Theoretical and Experimental Performance of an Electron Cyclotron Resonance Thruster Operating on Water Vapor Propellant

Anna J. Sheppard

A dissertation
submitted in partial fulfillment of the
requirements for the degree of

Doctor of Philosophy

University of Washington

2021

Reading Committee:

Justin Little, Chair

Chris Bretherton

Jim Hermanson

Mike Holmes

Uri Shumlak

Program Authorized to Offer Degree:
Aeronautics and Astronautics

University of Washington

Abstract

Theoretical and Experimental Performance of an Electron Cyclotron Resonance Thruster Operating on Water Vapor Propellant

Anna J. Sheppard

Chair of the Supervisory Committee:
Assistant Professor Justin Little
William E. Boeing Department of Aeronautics and Astronautics

A coaxial electron cyclotron resonance (ECR) thruster is analyzed experimentally and theoretically for operation on water vapor. A one dimensional model using chemical kinetics theory and empirical electron impact collision cross sections is developed to determine plasma composition along the length of the thruster. A peak in thruster efficiency occurs in a region dominated by molecular ions at electron temperatures greater than 15 eV. An ECR thruster is designed, fabricated, and tested to verify model predictions. Water vapor performance is compared to argon, krypton, and xenon to understand how mass utilization efficiency and frozen flow losses vary across propellant type. Thrust performance is measured using an inverted pendulum thrust stand; plasma characteristics are measured using a retarding potential analyzer, ExB probe, Langmuir probe, and emissive probe; and species concentrations in a water vapor plasma are measured using optical emission spectroscopy. Frozen flow losses increase as electron temperature decreases and are found to be a factor of two higher for water propellant compared with the atomic species at comparable electron temperatures. It is found that higher propellant atomic mass and lower ionization energies generally exhibit higher mass utilization, due in part to lower neutral density in the thruster. Multiply charged ions did not constitute a significant fraction of the plume for the atomic species. Mass utilization efficiency and frozen flow losses describe the trends in the thrust efficiency

but not the overall magnitude. Microwave coupling and diffusion to the walls are also identified as dominant loss processes. Incorporating wall and coupling losses to the control volume model enables good agreement between the experimental and predicted values for thruster performance and species concentrations.

TABLE OF CONTENTS

LIST OF FIGURES

LIST OF TABLES

ACKNOWLEDGMENTS

Grad school has been rough, but on the bright side, there have been many supportive and helpful people.

To my family and Michigander friends: thank you for supporting me even though you do not know what I do. Honestly, it's very freeing to have that kind of support network, and I wouldn't be here without you. You are great!

To all the friends and co-workers I had at AFRL: shout-out to the Ranchettes (Haasiendians and other affiliates) and the Tuesday/Saturday ultimate crowd for the museum trips, camping adventures, assorted athletics, and general bonhomie. Thank you for answering various plasma physics questions and encouraging me to get a PhD. I'm so excited for our next trip.

To the folks at MSNW and Helion: thank you for accepting me into your labs as a graduate student, for the fire-hose of information on pulsed power electronics and light detection schemes, and for generally being very entertaining co-workers who kept me up-to-date on little trees, tape drop experiments, and finely-aged Red Vines. I hear "Africa" by Toto and think of you.

To my labmates: thank you for answering my questions about LabView, power supplies, cables, diagnostics, etc, etc. I know a lot more now thanks to you fine folks. I apologize for all the screaming due to my steel tools being wrenched from my hands around my magnetic thruster, but thank you for your concern.

To the plasma grad students: thank you for helping with homework (especially the computational students that I have bothered more than any other group combined; sorry, not sorry) and with research. I also appreciate the friendships and camaraderie, especially

when I just needed to vent. Luckily our field is pretty small, so I am looking forward to meeting you all again over the course of our careers.

To the rest of the grad students: it has been delightful to get to know everyone in the various different specialities in A&A through soccer and frisbee and running into you in the halls. I have thoroughly enjoyed learning about your niche research topics and also being able to complain to other students about the ridiculousness of our department.

To Just Saiyan and the Thursday running group: joining you was 10/10 necessary for me keeping my mental sanity during my time in Seattle. Super fun to play/run with you all (except Joe), and I cannot wait for the next international tournament and/or Ragnar!

To Justin: thank you for butchering my first drafts (*including the acknowledgments section, whereupon* ***this guy*** *comments "what about your second, third, and fourth drafts?"*), asking clarifying questions on the analysis and the plots and the experiment, and generally being an A-1, top-notch advisor. I would have quit a long time ago if not for you, so thank you for having my (our) back during this entire process of school and moving labs and completing research. Also, also, thank you for being SO MUCH of a plasma nerd – every time you see plasma, it is as if you had never seen it before in your life and I heartily appreciate your child-like joy you have in your job. I wish I could be as lucky in my future career. Maybe we can collaborate on a solar eclipse chasing grant?

To Holmes: thank you for responding to all of my late-night questions and emails about plasma analysis. I felt slightly guilty for disrupting your retirement to ask you about Druyvesteyn distributions, but you ended up getting another real job, so I don't feel that bad about it. Also, the image I will forever have in my head for you is spork in a drill mixing up pancake batter (I think in the Mojave Preserve?), and I want you to know that I strive for that level of cool.

To Uri, Chris, and Jim: thank you for being very enthusiastic and encouraging about the prospect of graduate education. I want to additionally thank Uri for the book discussions,

Jim for bringing out his telescope to look at planets, and Chris for the interesting conversations. I cannot thank you enough for agreeing to be on my committee, and I'm very glad for your time.

To Bonnie: I am so excited to see the bound copy of this dissertation. I miss seeing you every day, but I will definitely smile and think of you fondly every time I look at this beautiful book. Thank you for everything.

To anyone I missed: while grad school has been rough, the people have been lovely. It has been great to chit chat with folks in the hallway, take classes throughout the University, fight the good fight with the union folks, and experience the PNW. So long and thanks for all the fish!

Last (legal) one: This material is based upon work supported by the National Science Foundation Graduate Research Fellowship Program under Grant No. DGE-1762114. Any opinions, findings, and conclusions or recommendations expressed in this material are those of the authors and do not necessarily reflect the views of the National Science Foundation. Thanks, NSF!

Chapter 1
INTRODUCTION

The use of electric propulsion (EP) systems on spacecraft is quickly becoming commonplace. EP systems have higher specific impulses compared to chemical propulsion systems and are well-suited to long-duration missions involving large changes in velocity (Δv). Furthermore, EP devices do not require propellants that are chemically reactive – they can accelerate any species which can be ionized. Corrosion, oxidation, or other chemical reactivity of the propellant or dissociation or ionization products is very much an engineering concern and will be discussed later. In general, however, this agnosticism in propellants is appealing for several mission applications: multimode, *in situ* resource utilization (ISRU), and air-breathing spacecraft.

Multimode propulsion systems enable mission flexibility by using one propellant to power different propulsion devices for different objectives: chemical systems for impulsive maneuvers and electric systems for station-keeping or precision maneuvers. A conceptual schematic is shown in Figure 1.1. This scheme eliminates the need to carry multiple types of propellant onboard the satellite and increases mission flexibility in terms of maneuverability [8]. However, finding propellant that is simultaneously applicable to both systems is an open challenge. EP devices with high efficiencies and thrusts have historically been operated on noble gas propellants, due primarily to their low reactivity. Other propellants have been used (mercury, iodine, Teflon) [53], but combustion with these propellants is essentially nonexistent. Current research into ionic liquid propellants is promising [24], but the molecular dynamics of these propellants in a plasma environment remain to be understood. Electrosprays exploit the inherent ionic nature of these liquids to accelerate them effectively, but

do not create plasmas. Understanding the different operating modes of electrosprays is an open question [137], but the research there is largely limited to a relatively narrow field of propellants.

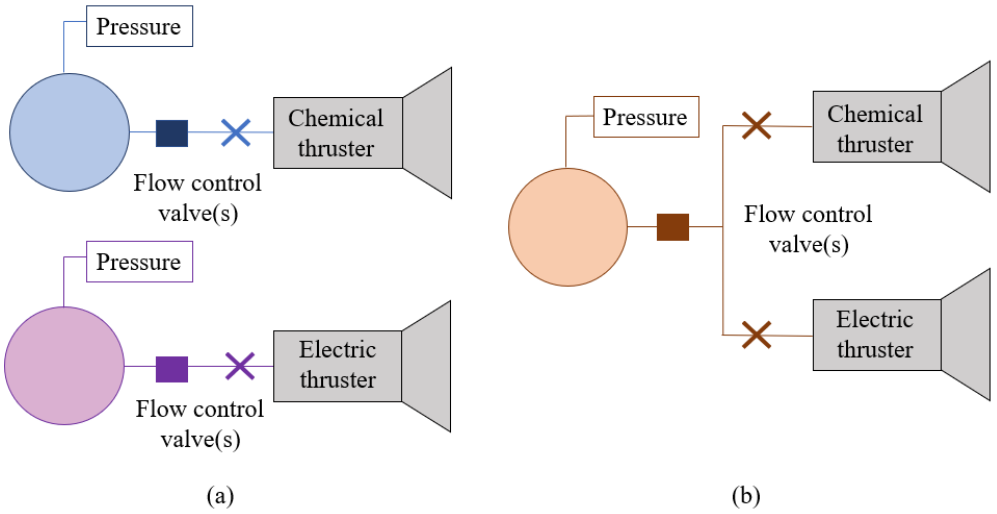

Figure 1.1: Conceptual schematic of benefits of multimode system.

Another motivator in adopting molecular propellants for use with EP devices is ISRU [112]. ISRU exploits the local availability of consumable propellants in order to expand mission capabilities. Exploration to more distant planets and asteroids would be more feasible if ISRU were available for propellant replenishment; missions could be extended or sample return might be possible if fuel could be collected at a destination. However, the types of molecules that are abundant in the solar system are not those currently compatible with state-of-the-art EP thrusters. Adapting EP devices to run on these molecules, such as hydrogen, methane, carbon dioxide, water, and nitrogen, would open extended mission capabilities for scientific exploration.

Finally, a subset of ISRU is air-breathing electric propulsion. These thrusters collect propellant from the upper atmosphere of bodies the satellites orbit. There is one main concern: can propulsion devices generate sufficient thrust to overcome the drag inherent

in collecting propellant? This question is the driving force behind mission studies done in this field, and several review papers summarize the current state of the art [115, 124]. One aspect of this research is developing thruster technologies that can appropriate accelerate the species found in the upper atmosphere of Earth (predominantly molecular and atomic oxygen and molecular and atomic nitrogen). However, these species are chemically reactive, so new thruster concepts or more robust components are required. Additionally, mission studies determining the feasibility of these concepts have suggested high power thrusters: research has proposed 6 MW magnetohydrodynamic (MHD) thrusters [32] and 0.7 - 2 MW Hall thrusters [101]. Limited experimental results with Hall thrusters and ion engines have shown increased erosion and worse performance operating with atmospheric propellants [27] compared with xenon, and both thrusters used xenon for ignition and to feed the cathode. Research into novel cathodes that can operate with oxidizing propellants is on-going [87, 83, 33, 94].

Understanding molecular propellant usage in EP requires fundamental studies into simple, relevant molecules. Gases of interest include water, carbon dioxide, and air, due to their abundance. Water and carbon dioxide are excellent gases to begin analyzing ionization and plasma composition, as they have been highly studied, and reaction cross sections have been experimentally determined for most dominant reactions [52, 51]. Likewise, air is comprised of common molecules and is of particular interest for Earth missions.

1.1 Molecular Plasmas in Industry

Molecular plasmas commonly occur in industrial processing [93, 49, 136, 68, 36, 6, 41, 110, 96]. However, in processing plasmas, metrics tracked are primarily related to quality of the manufactured product and not the state of the plasma: hydrogen production [95], syngas production [96], etch rate [36], etc. Other research into plasma catalysis for combustion [147, 148] and plasma chemistry for medical applications [84] use non-equilibrium, atmospheric pressure, and low temperature plasmas. Plasma chemical models have focused on the decomposition products that have industrial or environmental applications (e.g. dissociation of CO_2

plasmas [68]) as opposed to generation of ions that would produce thrust.

Electron cyclotron resonance (ECR) sources can achieve high plasma densities with an electrodeless configuration compatible with etching agents. Many ECR sources for plasma processing have a source with a magnetic mirror confinement scheme which impinges on a plate, which can be biased to enhance etching [88, 109]. These experiments rely on high ion flux but low ion energy. Stronger magnetic mirror fields at the exhaust of the ECR source decrease the mean ion energy, narrow the ion energy distribution, and increase ion current; furthermore, lower gas pressures increase average energy and the magnitude of floating potential on the substrate plate [88]. Sadeghi et al [109] used laser induced fluorescence to evaluate the ion velocity distribution function in an argon-helium propellant ECR source. Results show a bimodal velocity peak, with low energy ions arising from collisions near the magnetic nozzle throat and high energy ions accelerating directly from the ion source [109], which is promising for propulsion but not directly verified for that purpose.

Furthermore, several ECR studies for plasma processing focus on the specific species required for etching – controlling the CF_2 to F ratio produced from a CHF_3 plasma by modulating power [110], increasing ion beam current by exciting a slow wave structure to enhance ECR heating [7], modeling and measuring hydrogenated amorphous carbon film growth rates from CH_4 plasma [93], etc. This last paper explores much of the gas-phase chemistry present in a well-mixed ECR source operating with methane, and we see the presence of many ion species that may be beneficial to a thruster application. However, the neutral densities are an order of magnitude higher than that of ions [93], and none focus on ion production relevant to EP applications.

1.2 Molecular Plasmas in Electric Propulsion

With any plasma source, reactivity of the constituents is a concern, particularly for components in direct contact with the plasma. Since the propellants we are considering are expected to produce oxidative components, mitigating the exposure to thruster walls and electrodes is paramount. This leads to three natural divisions in electric propulsion: (1)

electrothermal devices, (2) modified state-of-the-art devices, and (3) electrodeless thrusters.

Electrothermal thrusters are historically the domain of molecular propellants. Hydrazine, ammonia, and hydrogen are well-established propellants for resistojets and arcjets [53]. Expansion into more potentially corrosive or oxidative propellants necessitates a method to heat the propellant without electrodes, and researchers developed microwave electrothermal thrusters (METs) [105]. METs use a resonant cavity to deposit energy from a standing microwave into a flowing propellants. Coupling (η_c) and thrust (η_T) efficiencies can be quite high ($\sim$60 - 80%), depending on propellant choice [34]. However, METs tend to be high power ($\sim$1 kW) and low specific impulse ($\sim$400 s) devices [14], although Takao et al tested a miniature MET that operated at 6 W and 79 s specific impulse [132].

State-of-the-art electric thrusters are not compatible with molecular propellant due to surface chemistry limitations at plasma-facing electrodes. Experiments with hot cathodes from Hall thrusters and emitters for ion engines have shown that the cathodes have downgraded performance due to oxidative contaminants. These hot cathodes rely on thermionic emission, and other techniques (such as field emission [87]) are not as successful or widely used. Tungsten and lanthanum hexaboride, common emitter materials, are poisoned by oxidation during operation [22], as are heating elements for resistojets and cathodes for arcjets. Designs for air-breathing varieties [97, 124] exist, but few experimental measurements on non-destructive operation with oxygen as the ionizing gas have been made [124]. Radio frequency (RF) cathodes, which theoretically have no limitations on species, have shown promising results on xenon [83, 33] but have not been fully tested with molecular species.

Finally, we consider three electrodeless thrusters. First, helicon sources are propellant-agnostic and are heavily used in industrial plasma processing. Helicon sources create and heat plasma by coupling energy via helicon waves using an RF supply and an axial magnetic field. For EP purposes, plasma is accelerated through a magnetic nozzle. Helicon thrusters are predicted to operate near 60 - 70% efficiency [3], but their measured thrust efficiency has been limited to less than 10% [130]. This low efficiency also contributes to the low measured specific impulse, which rarely exceeds 500 s. Understanding and closing the gap between the

theoretical and measured performance of helicons is presently the focus of intense research [130]. Helicon thrusters benefit from current-free double layers, which further accelerate particles in the plume. Charles et al [25] evaluated helicon thruster performance on a variety of molecular propellants and found double layer formation was similar for the propellants tested (N_2, CH_4, NH_3, and N_2O) compared with argon and simplified plasma chemistry in their analysis by considering only singly-charged molecular ions. Second, ECR thrusters selectively heat the electrons using cyclotron resonance. This resonance typically occurs only in a thin region within the thruster, and ionized plasma is accelerated with a magnetic nozzle. ECR thrusters are usually operated in the GHz range; at 2.45 GHz, an axial magnetic field strength of 875 G is required. Both waveguide and coaxial ECR thrusters have been designed [117, 139]. ECR thrusters are also predicted to operate near SOTA performance regimes but have experimentally demonstrated efficiencies around 15% with specific impulses on the order of 1,000 s [89]. Third, field reversed configuration thrusters create a high density, magnetized, and self-contained plasma toroid (plasmoid) which can be rapidly accelerated using magnetic fields. The plasmoid can be formed by a rotating magnetic field (RMF), as in the Electrodeless Lorentz Force (ELF) thruster [125], to drive azimuthal currents. The plasmoid is then accelerated axially by the Lorentz force described by $j_\theta \times B_r$. FRC thrusters are pulsed devices, which provides interesting options regarding throttleability of these thrusters, but space-proven pulsed power electronics require further research.

1.3 Water Propellant in Electric Propulsion Devices

In general, water is a popular propellant choice, with groups studying water propellant pulsed plasma thrusters [114, 66], arcjets [46], and miniature microwave discharge ion thrusters [94]. These works have largely neglected the chemistry occurring within those devices, focusing instead on measuring (worse) performance compared to devices designed for operation with other propellants, and these results are largely empirical. In order to mitigate the corrosive effects of water plasma, some groups investigating water vapor as a propellant use electrolysis to split the water vapor into hydrogen and oxygen [116, 44]; these gases can be used as

propellant in flight-proven configurations. Schwertheim and Knoll [116] suggest running oxygen through the main channel of a Hall thruster and hydrogen gas through the cathode, to mitigate oxidation issues. Harmansa et al [44] plan to use the hydrogen gas as propellant in a pulsed plasma thruster. The overall efficiency of these devices is limited by the electrolysis step, but there are potential benefits of separating water into hydrogen and oxygen: these could be recombined in a fuel cell for power, the oxygen could support human missions, and hydrogen can be used as a propellant in a wide variety of electrothermal or cold-gas thrusters.

If we consider non-electrolysis methods of using water as a propellant, we need to consider the the oxidative nature of water vapor. Electrodeless thruster concepts have been proposed to overcome electrode poisoning problems, but the role of plasma chemistry within these devices remains uncertain. Petro and Sedwick developed an analytic model for water vapor propellant in a helicon thruster [102]. This work considered the propellant to consist of singly ionized molecules (here H_2O^+), neglecting the effects of dissociation reactions, multiple reactions occurring as species translate the length of the thruster, and propellant dwell time in their analysis. Staab et al. [126] applied the model of Petro and Sedwick to a water propellant ECR thruster and found worse performance with water compared to argon due to lower mass utilization efficiency (lower ionization fraction of the water vapor). Further, this group designed a thruster, which has shown comparable thrust efficiency compared with argon but much worse compared with SOTA thrusters ($\sim$2% vs $\sim$60%) [92]. Water appears to be a good choice of propellant for METs, since the low mass increases specific impulse [14], and the ELF thruster has been tested on water vapor, but no conclusive performance parameters have been published [65].

1.4 Dissertation Organization

This work addresses open questions in the field regarding modeling of water vapor propellant plasma in an electrodeless thruster, testing and variation among water vapor and atomic species in an ECR thruster, and comparison between model and experiment. This disserta-

tion is organized as follows: Chapter 2 covers the theoretical background and control volume model developed to assess the feasibility of using water vapor as a propellant in EP devices. Chapter 3 describes the overall experiment and diagnostics designed to validate and verify the theoretical results. Chapter 4 details the experimental results relevant to describing the performance variation between argon, krypton, xenon, and water vapor in an ECR thruster. Chapter 5 presents results comparing the model to the experimental results for water vapor, and Chapter 6 concludes this work and suggests future work.

Chapter 2

THEORETICAL BACKGROUND AND MODELING

The goal of this chapter is to understand how the complexity of plasma chemistry affects the performance of EP thrusters. Determining the relationship between thruster geometry, input power, and plasma composition is critical to designing efficient thrusters that can operate on molecular propellants, and we developed a more realistic model of expected performance. Our model expands on previous analytic work, by considering dissociation reactions and transit timescales. We evaluate the plasma exhaust composition (densities of neutral and ionized species) as a function of thruster length, initial gas pressure, and electron temperature. These relationships are found using particle mass, momentum, and energy balance equations to develop a 1D analytical model. We apply this model to water vapor thrusters to assess feasibility of water as an EP propellant.

2.1 Description of the Model

We investigate the evolution of molecular propellant along the length of a plasma source with cylindrical symmetry, as shown in Fig. 2.1. The source has radius r_t and length L, with a primarily axial applied magnetic field. At one end of the plasma source, propellant is injected at a constant mass flow rate $\dot{m}$. The other end of the source is open, with a magnetic nozzle formed from the magnetic field which additionally accelerates ions leaving the source. This configuration is applicable to a variety of schemes, including ECR thrusters [126, 55], helicon thrusters [25], and radio-frequency sources [95].

We take a control volume approach to analyze the flow through the thruster, as described in Sec. 2.1.1. As the molecular propellant translates the length of the thruster, electron impact reactions create excited, ionized, and dissociated species. This chemistry is modeled

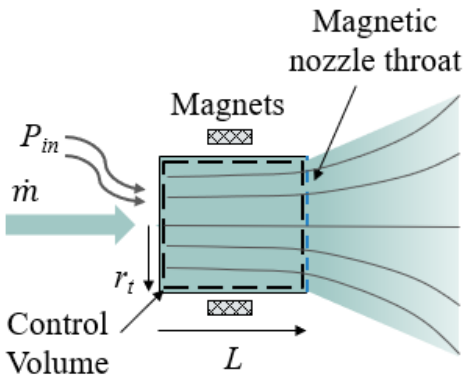

Figure 2.1: Schematic of the control volume model.

in Sec. 2.1.2. The composition of this plasma ultimately affects thruster performance, as shown in Sec. 2.1.3.

2.1.1 Control Volume Model

We develop a control volume model to determine species concentrations in the plasma plume. We assume the solution is steady state, and we ignore any explicit time dependence. Furthermore, we consider only axial variations in z; cross field diffusion and wall losses are ignored. This allows us to focus on the dominant chemistry occurring along the length of the thruster. These simplifications ultimately provide the best case scenario of thruster performance. Following our analysis, we will return to the issue of cross-field diffusion to examine the onset of wall losses in Sec. 2.2.4.

Species Continuity

The initial mass flow is introduced as a boundary condition, and total mass is conserved as species react. However, the mass flow rates of individual species evolve through production and consumption reactions. Considering the jth species, mass conservation is

$$m_j \left[\frac{\partial n_j}{\partial t} + \nabla \cdot (n_j \mathbf{u_j}) \right] = S_j - C_j, \tag{2.1}$$

where m_j is the particle mass of species j, n is the number density, $\mathbf{u}$ is the velocity vector, S_j represents production of j, and C_j represents consumption of j. We assume reactions are governed solely by electron impact collisions. We neglect reactions between heavy species, photon-driven reactions, radiative and dielectric recombination, and three-body recombination. This assumption, examined in more depth in Sec. 2.2.5, is generally valid for low-pressure EP plasmas. While they represent opposite physical processes, production and consumption have a similar form: reactions occur proportional to the density of each reactant species and the reaction rate, $\kappa = \kappa(T_e)$, where T_e is the electron temperature. For a specific reaction, this is

$$S_{k \to j} = \kappa_{k \to j} m_j n_e n_k \tag{2.2}$$

and

$$C_{j \to l} = \kappa_{j \to l} m_l n_e n_j, \tag{2.3}$$

where e represents the electrons, k represents reactant species producing species j, and l represents product species from reactions consuming species j. We assume the plasma has azimuthal symmetry and is radially uniform. This implies that $\dot{m}_j(z) = m_j n_j(z) u_j(z) A$, where $u_j(z) = u_{j,z}(z)$ is the axial component of the jth species velocity and A is the cross sectional area of the thruster. Further, by assuming steady state, we can write Eq. (2.1) as

$$m_j \frac{d(n_j u_j)}{dz} = \sum_{k \neq j} S_{k \to j} - \sum_{l \neq j} C_{j \to l}. \tag{2.4}$$

Assuming T_e is known, Eq. (2.4) gives us a set of N equations solving for N heavy species number densities, N heavy species velocities, and one electron number density ($2N + 1$ unknowns). We use momentum conservation (described in the next section) and charge conservation to close the model. Charge conservation requires

$$n_e = \sum_{j \in ions} Z_j n_j, \tag{2.5}$$

where Z_j is the charge state of ion species j.

Momentum Conservation

In order to describe species velocities, we need to understand the inherent physics of plasma sources operating with magnetic nozzles. Magnetic nozzles, similar to de Laval nozzles for fluid exhaust, convert the plasma thermal energy into directed kinetic energy. Recent analytic models of the flow before [3] and after [2, 90] the throat of the magnetic nozzle have shown the acceleration processes relevant to this model. Inside the plasma source, dynamic pressure provides the acceleration [3]. In the magnetic nozzle, diamagnetic electron currents generate a magnetic field that opposes the magnetic nozzle to provide thrust, and an ambipolar electric field accelerates the plasma [2]. Further downstream, the plasma detaches from the magnetic field as unmagnetized ions separate inertially from magnetic field lines [90, 78]. Once the plasma reaches the throat of the magnetic nozzle, it is assumed collisionless, and the effects of the magnetic nozzle on the ions and electrons are treated. Neutral species exhausting through a magnetic nozzle are not affected.

Inside the thruster, we assume that the plasma is quasineutral with no applied electric fields and that u_j and $\mathbf{B}$ are purely in the axial direction. Further, we assume perfect magnetic shielding of the lateral walls, due to a sufficiently high axial magnetic field, and large local magnetic shielding of the rear wall, consistent with those assumptions in [3]. These latter assumptions eliminate wall losses and the possibility of recombination at the wall, but Ahedo and Navarro-Cavallé showed these effects do not dramatically affect plasma density [3]. Ahedo and Navarro-Cavallé also calculated the ion velocity inside the thruster; while plasma velocity is not constant in the thruster, ions quickly accelerate to the sonic velocity, c_s. In our analysis, we use momentum conservation with an assumed potential drop along the thruster to determine ion velocity.

The potential drop between propellant injection and the throat of the magnetic nozzle is assumed to follow

$$V_p = -\frac{\gamma_e k_B T_e}{2}\left(\frac{z}{L}\right)^{\alpha}, \tag{2.6}$$

where $V_p(z)$ is the potential inside the thruster, γ_e is the polytropic index for the electrons, k_B is the Boltzmann constant, and α represents the steepness of the acceleration region. This profile ensures the ions exhaust at or near their sonic speed.

Solving for velocity requires solving the conservation of momentum equation. Assuming steady state solutions (no explicit t dependence) and azimuthal and radial symmetry (only z dependence), this becomes

$$\frac{d(m_j n_j u_j^2)}{dz} = Z_j q n_j E_z + F_{j,CX} + \sum_{k\neq j} S_{k\to j} u_k - \sum_{j\neq l} C_{j\to l} u_j, \tag{2.7}$$

where $E_z = -dV_p/dz$ is the electric field in the z direction and $F_{j,CX}$ is the momentum transfer due to resonant charge exchange for species j

$$F_{j,CX} = m_j n_j n_{j,CX} \sigma_{j,CX} (u_{j,CX} - u_j)|u_{j,CX} - u_j|, \tag{2.8}$$

where $\sigma_{j,CX}$ is the charge exchange collisional cross section for species j.

The first term on the right hand side of Eq. (2.7) is the acceleration of ions due to the presence of an electric field. The second term on the right hand side represents momentum conservation during charge exchange collisions. The third and fourth terms on the right hand side of Eq. (2.7) describe momentum conservation.

Energy Conservation

Power is a design point for thrusters, and accounting for power consumption ensures a self-consistent electron temperature solution. We calculate input power (P_{in}) from the energy to produce an atom, ion, or molecule from the parent species (frozen flow power, P_{ff}), the

energy required to accelerate these species through a magnetic nozzle (kinetic power, P_v), and other power loss terms (P_{losses}):

$$P_{in} = P_{ff} + P_v + P_{losses}. \tag{2.9}$$

The power required to ionize or dissociate is a frozen flow loss, as this power cannot be recovered from the flow as it exhausts. In this model, we do not make any estimates on power losses due to inefficiencies in coupling, line resistance, or wall losses. Therefore, $P_{losses} = 0$. This assumption, along with the frozen flow calculation, minimizes the power required and provides an upper limit on the thrust efficiency, as will be shown in Sec. 2.1.3.

Frozen flow power for a species j accounts for the energy loss of every reaction consuming j in the thruster volume, V. Since reaction rates describe number density production per second, we must integrate frozen flow losses over the thruster volume, which yields

$$P_{ff,j} = \int_V \left(\sum_{k \neq j} \kappa_{j \to k} \epsilon_{j \to k} n_e n_j \right) dV, \tag{2.10}$$

where $\epsilon_{j \to k}$ is the energy loss for the reaction $j \to k$. Integrating frozen flow power accounts for axial variation in n_e and n_j. We assume constant area, azimuthal symmetry, and radially uniform plasma and sum over all species j to get the overall frozen flow loss:

$$P_{ff} = \sum_j \pi r_t^2 \left[\int_0^L \left(\sum_{k \neq j} \kappa_{j \to k} \epsilon_{j \to k} n_e n_j \right) dz \right], \tag{2.11}$$

where $\pi r_t^2 = A$ for the geometry considered.

To account for the effects of excitation and radiative energy losses, we use an effective energy loss for ionization. We assume the effective energy loss for ionization of a neutral species is twice the ionization energy. This is the asymptotic limit at high T_e of energy loss due to ionization, excitation, and elastic scattering for noble gases [73]. This assumption is more accurate for high temperatures ($T_e > \epsilon_{min}$), and molecular species may have higher energy losses due to dissociation and vibrational and rotational modes. However, we track dissociation costs separately, and dissociation reactions were not subject to this effective

energy loss. Dissociative recombination reactions have no associated energy loss [56]. We evaluate the effects of these assumptions in Sec. 2.2.1.

In order to determine the kinetic power P_v, we evaluate the conversion from electron thermal energy to ion kinetic energy in the magnetic nozzle. This conversion factor, g_u, is the additional velocity increase of ions through the magnetic nozzle [79],

$$g_u = \frac{u_{j,ex}}{\sqrt{\frac{\gamma_e k_B T_e}{m_j}}}, \tag{2.12}$$

where $u_{j,ex}$ is the exhaust velocity of species j. We assume electrons cool polytropically in the exhaust plume and all the electron thermal energy is converted into ion kinetic energy [79]. Then g_u takes the following form

$$g_u = \sqrt{\frac{\gamma_e + 1}{\gamma_e - 1}}. \tag{2.13}$$

Experimentally, γ_e is found to be 1.15 - 1.37 [31, 77], and the value 1.2 is used here. For neutral species, the magnetic nozzle provides no additional acceleration. Incorporating the effect of magnetic nozzle acceleration into the kinetic power yields

$$P_v = \frac{1}{2}\pi r_t^2 \left(\sum_{j \in ions} g_u^2 m_j n_j u_j^3 + \sum_{j \notin ions} m_j n_j u_j^3 \right). \tag{2.14}$$

Together, Eqs. (2.4) - (2.9), (2.11), and (2.14) describe a control volume model which can estimate the performance of complex propellant thrusters given thruster geometry, mass flow rate, and input power. While this framework is general, we focus on water propellant in the following sections.

2.1.2 Plasma Chemistry Model for Water Vapor

Collisions in a water vapor plasma create excited and ionized states and neutral fragments of the molecular species, as shown in Table 2.1. As these species translate the thruster, the axial composition of the plasma changes. We determine these products from reaction

rates, κ, derived from experimental reaction cross sections, σ [52, 133, 118, 5, 134, 56]. We consider electron collisions and resonant charge exchange reactions because other heavy particle reactions have negligible cross sections at the pressures and temperatures relevant to EP [85, 134]. For a Maxwellian electron energy distribution, the reaction rate for electron collisions may be modeled as [40]

$$\kappa = \langle \sigma(\epsilon_e) v(\epsilon_e) \rangle = \sqrt{\frac{8q}{\pi m_e T_e^3}} \int_{\epsilon_{min}}^{\infty} \epsilon_e \sigma(\epsilon_e) \exp\left(\frac{-\epsilon_e}{T_e}\right) d\epsilon_e, \tag{2.15}$$

where ϵ_e is the electron energy, v is the electron velocity, q is the electron charge, m_e is the electron mass, T_e is the electron temperature, and ϵ_{min} is the threshold energy of reaction. ϵ_{min} is on the order of a few eV per reaction, as shown in Table 2.1. These reaction rates drive the change in number density of species in the plasma as shown by Eq. (2.4).

To determine the most prevalent species in the plasma, we evaluated all collisions of the initial species (water): elastic, excitation, vibration, rotation, ionization, and decomposition. Above a few eV, the energy loss due to elastic collisions is negligible compared to that from ionization and dissociation collisions and the likelihood of excitational, rotational, and vibrational collisions is small compared to the ionization and dissociation collisions, in agreement with the work of Petro and Sedwick [102]. Therefore, these reactions are ignored in the species continuity equations, Eqs. (2.4) - (2.5). Likewise, initially, all positive and negative ion species of H_2O mentioned by Itikawa [52] are considered; however, negative ions (above approximately 4 eV) and the positive ions O^{2+} and H_2^+ have negligibly small cross sections compared to the other positive ions and decomposition species. As such, the tracked species are pared down to the eight most prevalent: H_2O, OH, H, O, H_2O^+, OH^+, H^+, and O^+. We assume the water propellant is injected at the room temperature (298 K) sound speed, $u_{H_2O} = 369.9$ m/s; all species are initially assumed to have this velocity until they are accelerated as defined by Eq. 2.7. As these species translate the thruster, they may experience subsequent reactions, including dissociative recombination, as shown in Table 2.1. The products from these reactions are tracked and allowed to react until they ex-

haust from the thruster. The inclusion of dissociation reactions and transit time scales in the thruster is a departure from the work of Petro and Sedwick, which ultimately shows a peak in performance corresponding to specific thruster geometries yielding higher concentrations of molecular ions.

Table 2.1: The product species with dominant reaction rates are tracked for each reactant species. In some cases, the cross section correlates to any of several reactions that may yield the product species (e.g. producing H from H_2O). This total cross section is used, and the smallest ϵ_{min} of any reaction producing the product is used as the energy cost per atom/molecule. H^+ and O^+ are both assumed to exhaust before any recombination reactions occur.

Type of collision	Reaction	ϵ_{min} (eV)	Reference
Dissociation	$H_2O + e^- \rightarrow OH + H + e^-$	5.1	[52]
Dissociation	$H_2O + e^- \rightarrow O + e^-$	9.2	[52]
Ionization	$H_2O + e^- \rightarrow H_2O^+ + 2e^-$	12.6	[52]
Dissociation and Ionization	$H_2O + e^- \rightarrow OH^+ + H + 2e^-$	18.1	[52]
Ionization	$H_2O + e^- \rightarrow H^+ + 2e^-$	17.0	[52]
Ionization	$H_2O + e^- \rightarrow O^+ + 2e^-$	19.0	[52]
Ionization	$OH + e^- \rightarrow OH^+ + 2e^-$	13.0	[133]
Dissociation and Ionization	$OH + e^- \rightarrow O^+ + H + 2e^-$	16.0	[133]
Dissociation and Ionization	$OH + e^- \rightarrow H^+ + O + 2e^-$	16.0	[133]
Ionization	$H + e^- \rightarrow H^+ + 2e^-$	14.6	[118]
Ionization	$O + e^- \rightarrow O^+ + 2e^-$	13.62	[134]
Dissociative Recombination	$H_2O^+ + e^- \rightarrow OH + H$	–	[56]
Dissociative Recombination	$H_2O^+ + e^- \rightarrow O + 2H$	–	[56]
Dissociative Recombination	$OH^+ + e^- \rightarrow O + H$	–	[5]
Resonant Charge Exchange	$H_2O + H_2O^+ \rightarrow H_2O^+ + H_2O$	–	[76]
Resonant Charge Exchange	$OH + OH^+ \rightarrow OH^+ + OH$	–	$*$
Resonant Charge Exchange	$H + H^+ \rightarrow H^+ + H$	–	[108]
Resonant Charge Exchange	$O + O^+ \rightarrow O^+ + O$	–	[127]

$*$Assumed equal to H_2O resonant charge exchange cross section

2.1.3 Thruster Performance

We assess thruster performance using specific impulse and thrust efficiency. Specific impulse is representative of the thrust produced relative to mass flow rate, and thrust efficiency is a measure of the amount of kinetic power produced from input power. These two parameters describe the feasibility of using water vapor as a propellant in EP thrusters.

Specific impulse (I_{sp}) is a ratio of the thrust produced by exhausted particles compared to the mass flow rate and includes contributions from both the ionized and neutral particles. The neutrals exhaust thermally, while the ions gain additional acceleration from the magnetic nozzle, as described in Sec. 2.1.1. For a multi-species exhaust, the specific impulse may be written as

$$I_{sp} = \frac{\pi r_t^2}{\dot{m} g_0} \left(\sum_{j \notin ions} m_j n_j u_{j,ex}^2 + \sum_{j \in ions} g_u m_j n_j u_{j,ex}^2 \right), \tag{2.16}$$

where g_0 is the sea-level acceleration of gravity. Specific impulse defines the class of missions where a proposed thruster would be useful, as defined by the rocket equation. For common Earth-orbit EP applications, the desired I_{sp} is usually around 1,500 - 2,000 s [98]. For interplanetary travel, desired I_{sp} is higher, around 3,000 - 4,000 s [53].

The thrust efficiency (η_T) for an electric propulsion thruster is defined as

$$\eta_T = \frac{\dot{m}(g_0 I_{sp})^2}{2P_{in}}. \tag{2.17}$$

The overall efficiency is a measure of the kinetic power relative to the input power. As described in Sec. 2.1.1, power losses (P_{ff} and P_{losses}) are minimized in this model, so calculated P_{in} is a minimum of the actual power required. In our analysis, the η_T we calculate is an upper bound on the expected efficiency of an actual thruster.

To identify the contributing factors to variations in specific impulse and thrust efficiency, we evaluate the following parameters: average ion mass, average ion cost, and ionization fraction. We calculate average ion mass as

$$\bar{m}_i = \frac{\sum_{j \in ions} m_j^2 n_j u_j}{\sum_{j \in ions} m_j n_j u_j}. \tag{2.18}$$

Here, $\bar{m}_i$ describes the composition of the ion species. Lower average ion mass indicates a more atomic plasma, while higher average ion mass points to more molecular ions. The average ion cost (ϵ_i) is the frozen flow energy loss per ion and is calculated as

$$\epsilon_i = \frac{P_{ff} \bar{m}_i}{\pi r_t^2 \sum_{j \in ions} m_j n_j u_j}. \tag{2.19}$$

Large values of ϵ_i are generally the result of the propellant undergoing multiple reactions. The ionization fraction (η_u) is given by

$$\eta_u = \frac{\pi r_t^2 \sum_{j \in ions} m_j n_j u_j}{\dot{m}}. \tag{2.20}$$

Here the ionization fraction also represents the mass utilization efficiency, which describes the rate of ion mass flow at the exhaust relative to the total mass flow rate. Specific impulse and thrust efficiency generally scale with ionization fraction because ionized species achieve higher exhaust velocities.

Electric thrusters require high thrust efficiencies to effectively utilize on-board power. State of the art Hall thrusters or gridded ion engines typically operate around 60 - 70%. Helicon and ECR thrusters are predicted to operate at similar efficiencies [3, 117]; however, their measured thrust efficiency to date has been limited to less than 20% [89, 130]. The power and propellant losses responsible for these inefficiencies also prove detrimental to the measured I_{sp}, which rarely exceeds 1,000 s. Understanding and closing the gap between the theoretical and measured performance of electrodeless designs is presently the focus of intense research [130].

Improving η_T should improve performance of these electrodeless designs, but experimental results have been limited. This is especially true for non-traditional propellants such as water. In these cases, plasma chemistry becomes important, and these changes in regimes have driven the work described in this chapter.

2.2 Results and Discussion

With the framework outlined above, we evaluate thruster performance changes due to water vapor plasma chemistry. Similarity across operating regimes defines scaling parameters important to maximizing performance and designing thrusters that are viable in real-world missions.

2.2.1 Plasma Composition

Plasma composition is important in describing thruster performance; the charge state determines whether particles will interact with magnetic or electric fields and therefore contribute more to thrust, the average mass of the particles will dictate specific impulse, and the presence of neutrals reduces overall efficiency. We use the model described above to study the effects of varying electron temperature and pressure on plasma composition. At a given electron temperature, as pressure increases, the distance required for reactions, as specified in Eq. (2.15), decreases, since the concentration of reactants is higher. In this case, distance correlates to the amount of time components have to react; particles take more time to transit longer distances. The similarity is linear for a given voltage drop, so that we need only consider the product of pressure and thruster length to determine the relative mass flow of species along the thruster, as shown in Fig. 2.2. The first thing we notice, at all temperatures, is the decrease in water vapor and rise of OH. The dissociation reaction leading to OH has the smallest reaction energy (as shown in Table 2.1) and the largest reaction cross section from water across the range of relevant temperatures, $\sim 5 - 40$ eV. As OH is produced, it is also consumed by ionization reactions encouraging the growth of O^+, H^+, and OH^+. OH concentration reaches a peak before the complete elimination of H_2O.

As the electron temperature increases, the likelihood of higher-energy, predominantly ionization, reactions increases as well. We note a peak in the production of H_2O^+ ions corresponding to the elimination of neutral water propellant. OH^+ is produced from several reaction pathways in the plasma, which explains its sharp concentration increase early on.

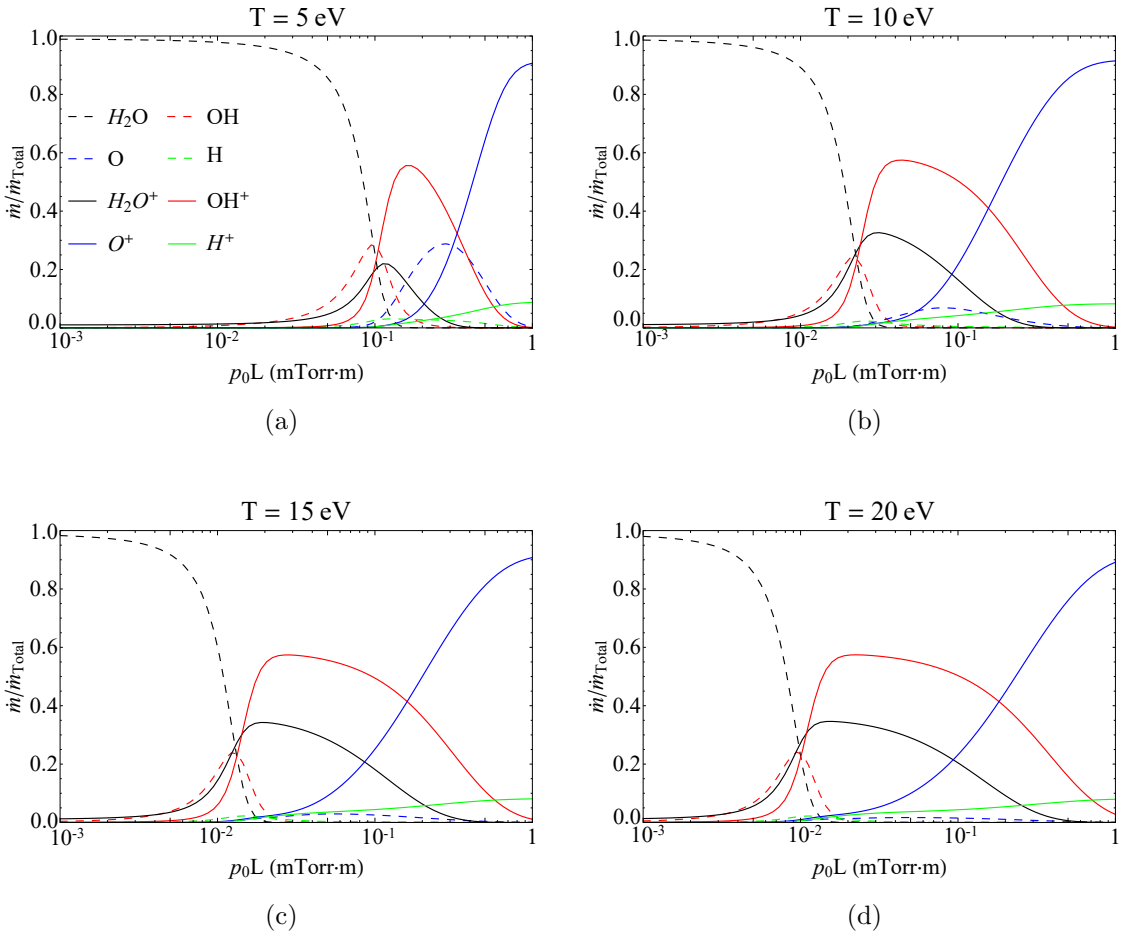

Figure 2.2: The normalized plasma composition at the thruster exhaust plane as a function of pressure times length with $\alpha = 2$ for (a) $T_e = 5$ eV, (b) $T_e = 10$ eV, (c) $T_e = 15$ eV, (d) $T_e = 20$ eV. Increasing pressure appears to push the reaction zones closer to the injector for a fixed length thruster. Increasing electron temperature increases the region of high molecular ionization.

The peak H_2O^+ and OH^+ mass flow rates are approximately constant across electron temperature, but the range of p_0L where they are the dominant species increases with electron temperature. Both molecular ions can dissociatively recombine, preferentially at low tem-

peratures, which explains the larger range of p_0L over which molecular ions dominate at higher temperatures.

In Fig. 2.2, atomic neutral concentrations begin to increase around the H_2O^+ and OH^+ peaks. O mass flow rate becomes noticeable around the peak of H_2O^+ ion concentration. O concentration decreases as the electron temperature increases for two reasons: first, the cross sections for the production of O from H_2O^+ and OH^+ decrease with increasing temperature; and second, the reaction $O \rightarrow O^+$ increases with electron temperature. Likewise, H production decreases as electron temperature increases for comparable reasons. O^+ mass flow rate reaches a steady state at lower p_0L for lower T_e, as shown in Fig. 2.2. Within the range shown here, O^+ increases most rapidly when the electron temperature is high enough to facilitate the conversion of O to O^+ but low enough that there is still a sizable population of O; this is also the case for the $H \rightarrow H^+$ reaction, but the effects do not appear as noticeable.

2.2.2 Thruster Performance

Thruster performance is predominantly determined by the ionization fraction and mass of exhausted species. Forming atomic ions increases the energy cost per exhausted ion, since these ions are usually formed from several dissociation or ionization reactions. Additionally, because specific impulse depends on mass, exhausting atomic species generally increases specific impulse. While this may be desirable, the extreme lightness of hydrogen generally increases this specific impulse to beyond that required for common EP applications ($\sim$ 1,000 - 4,000 s).

Fig. 2.3 shows several parameters of interest in evaluating thruster performance, whose values correlate to changes in plasma composition. Fig. 2.3(a) shows the average cost per ion as a function of p_0L for several electron temperatures of interest. Initially, the value slowly increases as the neutral molecules H_2O and OH produce ions and atomic neutrals. The ion cost increases more sharply as these remaining species undergo multiple reactions to produce O^+ and H^+, before reaching steady state values. The dip in ionization cost that is more pronounced for lower T_e is correlated with higher H_2O^+ production, followed by higher

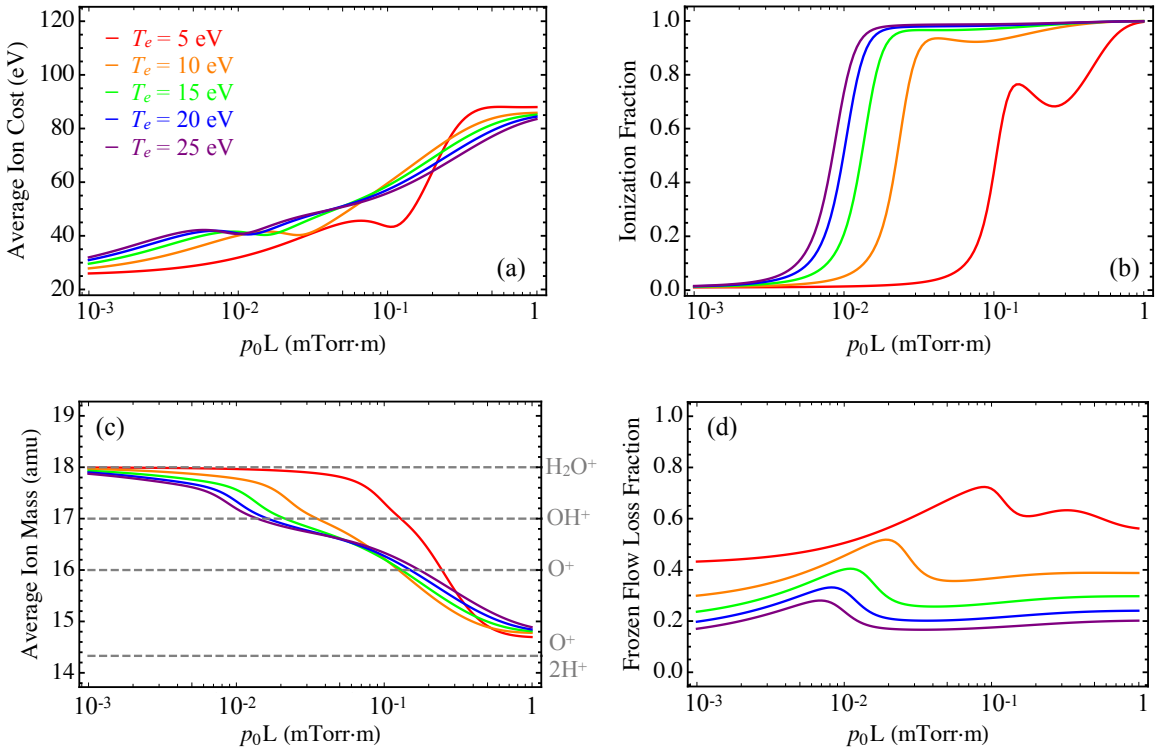

Figure 2.3: For $\alpha = 2$: (a) The average ion cost for exhaust at at any point defined by p_0L in the thruster. (b) The ionization fraction vs p_0L. As electron temperature increases, the ionization fraction increases rapidly at smaller p_0L. (c) Average ion mass vs p_0L with references to the three largest mass species and the steady-state mass average. At higher p_0L, the curves for different electron temperatures collapse onto one another as they reach a steady-state value of 14.33 amu. (d) Frozen flow loss fraction vs p_0L for electron temperatures of interest. Higher electron temperatures correspond to lower frozen flow losses. As p_0L increases, frozen flow losses first increase corresponding to neutral products then decrease as more ionized products are exhausted.

concentrations of neutral atomic species that increase the average ion cost. The steady-state ion cost decreases as electron temperature increases, due to higher ionization fractions and increasing likelihood of direct ionization reactions (as opposed to ionization of dissociated

neutrals).

In Fig. 2.3(b), for all electron temperatures, the ionization fraction initially increases as molecular ions are produced, peaks when those ionized species reach some critical concentration such that they begin to dissociate, decreases as ions recombine and dissociate, and finally increases as atomic ions are produced. The ionization fraction eventually trends toward unity as the atomic neutrals ionize. This behavior is more pronounced at lower electron temperatures, where the dissociative recombination reaction rates are higher. This characteristic nature, which is unique to molecular propellant EP, will be expanded in further depth in Sec. 2.2.3.

Fig. 2.3(c) shows the average ion mass as a function of p_0L for different electron temperatures. For every temperature, there are two steep drops corresponding to changes in the dominant ion species: for small p_0L, OH^+ concentration outpaces H_2O^+ concentration; for large p_0L, the average ion mass approaches an equilibrium value of 14.33 amu (H_2O converted to 2 H^+ and 1 O^+) due to the complete dissociation and ionization of the propellant. For moderate p_0L, ion mass slowly decreases as OH^+ and H_2O^+ dissociate and atomic ions begin to form. These characteristics are similar for all the electron temperatures plotted but with sharper transitions at lower T_e.

Fig. 2.3(d) shows the frozen flow loss fraction as a function of p_0L for the electron temperatures of interest. Higher electron temperatures correspond to lower peak frozen flow loss fraction, due in part to higher kinetic power. Frozen flow loss fraction initially increases as molecules begin to dissociate and then decreases as molecules ionize and accelerate through the thruster. At large p_0L, frozen flow losses increase again as atomic neutrals and ions proliferate. Higher electron temperatures correspond to the largest range of p_0L with low frozen flow losses; this is related to the long lifetimes of molecular ions in the thruster at those conditions and the larger ion velocities which increase kinetic power. At lower electron temperatures, the frozen flow loss appears to have two local peaks before relaxing to a steady-state value: one corresponds to the initial concentrations of molecular ions and one to the later concentrations of atomic neutrals.

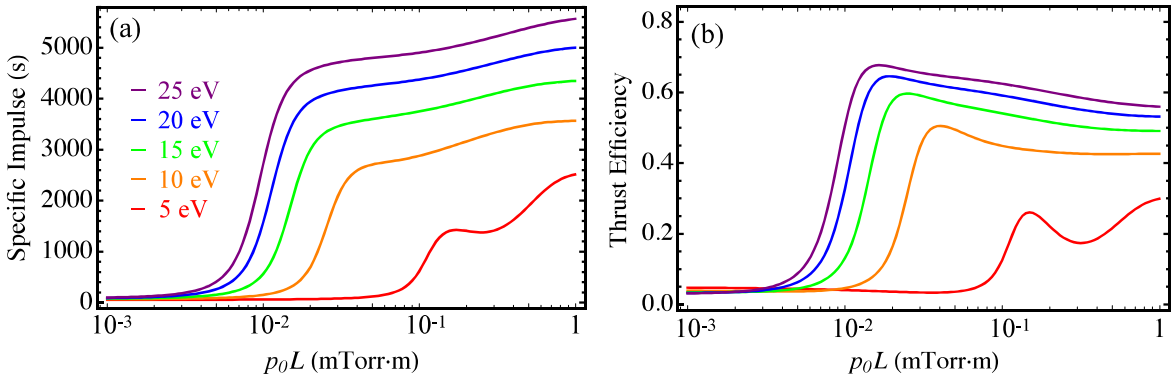

Figure 2.4: For $\alpha = 2$: (a) Specific impulse, calculated per Eq. (2.16), vs p_0L for electron temperatures common in EP. (b) Thrust efficiency vs p_0L. Note the similarity between this plot and ionization fraction represented in Fig. 2.3(b).

With this understanding of the overall behavior of the bulk plasma, we consider specific thruster performance characteristics, namely the specific impulse and thrust efficiency. In Fig. 2.4(a), the specific impulse against p_0L is plotted. We note a sharp increase at low p_0L as ionization quickly increases, followed by a slow increase as atomic ions begin to dominate the plasma composition. At $T_e = 5$ eV, I_{sp} has two sections of rapidly increasing slope; the first corresponds to the formation of molecular ions and the second to the formation of atomic ions. At higher p_0L, I_{sp} reaches a steady state value corresponding to atomic ions for all temperatures.

Thrust efficiency is plotted in Fig. 2.4(b) and loosely follows the ionization fraction shown in Fig. 2.3(b). The thrust efficiency is lower than the ionization fraction because it also includes effects from the frozen flow losses corresponding to the increased energy required for multiple reactions. For this reason, thrust efficiency decays after reaching an initial peak corresponding to high molecular ion formation. At higher p_0L, the thrust efficiency increases for the $T_e = 5$ eV case as more atomic ions are created, and, at higher electron temperatures, the thrust efficiency levels out. We note that this behavior is unique to molecular propellants.

As expected, increased thrust efficiency is correlated with increased I_{sp}. However, this

correlation stops when the thrust efficiency reaches its first peak; thereafter, the thrust efficiency decreases as specific impulse increases for electron temperatures greater than 15 eV. For lower electron temperatures, a constant I_{sp} drops thrust efficiency, but a two-fold increase in specific impulse does moderately improve efficiency at $T_e = 5$ eV. This is characteristically different from performance on noble gases in state of the art EP devices [13, 11], which monotonically increase toward a limiting thrust efficiency and I_{sp}, as shown in Fig. 2.4(a) and 2.4(b). As electron temperature increases, this thrust efficiency peak broadens due to the lower rates of dissociative recombination at higher temperatures. At these temperatures, a small change in operating conditions ($p_0 L$) does not significantly alter performance.

We take a moment to comment on the influence of our effective ionization energy assumption on the results in Figs. 2.3 and 2.4. Petro and Sedwick [102] show that losses due to elastic collisions and rotational and vibrational modes are negligible for $T_e \gtrsim 5$ eV, and losses due to radiation from dissociative species excitation are small (~ 1 eV) compared with ionization and dissociation losses for $T_e \sim 5 - 40$ eV. As a result, the addition of these loss processes would not significantly alter our results. Itikawa and Mason note that experimental data for electron impact excitation of H_2O is incomplete [52], which yields uncertainty regarding the effective ionization cost coefficient (recall we used the value 2). We explored this uncertainty by running our model for effective ionization costs in a range representative of typical excitation energy variations, $1.5\epsilon_i$ to $2.5\epsilon_i$. The results indicate that the general trends shown in Figs. 2.3 and 2.4 do not change significantly and that the location of the various local minima and maxima occur at approximately the same value of $p_0 L$. As expected, the main consequence of increasing the effective ionization cost coefficient is an increase in average ion cost and frozen flow loss fraction, and decrease in thrust efficiency. However, we note that additional experimental data is needed to determine the best value for the ionization cost coefficient for H_2O.

It is clear from our results that frozen flow losses have a significant impact on characteristic performance of molecular propellant EP devices. We can easily scale thruster designs based on common design parameters using performance maps, as shown in Fig. 2.5. Fig. 2.5

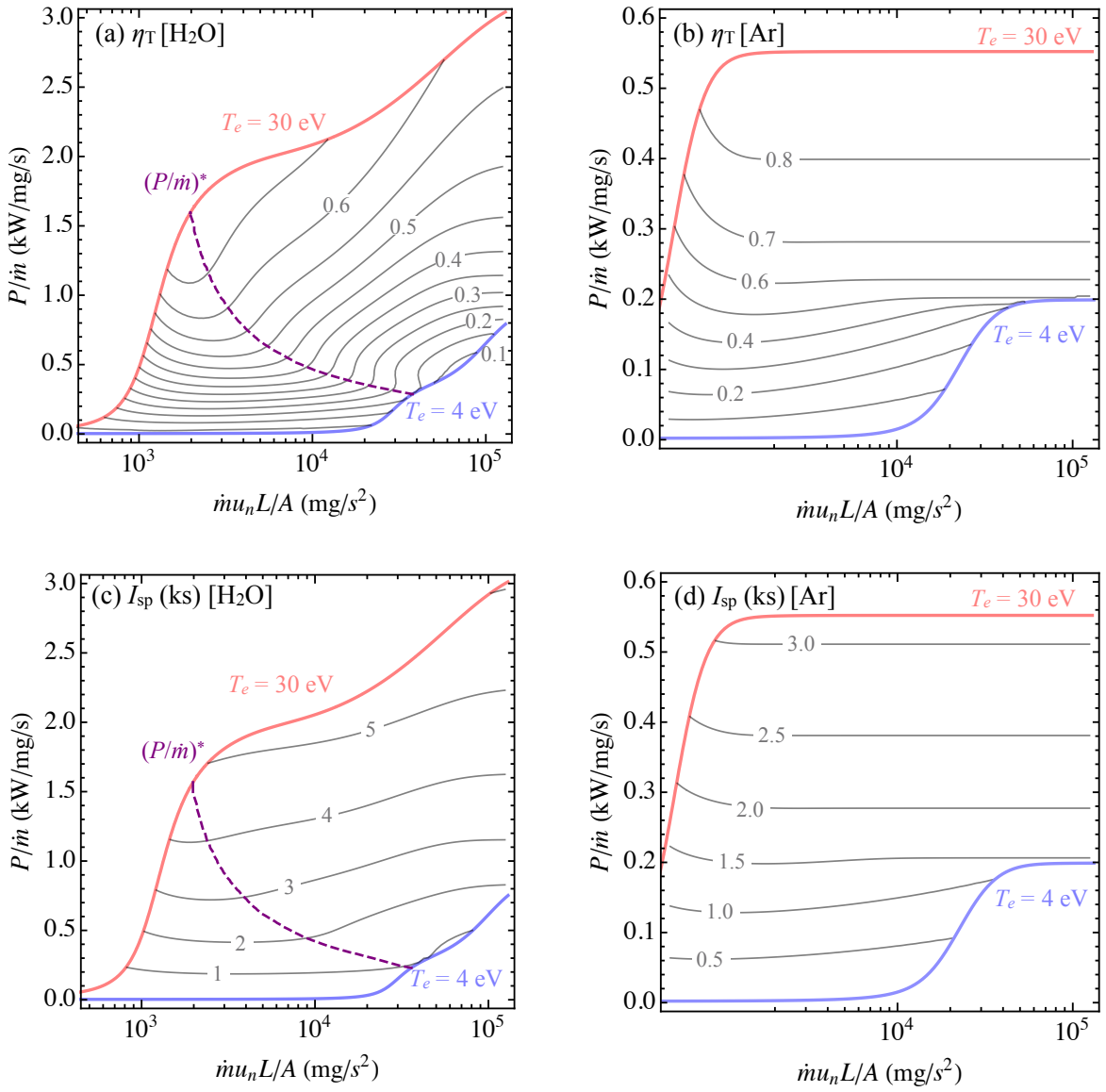

Figure 2.5: For $\alpha = 2$: (a) Contour map of thrust efficiency for water vapor. $(P/\dot{m})^*$ corresponds to the highest initial thrust efficiency [as shown in Fig. 2.3(b)]. (b) Contour map of thrust efficiency for argon. (c) Contour map of I_{sp} for water vapor. (d) Contour map of I_{sp} for argon.

presents contour plots of thrust efficiency [(a) and (b)] and specific impulse [(c) and (d)] for water vapor and argon. The y-axis is $P/\dot{m}$, and the x-axis is $p_0 L = \dot{m} u_n L/A$. This change to the x-axis describes design constraints in more commonly used terms – mass flow rate is variable, velocity is the room temperature thermal velocity of the neutral propellant, and the length and area constraints describe the geometry of the thruster. The blue and red lines are curves of constant electron temperature, 4 and 30 eV, respectively. On Fig. 2.5(a) and 2.5(c), the $(P/\dot{m})^*$ corresponding to the first peak of thruster efficiency shown in Fig. 2.3(b) is highlighted with a dashed line. The curves for argon are determined using the same framework described for water, but argon, as a noble gas, has only one product in this range of temperatures: the singly charged ion. Consistent with our assumption for water vapor propellant, we include radiative losses for argon by using an effective ionization energy that is equal to twice the minimum ionization energy. This assumption is reasonably accurate for $T_e > 8$ eV [73]. Again, the thruster efficiency should be considered an upper limit.

At first glance, the maps are qualitatively different for water vapor compared with argon. Comparing thruster efficiency [Fig. 2.5(a) vs 2.5(b)], we see that argon has higher efficiency at lower temperatures and requires less power per unit mass flow rate compared to water vapor. Additionally, above $\sim 60\%$, the argon thrust efficiency is approximately constant as a function of $\dot{m} u_n L/A$ for $\dot{m} u_n L/A > 2 \times 10^3$ mg/s^2. Thrust efficiency with water vapor, on the other hand, fluctuates with $\dot{m} u_n L/A$, increasing to a maximum then decreasing as $\dot{m} u_n L/A$ increases. At higher $\dot{m} u_n L/A$, molecular species are more likely to dissociate or ionize, unless molecular ions are sufficiently accelerated to leave the thruster before those reactions occur. The increased likelihood of dissociation increases required power and reduces efficiency.

Comparing the specific impulse curves shown in Fig. 2.5(c) and 2.5(d), we note that similar temperatures yield higher specific impulses for water vapor than for argon, due to the mass difference of the propellants. At a constant $P/\dot{m}$, specific impulse is approximately constant as $\dot{m} u_n L/A$ increases for argon, whereas specific impulse decreases with $\dot{m} u_n L/A$ for water, due to the effect of dissociative recombination.

2.2.3 Scaling Laws for H_2O Thruster Optimization

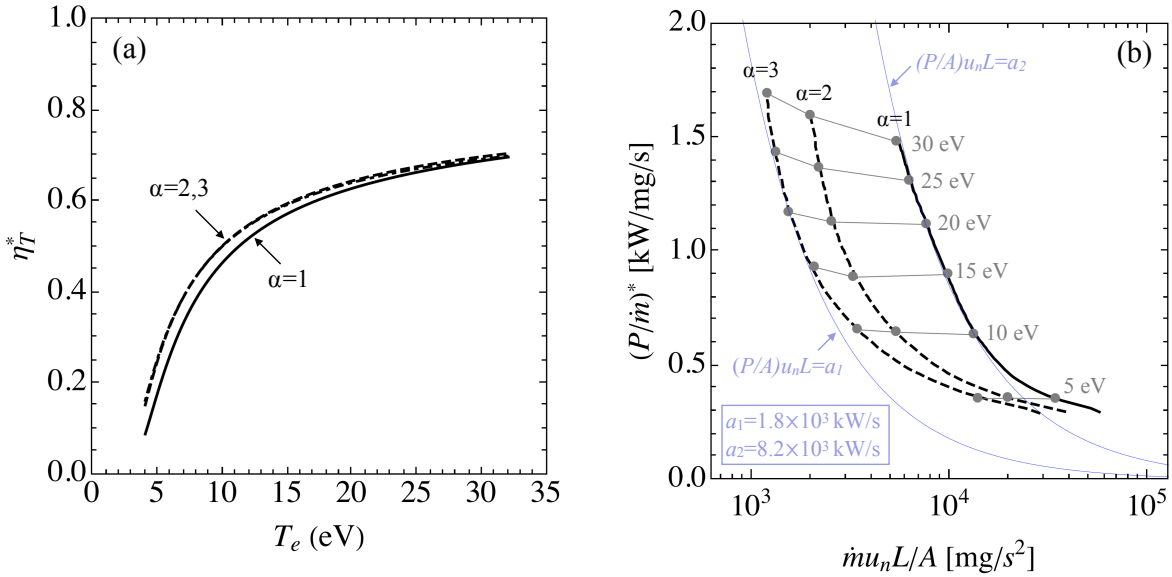

Figure 2.6: (a) The first peak thruster efficiency (η_T^*) vs electron temperature for different voltage drop profiles [Eq. (2.6)]. Sharpening the acceleration region (i.e. increasing α) does not appear to have much effect on peak efficiency. (b) Power per unit mass flow rate at η_T^* ($(P/\dot{m})^*$) vs $\dot{m}u_nL/A$. Setting $(P/\dot{m})^* = a/(\dot{m}u_nL/A)$, we find contours of constant power density (P/A), represented by a_1 and a_2.

With these results, we look for scaling laws to simplify design. The first peak in thruster efficiency η_T^* occurs at $(P/\dot{m})^*$, which can be determined uniquely from electron temperature. We also seek to account for the amount of uncertainty in describing the voltage drop from injection to magnetic nozzle. To that end, we investigate the relationship between η_T^*, $(P/\dot{m})^*$, and α, as defined in Eq. (2.6). These relationships are shown in Fig. 2.6.

Considering Fig. 2.6(a), we note that α does not have a significant effect on the value of η_T^*, especially above $T_e \sim 15$ eV. Furthermore, we note that $T_e \sim 10$ eV corresponds to a threshold thruster efficiency of 50%. Considering our optimistic model, thrusters operating on water vapor propellant at $T_e < 15$ eV would significantly underperform compared to state

of the art EP systems.

When designing a thruster or experiment, Fig. 2.6(b) provides a map of required power for peak efficiency. With respect to electron temperature, we note that the $(P/\dot{m})^*$ to achieve an electron temperature is approximately constant; this makes sense, as $(P/\dot{m})^*$ is an energy per mass of propellant to achieve an optimal plasma composition, which we showed earlier was a unique function of electron temperature. As α increases, the acceleration region for ions is narrower, and thruster length for a given pressure shortens. We relate these scalings by considering relationships between $(P/\dot{m})^*$ and $\dot{m}u_nL/A$ of the form $P/\dot{m} = a/(\dot{m}u_nL/A)$. This equation describes contours of constant power density given an initial species and thruster length: $P/A = a/(u_nL)$. From Fig. 2.6(b), we see that increasing α corresponds to decreasing power density required for optimum thrust efficiency. Additionally, for a given voltage drop profile, power density is constant for optimal performance for T_e between 10 and 30 eV. Considering the uncertainty in the voltage drop profile, experiments designed to span different power densities will have the flexibility to operate at the empirical optimum.

2.2.4 Onset of Wall Losses

Wall losses in EP devices reduce performance by decreasing efficiency and increasing thruster erosion. Magnetic shielding of the walls, achieved in part by the magnetic field required for the magnetic nozzle, reduces electron mobility to the walls. For the plasma source geometry described here, both classically-dominated [81] and Bohm-dominated [69] diffusion have been observed experimentally. In this section, we will examine the general conditions required to ensure wall losses are much smaller than flow out of the device, which can also be thought of as a minimum requirement for the magnetic field strength. Because high thrust efficiencies require large ionization fractions, we limit our analysis to diffusion processes in a highly-ionized plasma.

For both classical and Bohm diffusion, we evaluate the anisotropic Péclet number ($\mathrm{Pe_{an}}$), which compares field-aligned advection to perpendicular diffusion [81]. In general, we write

the Péclet number as

$$\mathrm{Pe}_{\mathrm{an}} = \frac{c_s/L}{D_\perp/r_t^2}, \tag{2.21}$$

where $c_s = \sqrt{\gamma_e k_B T_e/m_i}$ is the ion acoustic speed and $D_\perp$ is the cross-field diffusion coefficient. The classical cross-field diffusion coefficient is given by $D_{\perp,\mathrm{cl}} = \eta_\perp p_e/B_0^2$, where $p_e = n_e k_B T_e$ is the electron pressure, B_0 the magnetic field strength, and $\eta_\perp$ the cross-field resistivity. The ratio of the electron pressure and neutral pressure simplifies to $p_e/p_0 = (n_e/n_0)(T_e/T_n)$. We observe that within the thruster channel $\sqrt{T_n/T_e} \lesssim n_e/n_0 < 1$, which implies $\sqrt{T_e/T_n} \lesssim p_e/p_0 < T_e/T_n$. This scaling suggests that classically-driven wall losses can be neglected ($\mathrm{Pe}_{\mathrm{an}} \gg 1$) if

$$p_0 L < \frac{c_s B_0^2 r_t^2 T_n}{\eta_\perp T_e}. \tag{2.22}$$

Here, we have relaxed the requirement on $p_0 L$ because the upper bound of p_e/p_0 occurs only in a relatively small region within the thruster. The same analysis performed for cross-field Bohm diffusion, $D_{\perp,B} = k_B T_e/(16 e B_0)$ [26], yields the additional requirement

$$\frac{L}{r_t} \ll \frac{16 r_t}{r_{L,i}}, \tag{2.23}$$

where $r_{L,i} = m_i c_s/(eB_0)$ is the characteristic ion Larmor radius. Note that p_0 does not appear in Eq. (2.23); instead, Bohm diffusion limits the aspect ratio of a given device.

Eqs. (2.22) and (2.23) represent general requirements for limiting wall losses due to classical and Bohm diffusion, respectively. To provide an estimate of representative values, we consider an existing ECR thruster [138] with $r_t = 15$ mm, $L = 15$ mm, $B_0 = 875$ G, and $T_e = 20$ eV. Using Spitzer resistivity [26], $\eta_\perp \approx (100 T_{\mathrm{ev}})^{-3/2}$ [$\Omega \cdot$ m], Eq. (2.22) suggests that classical cross-field diffusion can be neglected for water propellant if $p_0 L < 17$ mTorr·m. Notably, the values of $p_0 L$ that we have considered throughout our analysis satisfy this requirement. According to Eq. (2.23), Bohm diffusion can be neglected for $L/r_t \ll 10$, which is also satisfied for this particular thruster geometry.

2.2.5 Onset of Additional Reactions

Our analysis assumes dissociation and ionization reactions are driven solely by electron collisions with heavy (molecular and atomic) propellant species. Here, we examine the onset of various other reaction processes to identify the approximate regimes in which this assumption is valid.

Reactions between Heavy Species

As the pressure within the thruster increases collisions between heavy species can begin to dominate over collisions with electrons. In this limit reactions driven by heavy species collisions (e.g. $H + H_2O \rightarrow H_2 + OH$) become significant. The mean free path of species j undergoing reactions with species k is given by $\lambda_{j,k} = (n_k \sigma_{j,k})^{-1}$, where $\sigma_{j,k}$ is the reaction cross-section. Reactions between species j and k can therefore be neglected if $L < \lambda_{j,k}$. This condition may be expressed in terms of the quantity $p_0 L$ as

$$p_0 L < \frac{k_b T_n}{(n_k/n_0)\,\sigma_{j,k}}. \tag{2.24}$$

For water vapor propellant, maximum cross sections for reactions between heavy neutral species are typically on the order $\sigma_{j,k} \sim 10^{-24} - 10^{-20}$ m^2 [70]. The results of our model generally show that $n_k/n_0 \lesssim 0.1 \;\forall\; k \in [\mathrm{OH}, \mathrm{O}, \mathrm{H}]$. This suggests that heavy neutral species reactions can be neglected for $p_0 L \lesssim 30$ mTorr·m.

Larger cross-sections ($\sigma_{j,k} \sim 10^{-20} - 10^{-18}$ m^2) have been observed for reactions between neutral water and different ionized species, such as charge transfer (e.g. $O^+ + H_2O \rightarrow H_2O^+ + O$ [72]), dissociative charge transfer, (e.g. $O^+ + H_2O \rightarrow OH^+ + OH$ [72]), and proton transfer (e.g. $H_2O^+ + H_2O \rightarrow H_3O^+ + OH$ [76]) reactions. Fig. 2.2 indicates that O^+ and H_2O do not coexist in appreciable quantities for the conditions considered here, which suggests that charge transfer reactions and dissociative charge transfer between O^+ and H_2O can be neglected. Furthermore, the proton transfer reaction is generally much slower than electron-driven reactions for $T_e > 5$ eV [103]. As a result, neutral H_2O is consumed via electron

collisions before a substantial quantity of H_3O^+ can be created via proton transfer.

Photon-Driven Reactions

Reactions can also occur by virtue of photons (p) interacting with plasma molecules or atoms. Photodissociation (e.g. $H_2O + p \rightarrow H + OH$ [71]), photoionization (e.g. $H_2O + p \rightarrow H_2O^+$ [145]), and dissociative photoionization (e.g. $H_2O + p \rightarrow H + OH^+ + e^-$ [18]) are three examples of photon-driven reactions. The maximum cross-section for these types of reactions are typically on the order $\sigma \sim 10^{-24} - 10^{-21}$ m^2. These relatively small cross-sections suggest that photon-driven reactions can similarly be neglected for $p_0 L \lesssim 30$ mTorr·m.

Radiative and Dielectronic Recombination

Electron collisions with plasma ions can produce radiative (e.g. $H^+ + e^- \rightarrow H + p$) and dielectronic (e.g. $H^+ + e^- \rightarrow H^* \rightarrow H + p$) recombination reactions. The density rate of change of ion species j due to these reactions is $\dot{n}_{j,3r} = -\alpha_j n_j n_e$, where α_j is the sum of the radiative and dielectric recombination rate coefficients. The loss rate of ion species j via recombination is small compared to convection for

$$p_0 L < \frac{k_b T_n c_j}{\alpha_j}. \tag{2.25}$$

Here, c_j represents the ion acoustic speed of species j. For singly-charged ions with $T_e \sim 1 - 40$ eV, the maximum recombination rate coefficient generally falls within the range $\alpha_j \sim 10^{-20} - 10^{-17}$ m^3/s [58]. As a result, radiative and dielectric recombination reactions can typically be neglected for $p_0 L < 10$ mTorr·m.

Three-Body Recombination

Collisional three-body recombination describes the process whereby an ion recombines into a neutral particle following an interaction with two free electrons. (e.g. $H^+ + e^- + e^- \rightarrow H + e$). The density rate of change of ion species j due to this process is $\dot{n}_{j,3r} = -\beta_j n_j n_e^2$, where β_j is

the recombination rate coefficient. Comparing this rate to the convective loss rate of species j, and recalling that $n_e/n_0 < 1$, we find that three-body recombination can be neglected for

$$p_0 L < k_b T_n \sqrt{\frac{c_j L}{\beta_j}}. \tag{2.26}$$

Using H_2O^+ as an example ($\beta_{H_2O^+} \approx 10^{-38} T_{ev}^{-9/2}$ [m^6/s][4]) and considering $L = 15$ mm and $T_e = 5$ eV, Eq. (2.26) predicts that ion depletion via three-body recombination is insignificant for $p_0 L < 100$ mTorr·m. We note that three-body recombination plays an important role in low-temperature ($T_e \sim 1$ eV), high-pressure ($p_0 L \sim 10^3$ mTorr·m) EP devices such as arcjets [144]. It is the strong scaling of α_j with T_e that effectively suppresses three-body recombination at the conditions relevant to the low-pressure EP plasmas considered here.

2.3 Conclusion

This chapter presents a 1D global model of molecular plasma composition in a cylindrically symmetric thruster to examine the effects of dissociation on thruster performance. We established a control volume model and evolved chemical kinetics equations axially to determine species concentrations along the length of the thruster. These concentrations determine thruster performance, as higher-velocity, less dissociated ions increase efficiency and specific impulse.

Water vapor plasma composition was found to be a function of both thruster length times pressure ($p_0 L$) and electron temperature. Near propellant injection (small $p_0 L$), the plasma consists primarily of molecular ions and neutral fragments; this region corresponds to the highest average ion mass and the lowest ion cost. As these molecules dissociate, atomic neutrals begin to populate the plasma, increasing ion cost and decreasing ionization fraction for lower electron temperatures. For large $p_0 L$, these neutrals ionize, and the atomic ions accelerate through the magnetic nozzle. Increasing electron temperature from 5 to 20 eV extends the region dominated by molecular ions and reduces the concentration of neutral molecules and atoms.

Unlike an atomic plasma, a water vapor plasma with a given electron temperature was found to exhibit a peak in ionization percentage corresponding to higher-mass ions that subsequently recombine and dissociate into atomic species. This peak corresponds to a $(P/\dot{m})^*$ that represents a critical value suggesting a distinct operating regime for water vapor propellant with thrust efficiency and specific impulse comparable to state of the art EP devices such as Hall thrusters and gridded ion engines [89]. The optimal operating regime requires $p_0 L^*$ between 0.03 and 0.3 mTorr·m and $T_e > 15$ eV. These conditions correspond to $P/\dot{m} > 0.8$ kW/mg/s and enable specific impulses between 2,000 and 4,000 s. This novel behavior is not captured in earlier models [102] that do not consider dissociation or transit times. We note that current experiments on electrodeless thrusters operate well below the optimal values calculated here: an ECR thruster working with argon [55] at $\dot{m}u_n L/A \sim 2,400$ mg/s^2 and $P/\dot{m} \sim 0.25$ kW/mg/s may drop from a maximum thrust efficiency of $\sim 65\%$ on argon to $\sim 30\%$ if operated with water vapor at the same conditions; the AQUAJET thruster [126] working with water vapor at $\dot{m}u_n L/A \sim 4,700$ mg/s^2 and $P/\dot{m} \sim 0.5$ kW/mg/s would produce a maximum of 2,000 s I_{sp} and 40% thrust efficiency; and a helicon thruster that has been tested with molecular propellants [25] at $\dot{m}u_n L/A \sim 40,000$ mg/s^2 and $P/\dot{m} \sim 0.03$ kW/mg/s is below the calculated values shown in Fig. 2.5.

The difference between molecular and atomic propellant performance highlights the importance of being able to describe the principle design laws. Our model suggests that operation on water can achieve reasonable performance within engineering constraints; mass flow rate, thruster geometry, and power can be tailored to design a plasma source that preferentially creates singly-ionized, heavy molecules from water (H_2O^+ and OH^+). These design constraints are integral to successful operation of these thrusters. Furthermore, our work demonstrates that thruster performance with molecular propellants is not monotonic in the absence of wall and coupling losses, contrary to what has been shown for atomic propellants.

The rest of this dissertation describes our experimental efforts to validate and verify these conclusions. While the conclusions drawn in this chapter indicate that the thruster is theoretically feasible, in subsequent chapters we assess whether we are able to realize this

performance in the lab and determine the practicality of building an EP thruster to operate on water vapor.

Chapter 3
EXPERIMENTAL DESIGN

The theoretical background derived in Chapter 2 informs our experimental thruster design. Electrodeless thrusters are less likely to suffer from oxidation or corrosion from water vapor propellant, and, of the various electrodeless thruster concepts (radio frequency, helicon, field reverse configuration, etc), electron cyclotron resonance (ECR) thrusters offer the most control over electron temperature, shown to be an important parameter in controlling plasma composition. Furthermore, ECR thrusters have experienced somewhat of a resurgence in recent years, with several groups exploring their operation on both noble gases and molecular propellants, to include water [139, 126, 140]. By incorporating our theoretical understanding of performance regimes with the experimental efforts, we verify the model and explore higher power regimes predicted to correlate with higher performance. Explicitly, we are targeting operation for $T_e > 15$ eV, which corresponds to $P/\dot{m} > 0.8$ kW/mg/s.

3.1 Facilities

All testing described in this work was undertaken in the SPACE Lab Test Facility (STF), shown in Fig. 3.1. STF consists of a 1.4 m diameter spherical section with 108 ports for view and diagnostic access. A 1 m diameter by 1.7 m long cylindrical extension is added to this spherical chamber to incorporate additional pumping capability and increase chamber volume for plume expansion. The STF chamber walls are stainless steel, but no effects of sputtering were observed on the test article. STF has three cryopumps, one turbomolecular pump, and one roughing pump which give a capability of 25,000 L/s on nitrogen and 70,000 L/s on water vapor. All results presented in this dissertation were tested using one Sumitomo Marathon CP-20 cryopump, plus the Shimadzu TMP-V2304LMP turbopump,

giving a pumping speed of 29,000 L/s on water and 10,000 L/s on argon. The base pressure for the facility is 2×10^{-7} Torr and pressure during testing never exceeded 2×10^{-5} Torr. To protect the cryopumps from energetic ions impinging the louvers, a beam dump is placed 0.75 m from the junction between the two chambers. The beam dump is constructed of aluminum supports covered in 1/32" graphoil and is water-cooled at a rate of 2 gal/min.

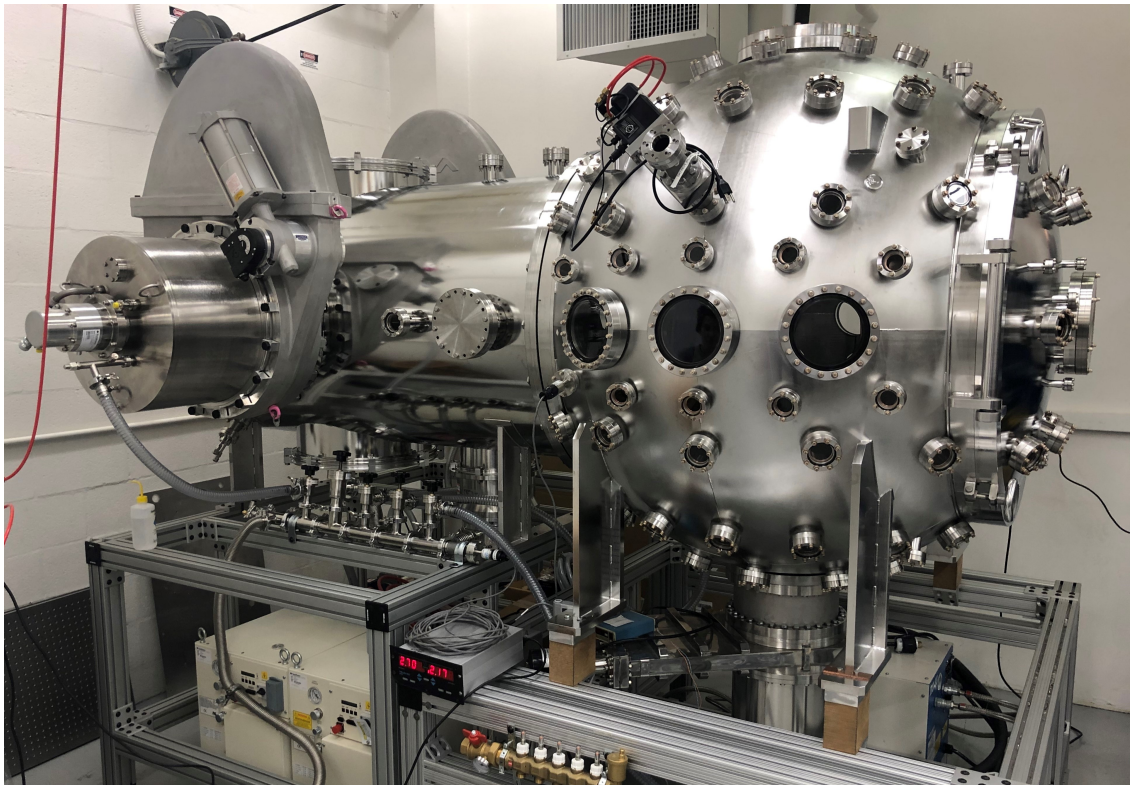

Figure 3.1: The SPACE Lab Test Facility.

3.2 Thruster Design

The SPACE Lab Alternative Propellant ECR eXperimental (APEX) thruster built for these experiments is derived from ECR thrusters developed at PEPL [140] and is similar to those tested at ONERA [139]. In the following subsections, we review previous research into ECR thrusters and describe the APEX thruster as tested. As detailed, the initial APEX

thruster suffered from thruster-rich combustion, and the thruster was modified to ensure survivability during high power testing. All data presented in later chapters is from the second, more robust APEX thruster.

3.2.1 History of ECR Thrusters

Researchers have explored ECR sources for use as electric propulsion devices intermittently since the 1960's [67, 117, 55]. Early concepts used waveguides and vacuum windows to launch microwaves into a resonant cavity with an axial magnetic field. Pre-ionization is not required, as the RF is sufficient to generate seed electrons that are subsequently heated by cyclotron resonance. The size of these devices depends on the microwave frequency and the waveguide required to launch the wave. NASA Lewis in the 1960's used a 1 kW, 8.35 GHz source to launch a TE11 wave into a resonant chamber using argon and xenon propellant [67]. The ECR zone is located outside the thruster cross-section, approximately 1 - 2 cm from the exit plane of the thruster. This geometry means that the acceleration and heating take place outside the thruster, which the authors speculate is responsible for the high-power efficiency of the thruster. However, background gas may also be ionized in this configuration, and these ions contribute to higher densities and lower ion energy. Nevertheless, the authors measured a 13 - 19° divergence angle, showing the ion beam coherence and feasibility for space propulsion. In the 1990's, researchers at Cal Tech developed a 2.12 GHz waveguide thruster with the resonance zone just inside the thruster channel. Results showed that plasma potential and electron temperature decrease as background pressure increases and that plasma potential and ion energy are largely unaffected by increasing power [61, 60]. Higher powers do increase ion flux [60]. Thruster performance results are lackluster: calculated propulsive efficiency is $\sim$20% ignoring nozzle losses, calculated specific impulse with hydrogen is around 15,000 s, and mass utilization efficiency $> 100\%$ at some points due to background pressure effects [60].

Since the early 2010's, researchers at ONERA have studied coaxial ECR thrusters [55], enabling a smaller thruster size ($\sim$1.5 cm vs $\gtrsim$3.5 cm in diameter for 2.45 GHz). Having

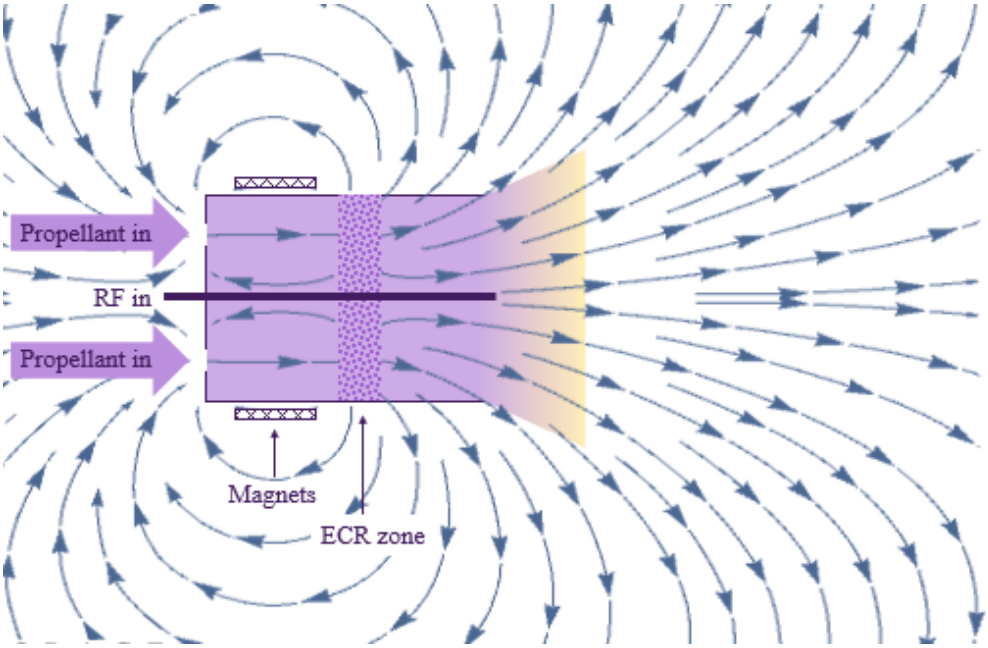

Figure 3.2: Schematic of a coaxial ECR source.

a smaller geometry also makes it easier to create the magnetic nozzle, by using permanent magnets or less current through electromagnets. Coaxial ECR thrusters have been investigated using a variety of plume and thruster diagnostics: a retarding potential analyzer (RPA) and Faraday cup to determine the angular variation of the plume and calculate the thrust [55]; laser induced fluorescence (LIF) to investigate the acceleration of xenon ions through the magnetic nozzle [141, 54, 29]; and torsional [92, 107] and nulled pendulum [138] thrust stands to measure the produced thrust. Integration of an analytic model of the discharge [19] and tuning experiments [21, 139, 138] refined the magnetic field configuration and thruster geometry such that thrust efficiency with xenon quadrupled from 4% to 16%. Other improvements, such as increasing the length of the ECR zone [21] or mixing frequencies to provide a secondary ECR zone [142], have not shown marked improvement over the conventional designs. Experiments with argon [55, 92] and krypton [139] showed lower thrust, efficiency, and specific impulse than xenon, but these propellants have not been tested on

more optimized thrusters. Performance increases as power increases from 20 to 50 W, but the bounds on this effect remain unknown. Some testing into higher powers (up to 170 W) with xenon agrees with this trend [107].

The literature suggests that the largest contributors to low thrust efficiency compared with other thrusters in this class are low mass utilization and low power conversion efficiency [55]. Mass utilization efficiency describes the fraction of the plume that is ionized, which represents both the likelihood of neutrals being ionized in the thruster and exhausting the thruster without recombining on the walls. This efficiency is driven by the ionization cost and cross section (i.e., species with lower ionization energies and higher cross sections at the electron temperatures in the thruster have higher mass utilization) [55] and the length of the thruster [106, 3], which should be sized such that the neutral transit timescale is longer than the ionization timescale. While wall losses in electrodeless thrusters are expected to be small, provided the magnetic field is parallel to the walls and strong enough to limit electron mobility [3], Sánchez-Villar et al modeled the characteristics of a xenon plasma in a coaxial ECR thruster and found wall losses accounted for two thirds of the energy loss, with losses concentrated along the central antenna, substantial along the backwall of the thruster, and an order of magnitude less on the lateral walls [111]. The relative importance of these wall losses on the performance with other propellants is not known. Furthermore, while water vapor has been studied theoretically [102, 121] and experimentally [92], the main loss mechanisms for molecular propellants remain an open question. Molecular propellants are found to have higher frozen flow losses, due to the increased likelihood of dissociation and multistep ionization pathways for species products [35]. No experimental results have explored the presence of multiply charged ions in ECR plasmas, although ExB probe analysis on Hall thrusters suggests increased plasma density correlates to higher fractions of multiply charged ions [17] and that higher ionization energies should correspond to lower fractions [74]. Extrapolating Hall thruster research to ECR thruster behavior is not necessarily straightforward, as research suggests discrepancies between the two devices: Faraday probes measure lower ion current and increased divergence with increased background pressure on an ECR

thruster [139], while a higher ion current and constant divergence is measured with increased background pressure for Hall thrusters [143]; likewise, LIF shows a decrease in ion velocity with increased background pressure for ECR thrusters [141] instead of staying constant for Hall thrusters [86]. This suggests that understanding plasma interactions with background neutrals is critical for these devices, especially considering mass utilization in the channel and downstream in the plume.

3.2.2 Magnetic Field

The magnetic field in an ECR thruster must be carefully designed to ensure the ECR region is located in an optimal location within the thruster channel. Early on in the design process, we specified the frequency for the thruster (2.45 GHz), which dictated the peak magnetic field strength required (875 G). Permanent magnets provide a compact, strong magnetic field, but are less flexible in modifying the field compared with electromagnets. In order to achieve this field, we use commercially available, permanent N42 ring magnets, each of which is 3" OD, 1.5" ID, and 1/4" thick. Six magnets are used as the baseline case, providing the requisite magnetic field strength.

We use an axial Gaussmeter to measure the axial magnetic field at different axial and radial points and compare to a FEMM 4.2 calculation, as shown in Fig. 3.3. The agreement is within 1%, and we use the simulated results to describe the magnetic field in the far field.

One additional concern with using permanent magnets in a thruster is the demagnetization at high temperature. For the magnets used in these experiments, the maximum operating temperature is 80°C. This constraint necessitates thermal consideration; specifically, we must monitor the temperature and limit the time of high power testing. Water cooling would reduce the temporal limits on this experiment, but, due to the sensitivity of the thrust stand, this added complexity is avoided.

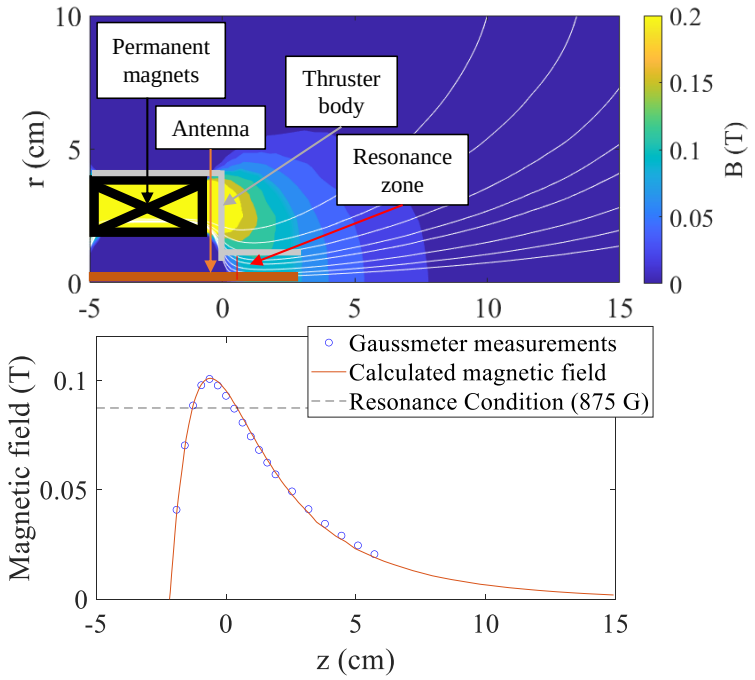

Figure 3.3: Contour map of the magnetic field strength, as calculated using FEMM, with the magnetic field lines shown in black (top) and plot of the centerline magnetic field showing good agreement between values calculated using FEMM and measurements made with a perpendicular Gaussmeter (bottom).

3.2.3 APEX Thruster, v1

The v1 APEX thruster was derived from the University of Michigan's ECR thruster experiment [140], but modified for different magnetic components and to incorporate additional considerations to prevent erosion or contamination from the water vapor plasma. The main body is made from aluminum, for both ease of machining and permeability of the magnetic field (e.g., ferrous metals would perturb the magnetic field). Ceramic Macor sleeves were designed to protect the coaxial antenna and thruster walls. Modularity ensures that thruster components (e.g., antenna length, thruster channel dimensions, etc) are variable and can be thoroughly inspected for damage from operation.

The first version of the APEX thruster utilizes a bulkhead N type adapter with a 3mm-0.5 metric threaded antenna. This antenna is used with threaded Macor sleeve, which increases its overall diameter to 0.64 cm. The aluminum thruster channel is 2.54 cm in diameter, and the Macor insert reduces the inner diameter of the thruster to 2.18 cm. The assembled thruster is shown in Fig 3.4, and a CAD rendering of the inner dimensions is shown in Fig 3.5.

This design incorporates a gas reservoir/plenum for even azimuthal distribution of the propellant into the thruster channel and a spacing behind the thruster channel for even axial distribution. This distribution space, however, provided a cavity of high density gas that is exposed to microwave energy, which proved to be the downfall of APEX v1. Plasma was viewed forming in the gas plenum, as shown in Fig 3.6, but no signs of damage appeared in this region during thruster disassembly. In order to ensure components are well-clamped together such that no gas can escape, helicoil inserts were added to the thruster face to strengthen the tapped holes in the aluminum thruster body. These efforts did eliminate visual evidence of plasma formation. However, the dark space remained, and thruster operation did not improve. Subsequent efforts to fill this space with 1 mm alumina milling balls did not have any apparent influence on thruster performance.

Certain test conditions produced a plasma in this region in the rear of the thruster, as shown in Fig 3.7. This plasma wrecked havoc on the N type bulkhead connector used as the RF antenna, shown in Fig 3.8; some engineering control must be designed to prevent the melting and consumption of the nylon spacer integral to the connector. Early experiments tested ceramic paper and two ceramic epoxies (Cotronics 940LE and 780). The ceramic paper appeared to suffer from outgassing, becoming flaky after being exposed to thruster conditions, and the ceramic epoxies were also deemed unsuitable – at the small scales necessary, they did not have the strength or density required. The ultimate solution to filling this space is shown in the CAD rendering, Fig. 3.5, with a solid Macor spacer filling the entire volume. However, the residual volume behind the thruster needed to be sufficiently porous to distribute the propellant gas. We attempted to mitigate the pressure times distance of the non-thruster-channel spaces of the thruster, in accordance with Paschen's law, which dictates the voltage

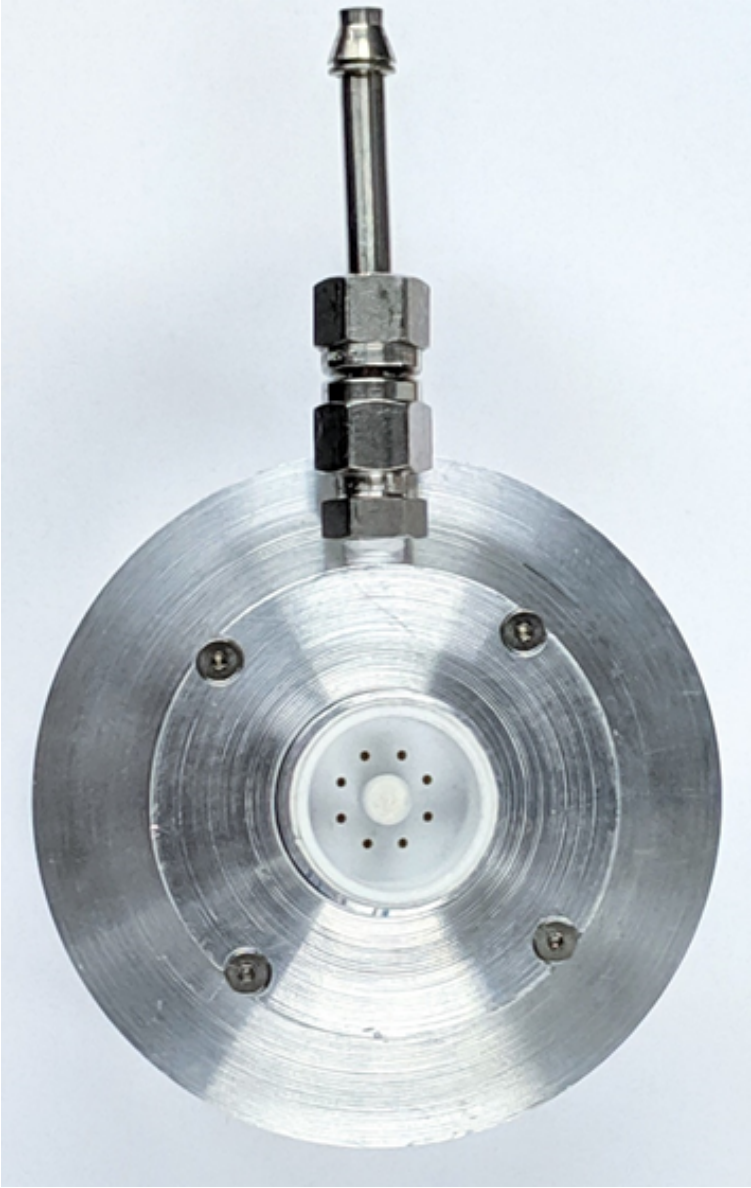

Figure 3.4: Image of the v1 APEX thruster with axial propellant injection. For scale, the inner diameter is 1/4".

required to initiate a plasma breakdown [99], but these efforts were unsuccessful. A succession of images is shown in Fig. 3.8 of the destruction wrecked by unintended plasma. Both conductive and insulating materials were tested for filling the negative space; conductive

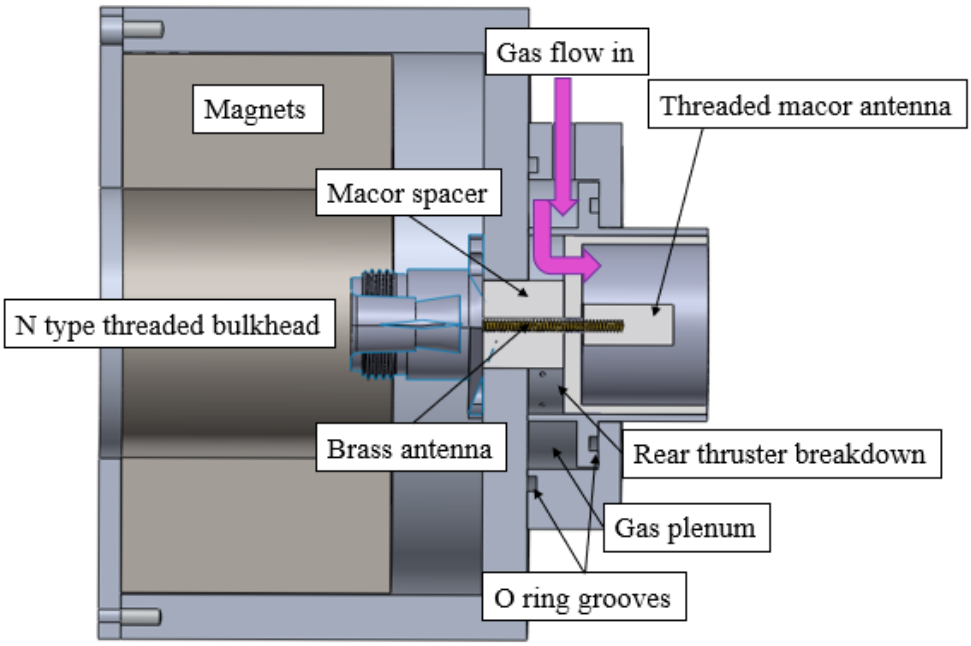

Figure 3.5: CAD model slice showing the inner dimensions of the v1 APEX thruster with axial propellant injection. For scale, the inner diameter is 1/4".

materials coupled to the RF, prevented discharge, and were therefore quickly abandoned.

However, the insulators tested covered a gamut of materials: porous polyimide foam, a stack of ceramic paper sheets, 1 mm alumina milling balls, and 10 μm porous glass. The polyimide foam had been tested previously for gas distribution in a pulsed inductive thruster in the SPACE Lab but was consumed in plasma breakdown in the back of the thruster. The stack of ceramic paper sheets had some outgassing associated with it, and a discharge was formed between the layers. Packing the 1 mm alumina milling balls inherently involved unknown void fraction, similar to that common with catalyst packing in the monopropellant community. Even at dense packs, plasma still formed in this region, causing charring on some of the alumina balls and leading to questions of purity. The porous glass appeared to work, but the v1 APEX thruster was abandoned before the failure mechanism of the porous

Figure 3.6: Image of plasma forming in the plenum region of the thruster.

glass could be determined and there was difficulty in machining the porous glass.

Further concerns regarding the suitability of the v1 APEX thruster resulted from the deterioration of the brass threaded antenna. Brass is an unsuitable thruster component, due to the low vapor pressure of zinc. As the antenna was exposed to the vacuum and subjected to moderate heat loading from the plasma, the zinc migrated to the surface of the antenna and subsequently sublimated, even when protected by a threaded Macor cover, Fig. 3.9. In addition, the heat loading on the antenna gradually softened the connector insulating material and caused arcing in the cable connectors. These issues, along with the unintentional plasma formation in the rear of the thruster ultimately drove the decision to redesign the thruster, leading to the v2 APEX thruster.

3.2.4 APEX Thruster, v2

The improved APEX thruster was designed specifically with (1) higher power RF connectors that were further removed from the plasma source and (2) no high density gas regions outside

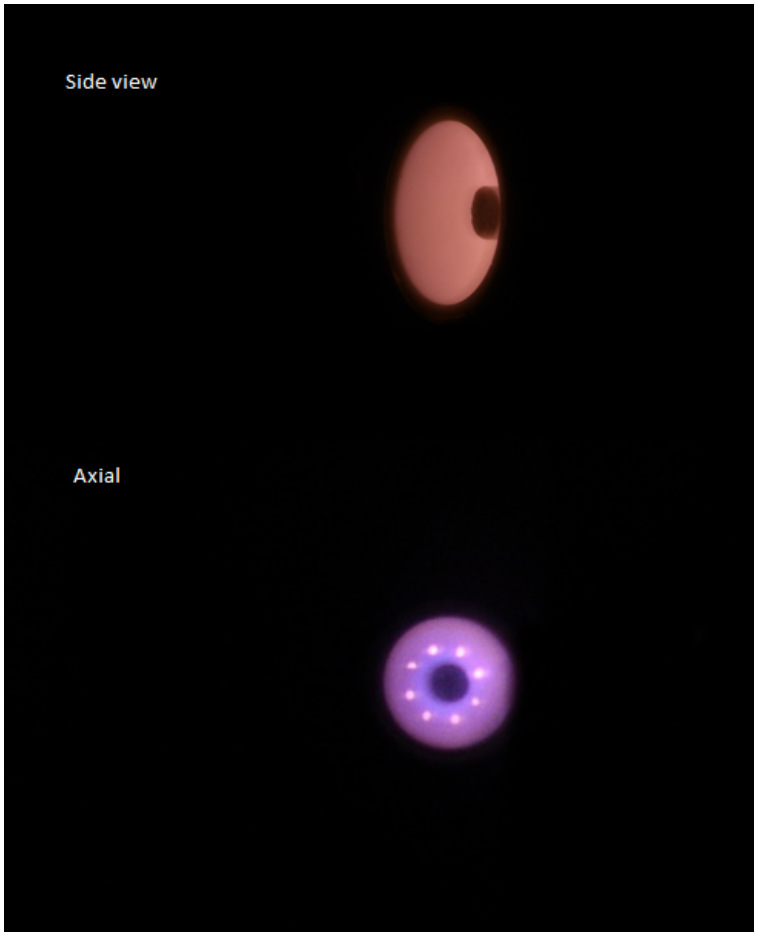

Figure 3.7: 45° angle side (top) and end-on (bottom) view of plasma forming in the plenum region of the thruster.

of the thruster channel. In order to accomplish this, we switched from N type to 7/16 DIN connectors. The 7/16 DIN series is designed for higher power loading (2 kW) compared with the N series (500 W). Furthermore, the thruster antenna was reimagined as a continuation from a coaxial assembly. The antenna is a solid 1/8" copper rod fitted inside a 1/4" OD alumina tube. The end of the alumina tube is capped with Aron-D ceramic (a one-part ceramic epoxy that consists largely of alumina and silica). The solid copper is the same dimensions as the center conductor in standard LMR-400 RF cable, and the alumina is

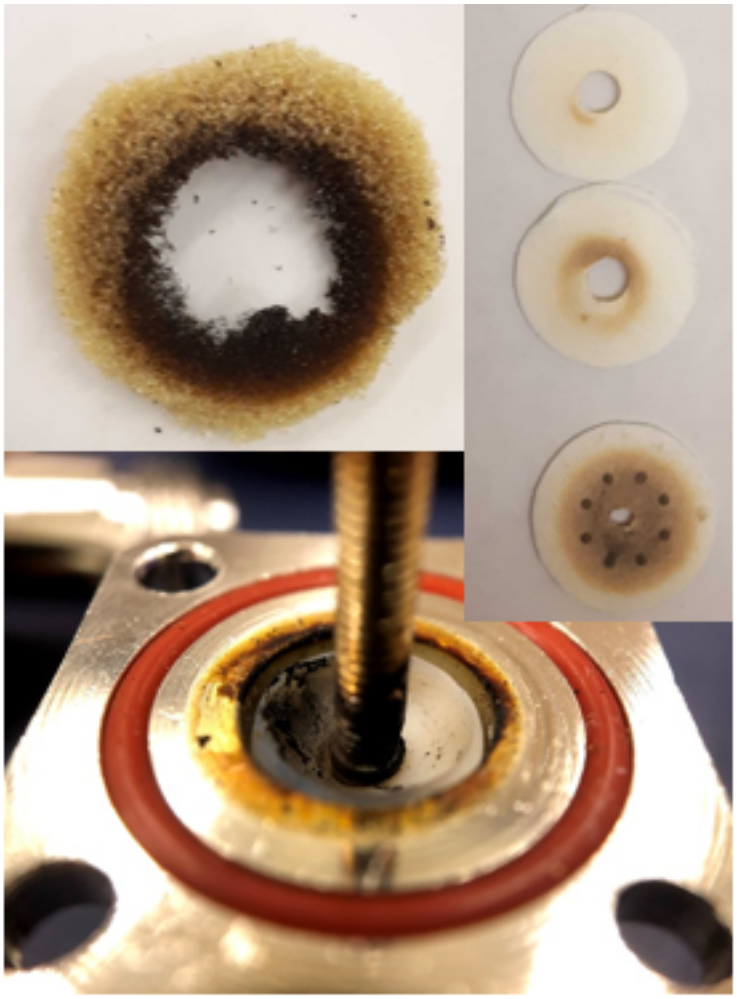

Figure 3.8: Images of destruction wrought by unwanted plasma. Shown here is the polyimide foam (top left), ceramic paper (top right), and the surface arcing on the threaded bulkhead connector that occurs without any protection (bottom).

approximately the same size as the insulator in that same cable. A 3/8" OD aluminum tube serves as the coax shielding and gas distribution. These antenna components are assembled and connected to a 7/16 DIN bulkhead connector designed for LMR-400 cable.

Mitigating the dark space in the thruster required a redesign of the gas injection scheme from the v1 APEX thruster. The new design, shown in Fig. 3.10, axially injected gas near

Figure 3.9: Image showing the zinc vaporization present in the threaded N type connectors after exposure to the thruster environment. The N type connector on the left was fired in vacuum, while the connector on the right was not.

the central antenna via four flutes, as shown in the CAD rendering in Fig. 3.11, with a circumferential groove that allowed the gas to spread radially. The smaller dimensions of the gas distribution region mitigated plasma formation, and no effects of unintended plasma were observed.

However, the new antenna configuration provided its own difficulties. Arcing occurred between the alumina sleeve and the copper antenna, as evidenced by charring on the antenna itself. While this arcing was intermittent and plasma ignition could usually be obtained by increasing gas flow, we could not ascertain the actual power deposited into the plume vs into the arc. A modification to the antenna shroud was further necessitated by observations of said shroud glowing red hot after operation at high powers or flow rates, as shown in Fig 3.12. We postulated different reasons for this heating: ion impingement onto the shroud, direct heating of the alumina, indirect heating of the alumina by the copper antenna, and effects of the arcing. As such, we modified the antenna shield to mitigate these potential

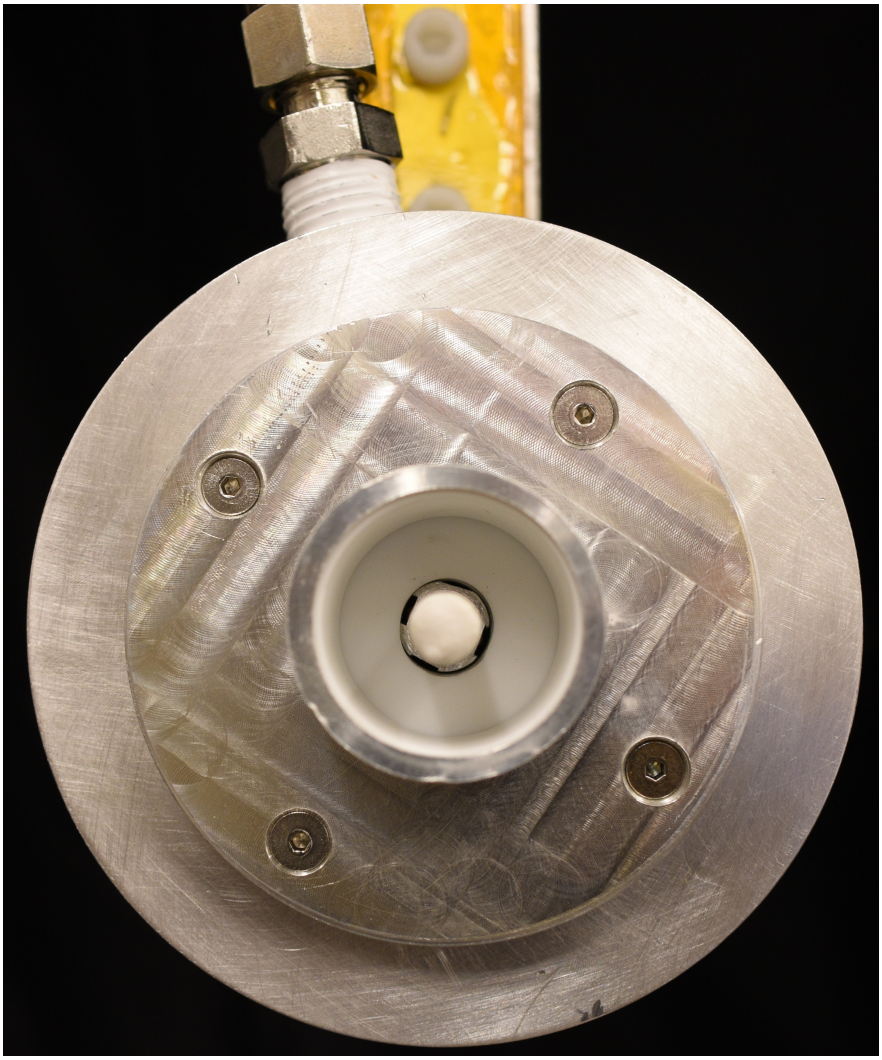

Figure 3.10: Image of the APEX v2 thruster.

causes.

Initially, we installed a fused quartz tube over the antenna, which served two purposes: (1) the transparency allowed us to see heating effects due to the copper and (2) quartz has a different RF absorption compared with alumina, which industrially is sintered using microwaves. The quartz tube was the same outer diameter as the alumina but a different inner diameter, meaning the fit over the copper antenna was not as tight. The thruster lit

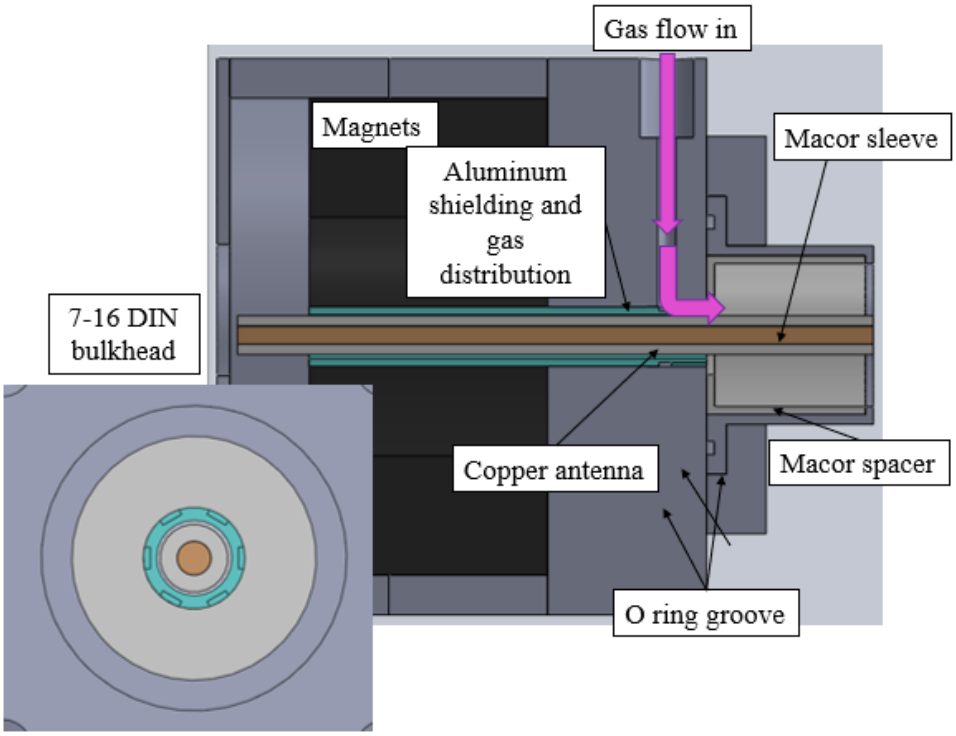

Figure 3.11: A Solidworks slice of the APEX v2 thruster.

with minimal difficulty, but evidence of arcing between the quartz and the copper antenna limited testing. These tests with the quartz showed no evidence of surface heating on the copper due to microwave transmission within in the thruster, but the quartz did glow in a similar manner to the alumina shroud. Heated quartz does not glow red, as one would expect; impurities on the surface might glow red hot, but the quartz itself is bright white/yellow, and then it emits strongly in the IR as you get closer to the melting point of the glass. We did notice that the quartz did appear to be glowing red, but this heating property of quartz indicates that, instead, it may be refracting light from deeper within the thruster. If the copper is glowing red beyond the view angles presented, it is likely due to arcing causing localized heating; resistive heating on the surface should be more global. Thus, the quartz tube met with only limited success in determining the cause of the alumina shroud heating.

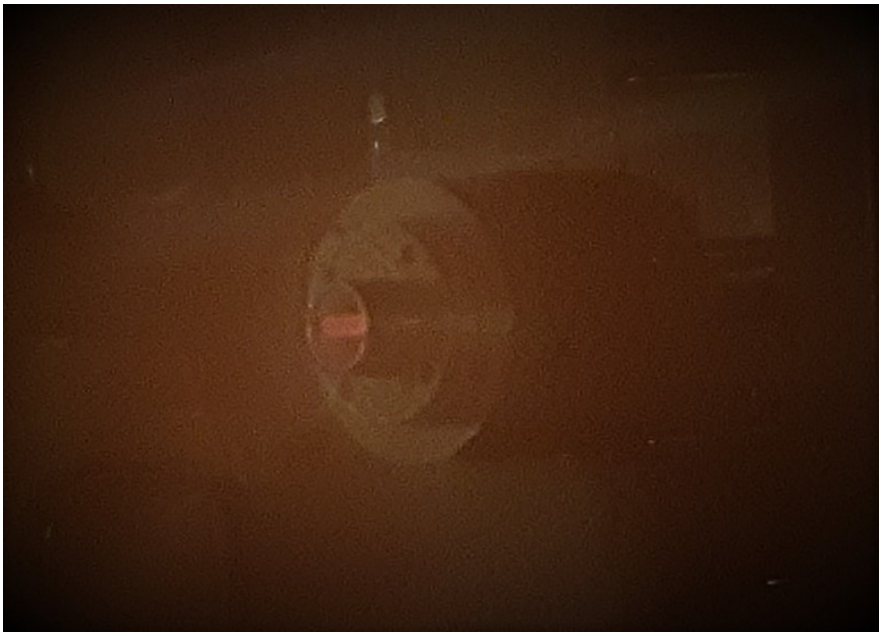

Figure 3.12: The alumina shield protecting the copper antenna is visibly glowing.

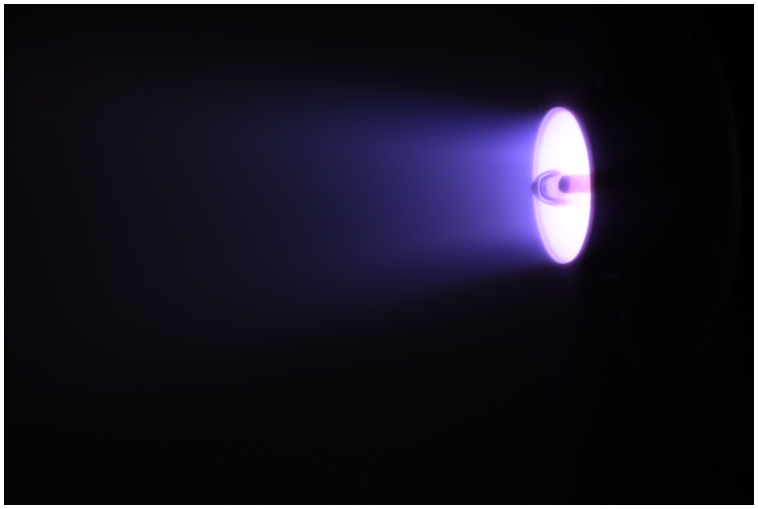

Figure 3.13: The APEX v2 thruster running with a fused quartz tube covering the antenna.

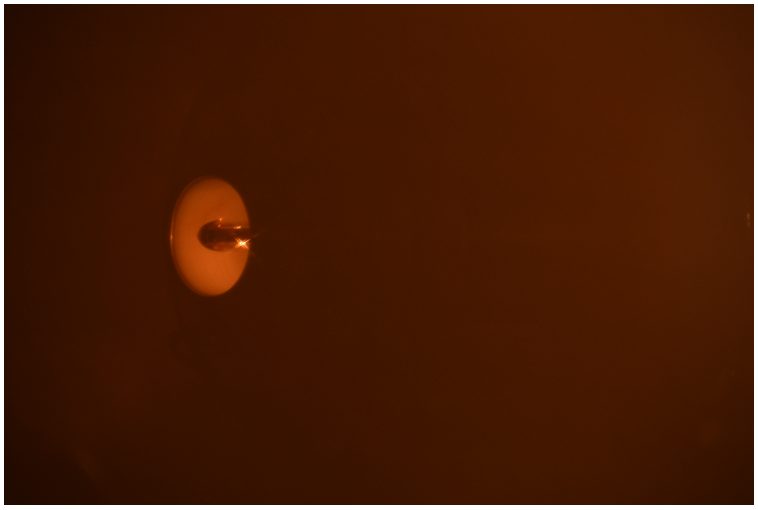

Figure 3.14: Evidence of an arc between the quartz shroud and the copper antenna.

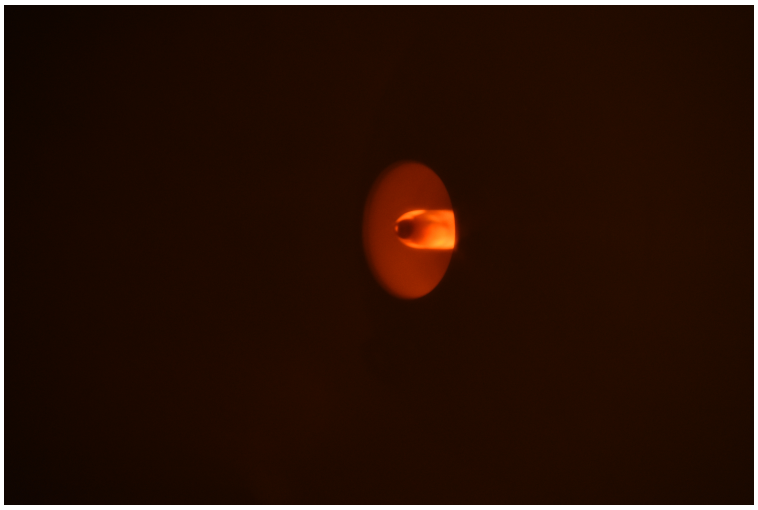

Figure 3.15: Evidence of heating the quartz shroud.

For both the alumina and quartz shroud, we saw evidence of surface plasmas (Fig. 3.16) occurring on the surface of the shroud. These surface plasmas occasionally formed during the ignition process but did not reliably translate into bulk ignition. Confronted with these complexities, we turned to the literature. Computational work published during the course

of the experiments [111] that found the electric field near the antenna is the driving force for effective power coupling. Between this computational evidence and the experimental complications, we decided to eliminate the insulating antenna shields from the thruster, while preserving the alumina insulation between the 7/16 DIN bulkhead connector and the back plane of the thruster. This approach maximizes the plasma near the maximized electric field while preventing damage to the power connector and is more similar to experimental efforts from other groups [141, 126].

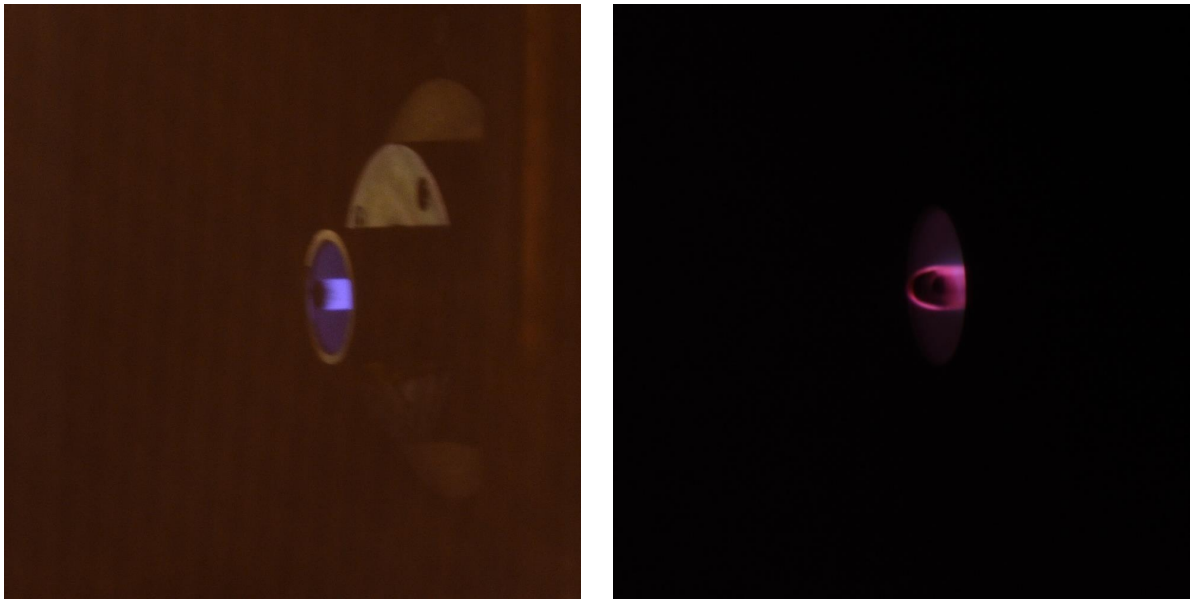

Figure 3.16: Surface plasmas on alumina (left) and quartz (right) shroud.

The bare antenna had an immediate impact on the visual appearance of the thruster plume. A bright, narrow jet formed around the antenna at approximately the radius of the earlier shields. This bright region is shown in Fig. 3.17. All data presented in this work is taken from this bare antenna configuration. However, this configuration is lifetime limited by erosion of the copper antenna by the plasma. Over the course of collecting data for this dissertation, the exposed part of the antenna decreased in diameter from 3.18 mm to 2.72mm. There is a clear distinction between the antenna sections exposed to plasma

and those protected by the alumina walls. The sputtered copper is partially redeposited on the insulating macor walls on the inside of the thruster (Fig. 3.18), and the thruster is cleaned during those occasions where the chamber is open over the course of testing. Following operation on water vapor, the exposed copper antenna has a patinated surface due to oxidation. Following operation on noble gases, the exposed copper antenna appears shiny/polished. Operation was not observed to be noticeably different operating with or without the copper deposition.

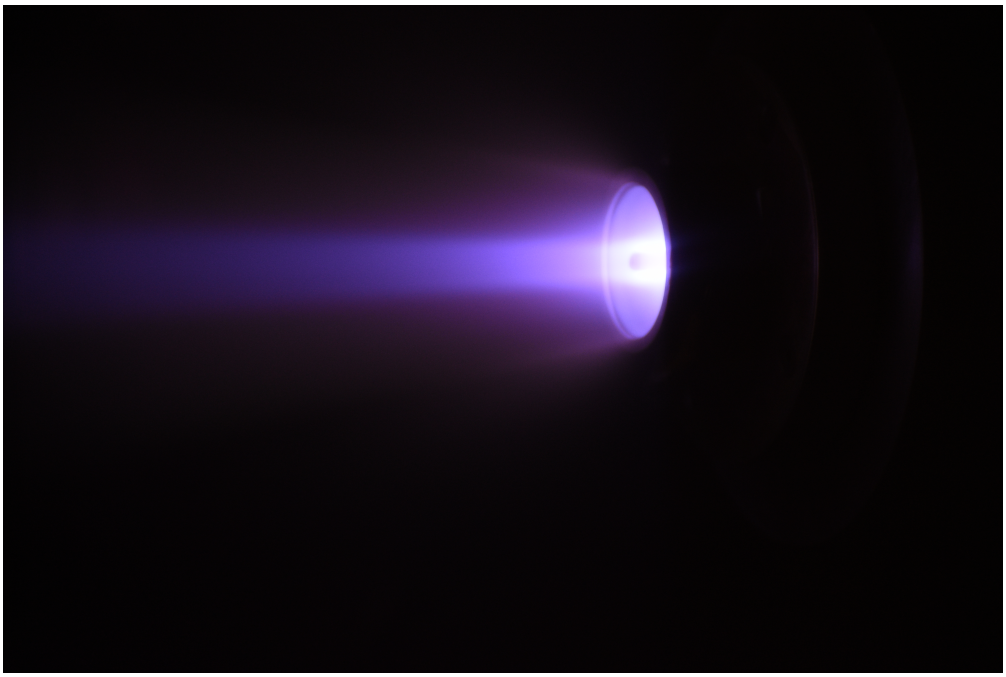

Figure 3.17: Thruster operation with a bare copper antenna.

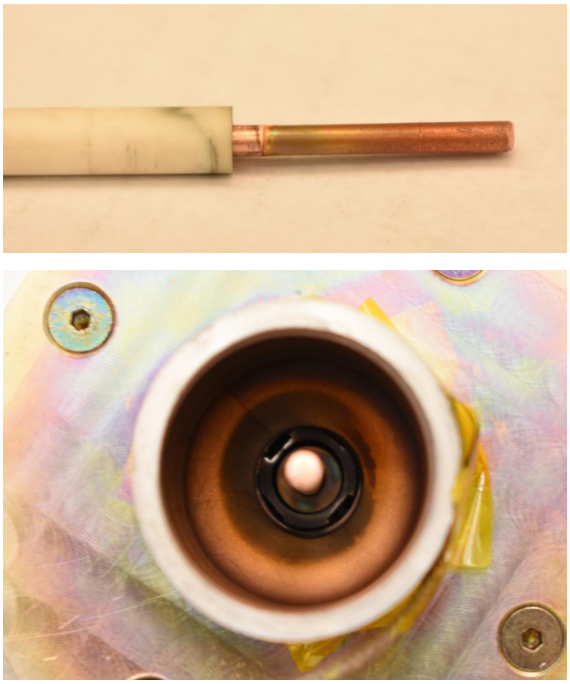

Figure 3.18: The patinated copper antenna, showing the demarcation between the protected and exposed sections of the antenna (top) and copper deposition on the thruster components (bottom).

3.3 Power Supply

Microwave power at 2.45 GHz is provided to the thruster by a Sairem GMS450 solid state coaxial 450 W supply via SPP375 corrugated coax cable with N type and 7/16 DIN connectors. A Narda 3022 dual directional coupler (DDC) is used to directly sample forward and reverse power to the thruster immediately prior to entering the vacuum chamber. As will be discussed below in Sec. 3.5.5, waveguides transmit power from the thrust stand shroud to the inverted pendulum thrust stand, and, overall, there is a 1.9 dB power loss in transmission between the dual directional coupler and the thruster as mounted inside the chamber. The thruster is electrically isolated from both the thrust stand and the STF. The overall power transmission is shown in Fig. 3.19.

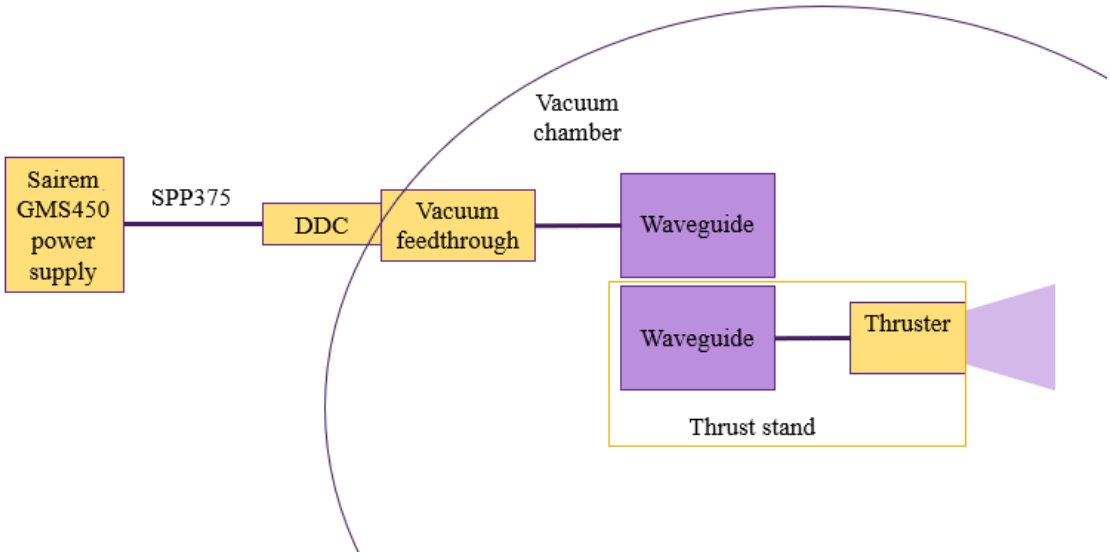

Figure 3.19: Microwave power transmission components.

The high power to mass flow ratio required for high performance necessitates a high-powered supply, and we expect thermal management to be a major concern in vacuum testing, especially with lower efficiencies. We placed thermocouples on the permanent magnets and main thruster channel in order to monitor temperature; the Curie point for the neodymium magnets is 80°C, and we cease operation whenever the magnet thermocouple exceeds 70°C.

3.4 Propellant Mass Flow Control

Because water is a liquid at standard operating conditions and freezes readily when introduced to vacuum, plumbing the water vapor propellant line requires some ingenuity. Standard gas mass flow controllers can operate with water vapor, but they are not robust to incidental liquid water, either through condensation on internal components or droplets entering the controller.

The vapor pressure of water at room temperature was too low for an Alicat 2.5 SLPM flow

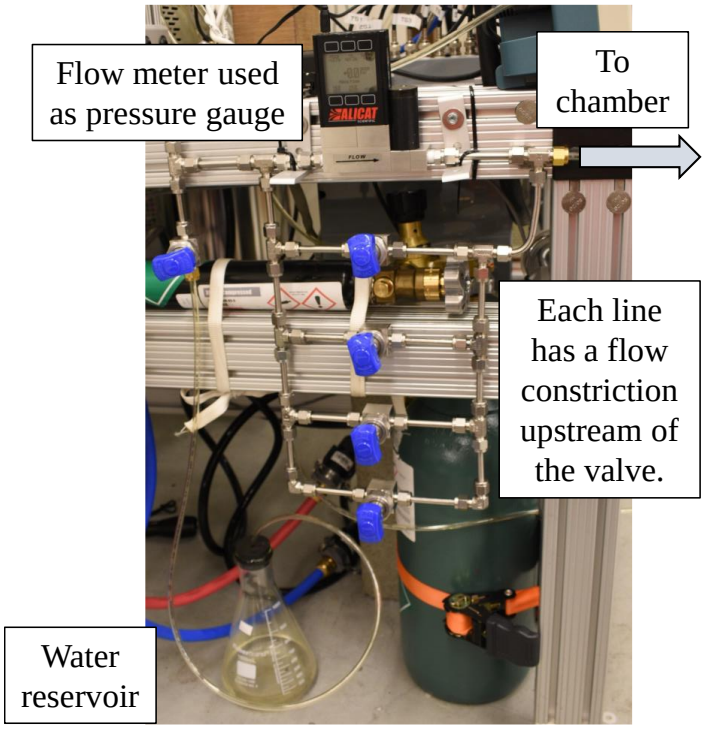

Figure 3.20: The water flow manifold as mounted next to the chamber. The flask of distilled water and the four valves representing different flow rates are shown. Only three valves were used during testing. The Alicat mounted here was used exclusively for measuring the backpressure of the line (0.31 psi during operation).

controller to sustain flow rates in the region of interest, and efforts to heat the water reservoir to increase the vapor pressure were insufficiently insulated, and liquid water condensed on lines leading to the flow controller, ultimately destroying it. Instead, a manifold consisting of a series of valves and flow constrictions (Fig. 3.20) was implemented in order to provide three different water vapor mass flow rates. An Erlenmeyer flask was halfway filled with deionized liquid water, and a rubber stopper was fitted into the top. A 1/4" surethane tube was inserted into this rubber seal, and the water vapor was tapped out of this line. In this manner, liquid water was separated from the water vapor by gravity. This line was split into three different lines, with a pressure sensor reading the upstream pressure. The three flow

rates were calculated by weighing the water reservoir before and after flowing gas. Due to the low mass flow of interest here, we ran these flow tests for on the order of one to two hours in order to evaporate a measurable amount of water. The water used during thruster testing was not measured; instead, we used the calculated flow rate, listed in Table 3.1.

Table 3.1: A table of water flow rates tested in the ECR thruster.

Valve Number	Calculated Mass Flow Rate (mg/s)	Standard Deviation (mg/s)
V1	0.362	0.022
V2	0.224	0.010
V3	0.136	0.013

The flow rates for the noble gas species was controlled using an Alicat 500M gas mass flow controller. The error in measurement is estimated at 0.2 sccm.

3.5 Diagnostics

In order to assess the composition of the molecular plasma, we need diagnostics that describe density of neutral, ion, and electron species, electron temperature, ion velocity, thrust, and thruster efficiency. These diagnostics must be (1) resilient to any plasma radicals, (2) unobstrusive to plasma flow, and (3) not affected by RF radiation. These requirements enable us to determine the effects of plasma chemistry on thruster operation without significantly modifying the collected data between propellants. Furthermore, we wanted to measure axial, radial, and angular variation of the plume. The diagnostics are explained in detail below, and a schematic of representative probes in the chamber is shown in Fig. 3.21.

3.5.1 Optical Emission Spectroscopy

Optical emission spectroscopy (OES) identifies molecular and atomic neutrals and ions based on characteristic emission from bound electrons. A 1" collimating lens focuses the signal to

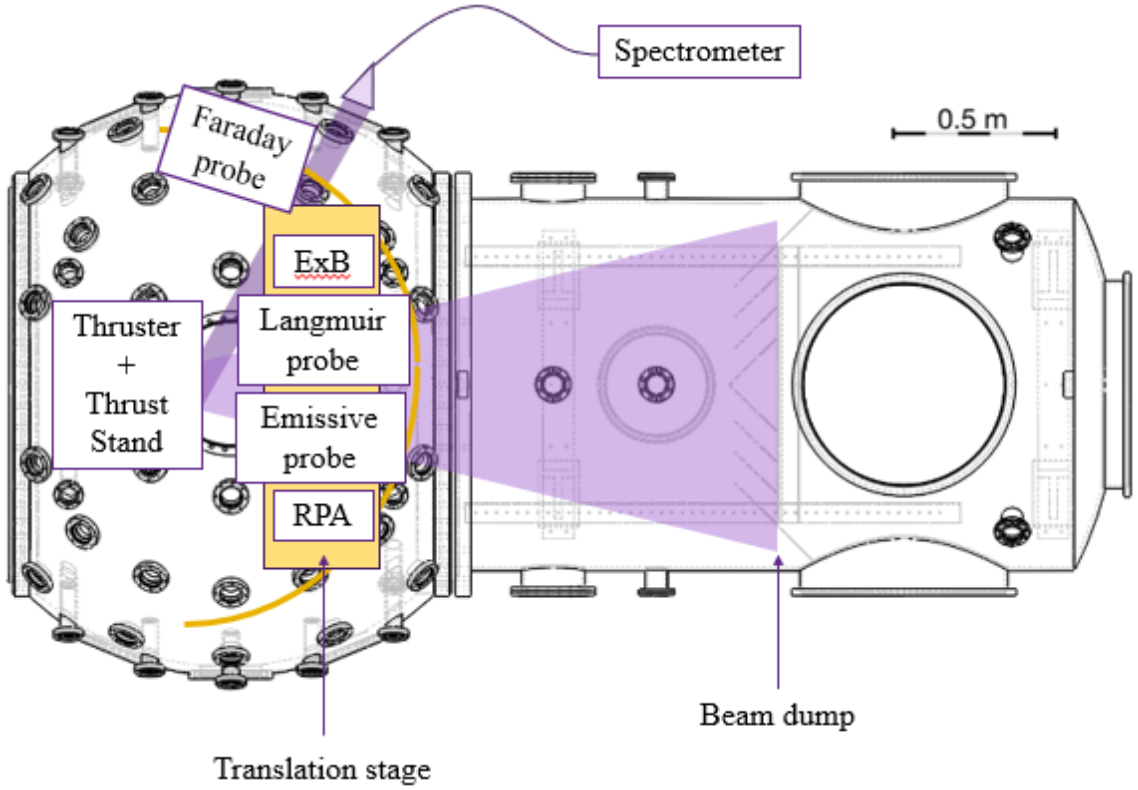

Figure 3.21: Schematic of diagnostic layout in STF.

400 μm, 1 m long fiber optic connected to the spectrometer. The lens is placed 0.95 m from the thruster exhaust plane. We use a ThorLabs Compact CCD (Charge Coupled Device) spectrometer with a 200 - 1000 nm range and $<$ 2 nm full width half maximum resolution. The collimating lens is mounted at a 45° angle to the thruster axis and centered on the thruster centerline at the exit plane of the thruster. The volume observed by the lens therefore incorporates a view approximately halfway into the thruster channel. The spectra are corrected for the sensitivity of the spectrometer. Since we are concerned with line intensities of dominant emissions and not with any line widening due to Doppler, Stark, Zeeman, or pressure broadening, the available spectrometer is sufficient for identifying different species. We identify dominant lines for atomic species from NIST [113] and for molecular species from

Table 3.2: Spectroscopic lines used for species identification.

Species	Line used for reference (nm)	Other strong lines visible (nm)
H_2O	927	n/a
OH	309	n/a
H	484	656, 433, 409
O	777	844
H_2O^+	746	n/a
OH^+	356	n/a
O^+	465	n/a

Pearse and Gaydon [100]. We use lines that are strong, distinct, and separated from potentially conflating lines in other expected species. The lines chosen are shown in Fig. 3.22 and listed in Table 3.2. The integration time is modulated to increase detection of the smaller peaks while avoiding saturation of the O I 777 nm line. This integration time ranged from 25 ms at high powers to 100 ms at lower powers.

There are several limitations to OES. First, it is a chord-averaged measurement, and the spatial resolution is correspondingly broad. In this case, we are observing all the light in a 2.54 cm diameter by 0.95 m volume. Second, some emission lines are not well disambiguated from other nearby lines or do not strongly emit in the visible. A spectrometer with a finer diffraction grating would be able to resolve close lines, but with a smaller wavelength range. Additionally, specialized spectrometers and optics are required for species that emit in the IR or UV. Furthermore, it is very difficult to derive quantitative measurements of species concentrations from OES, and we satisfy ourselves here with a qualitative assessment of the relative abundance.

Two sample spectra are shown in Fig. 3.22 to show the difference in emission at low and high power. The water vapor plasma spectrum shows clear peaks corresponding to O and

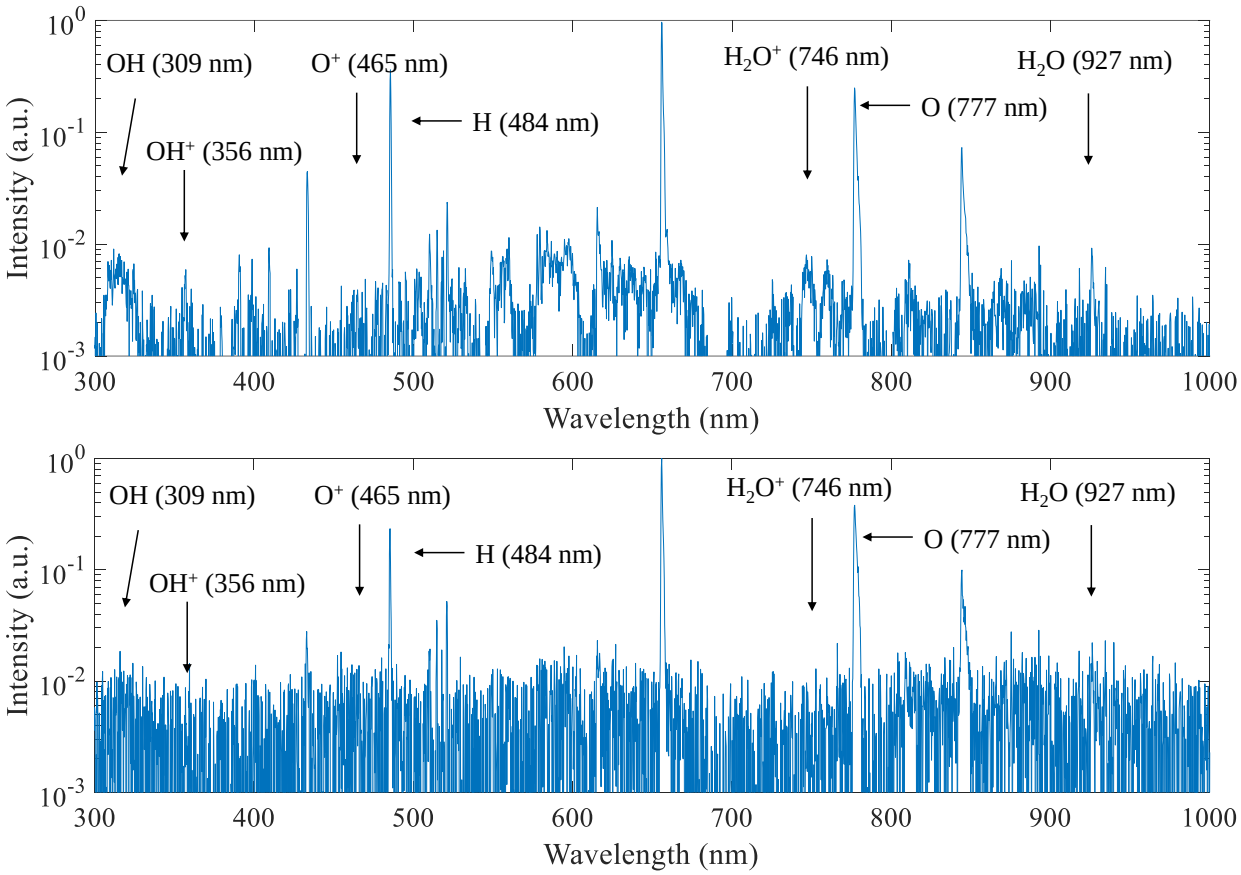

Figure 3.22: Two spectra showing the emission from water vapor in the ECR thruster. The mass flow rate is 0.224 mg/s and the input power is 60 W (top) and 174 W (bottom).

H neutrals and broader peaks corresponding to the molecular species [100]. The integration time is modulated to increase detection of the smaller peaks while avoiding saturation of the O I 777 nm line. This integration time ranged from 25 ms at high powers to 100 ms at lower powers. By presenting intensity results relative to the 777 nm line, we remove integration time as a variable.

3.5.2 Langmuir Probe

Langmuir probes measure electron number density and electron temperature. They consist of one or more electrodes immersed in a plasma as the voltage on the electrode is swept over a range of interest. We use a single Langmuir probe (LP), constructed following Lobbia and Beal [82] and shown in Fig. 3.23. One 1.0 mm diameter tungsten rod is slipped into a 3 mm diameter single-bore alumina tube telescoping inside a 6.35 mm diameter single-bore alumina tube. The probe tip is 5.0 mm long, and the voltage is swept from approximately -50 to 150 V at 1 Hz using a FG-100DDS function generator controlling a Kepco 500M Bipolar Operational Power Supply/Amplifier. We averaged four LP traces to improve signal to noise ratio. The LP data was taken at the 23.5 cm from the thruster exit plane, where the ambient magnetic field is low enough to ensure that $r_L >> r_p$, where r_L is the electron Larmor radius and r_p is the effective radius of the probe surface.

Figure 3.23: Image of the emissive (top) and Langmuir (bottom) probes used in testing.

We analyze the LP in the manner described by Lobbia and Beal [82], and a typical

current-voltage (IV) trace is shown in Fig. 3.24. In short, the ion current is subtracted from the overall signal, and a line is fit to the logarithm of the remaining signal between the floating potential and the plasma potential. The slope of this line is inversely proportional to the plasma temperature. The plasma number density is calculated from this temperature and the collection area of the probe. Classic LP theory assumes a thin sheath, with $r_p/\lambda_D > 50$, where r_p is the radius of the probe, $\lambda_D = \sqrt{\epsilon_0 k_b T_e/(q^2 n_e)}$ is the Debye length of the plasma sampled, and ϵ_0 is the permittivity of free space. In the downstream region sampled in our experiments, we find $r_p > \lambda_D \sim 3$, which prompts us to correct for orbital motion limits. This correction modifies the collection area for the current to account for the expanded sheath and is solved iteratively here to match ion number densities as described [82].

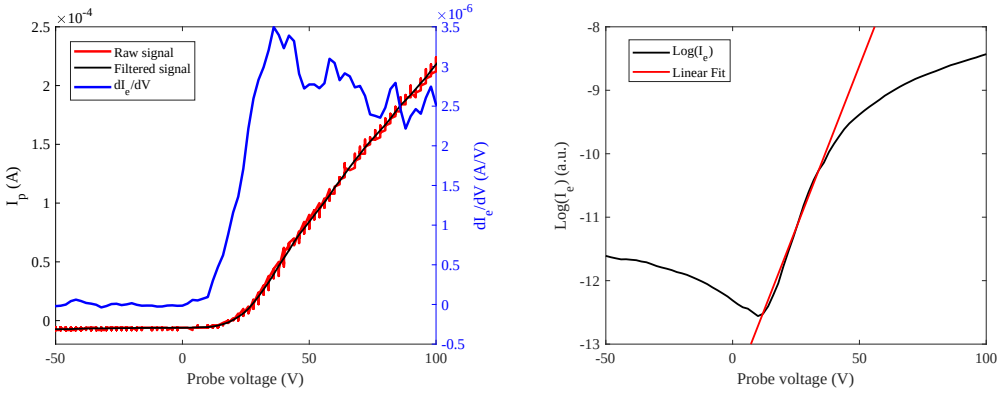

Figure 3.24: The raw and averaged signal (left) and the fitted line (right) for the Langmuir probe analysis.

3.5.3 Emissive Probe

An emissive probe was constructed [120] to determine the potential drop in the plasma at the plane of the RPA and is aligned parallel to the thruster axis. A 0.13 mm diameter, 1 cm long tungsten wire is bent into a hairpin shape and friction fit into a 2.29 mm double bore alumina tube with two copper wires. This alumina tube is telescoped into a 6.35 mm single

bore alumina tube 10 cm from the emissive probe tip. The probe is heated using a half-wave rectified AC current from a 240 V variac, and the floating voltage is measured during the non-heating half-wave. The probe is heated until the floating voltage does not change with any increase in power. An example trace is shown in Fig. 3.25

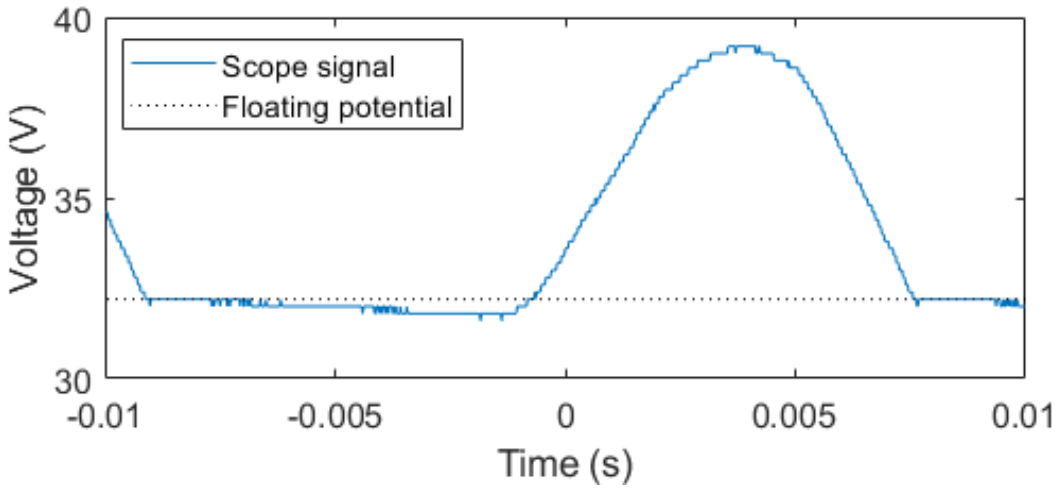

Figure 3.25: The floating voltage is determined from the half-wave rectified section of the emissive prove.

3.5.4 Faraday Probe

A swept Faraday probes was developed to assess plume divergence. The Faraday probe is mounted on a rotational stage 0.54 m away from the thruster exit plane that sweeps from -90deg to +90deg to measure the plume divergence in the far field. The probe collector is 12.5 mm in diameter and surrounded by a guard ring with outer diameter 24.0 mm and a 0.4 mm separation gap between the collector and guard ring. Both the collector and guard ring are made of 0.5 mm 99.9% molybdenum and mounted to an alumina silicate backing. The Faraday probe has an angular resolution of 1.25deg, and the small gap and guard ring ensure a flat sheath on the probe surface [16]. Both the ion collector and the guard ring are

biased to -250 V using a TDK-Lambda GEN600-1.3 power supply. A TLP7920F optically-coupled isolated amplifier conditions the floating measurement for the DAQ, and the current is measured using a 200 Ω resistor. The response and linearity of the amplified signal was checked across the expected range. The probe and an example trace is shown in Fig. 3.26.

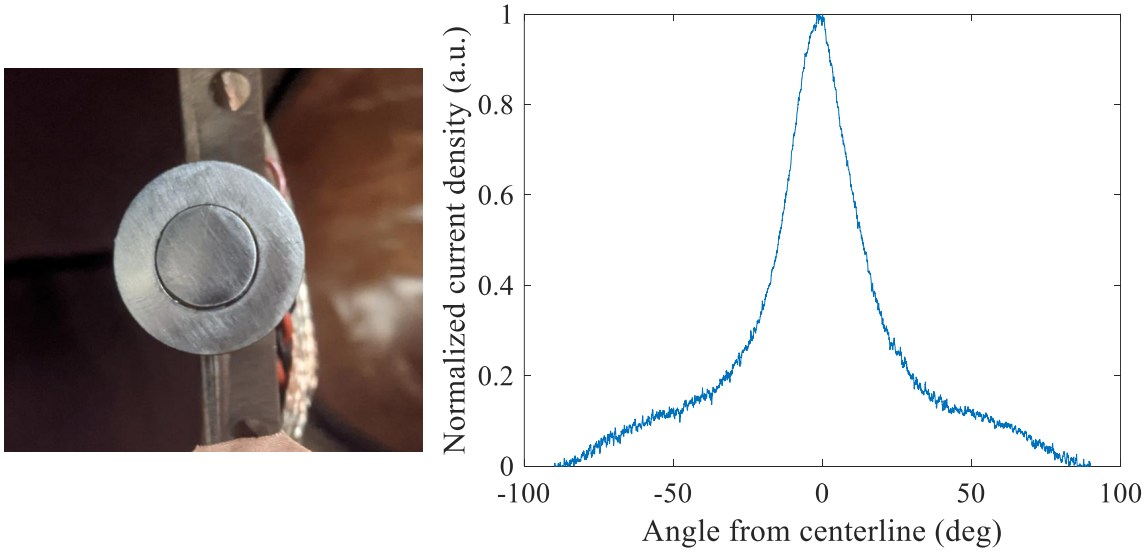

Figure 3.26: The Faraday probe used in these experiments (left) and a trace from the ECR thruster operating on 0.09 mg/s of argon at 42 W (right).

We analyze the Faraday probe following Jarrige et al [55] to determine the divergence efficiency, $\eta_D = I_{axial}/I_{beam}$, where I_{axial} is the axial ion current and I_{beam} is the total beam current. The beam current is found by integrating the current density, J_i, over the angular sweep, as

$$I_{beam} = \int_{-\pi/2}^{\pi/2} J_i \pi R_{FP}^2 \sin\theta d\theta, \tag{3.1}$$

where R_{FP} is the distance between the thruster and the probe and θ is the angle relative to the thruster axis, and the axial current is found from

$$I_{axial} = \int_{-\pi/2}^{\pi/2} J_i \pi R_{FP}^2 \sin\theta \cos\theta d\theta. \tag{3.2}$$

This calculation does not correct for the geometric error arising from assuming the thruster is a point plasma source, which is expected to be negligible since the thruster size is sufficiently small relative to the probe sweep radius [16]. From this plume divergence efficiency, we can determine the plume divergence half angle $\theta_D = \sqrt{\eta_D}$.

3.5.5 Thrust Stand

Measuring thrust for EP devices, due to their low thrust-to-weight ratio, usually requires a pendulum stand, and consideration into force balances, propellant and power connections, and chamber dimensions is paramount [104]. The measured thrust data from a thrust stand is incomparable; given propellant mass flow rate, we can calculate both specific impulse and thrust efficiency, in addition to the net thrust produced.

We built an inverted pendulum thrust stand able to measure thrusts between 100 μN and 100 mN [135], Fig. 3.27. This stand measures steady-state thrust with a response time on the order of 4 s. The stand itself is protected by a a water-cooled shroud in order to minimize sputtering and thermal effects during operation. The stand displacement is measured by a laser sensor that outputs to an oscilloscope. Testing of the SPACE Lab thrust stand show good linear response to increased force, simplifying sensor measurements to thrust values. We configured the thrust stand with 0.030" thick flexures, providing sensitivity in the thrust range of interest (100 - 1,000 μN), with a calibration of 674 mV/mN. In order to preserve stand sensitivity, we took care in connecting propellant, thermocouple, and power lines to the thruster. Surethane propellant lines were fed from the top of STF vertically down the arm used to support the thruster, and calibration tests were conducted and compared to baseline tests. There was no difference in period, frequency, or magnitude of the deflection.

Providing microwave power to the thrust stand without changing its response characteristics was more of a challenge. RF cable is inherently stiff and lossy – with high transmitted

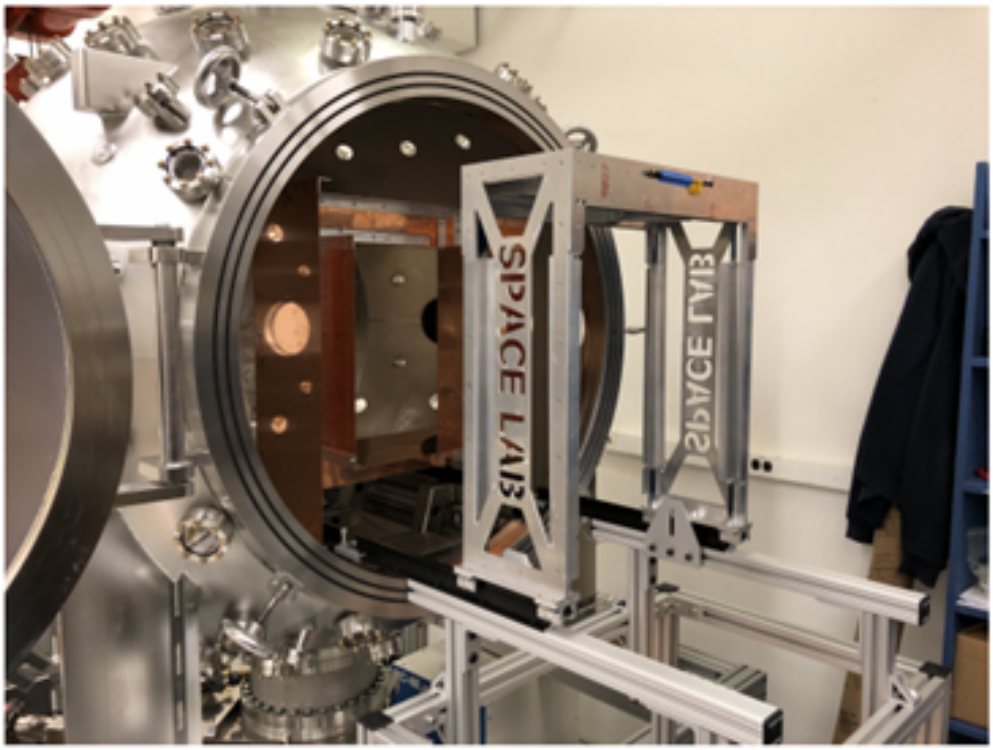

Figure 3.27: The SPACE Lab inverted pendulum thrust stand, with water-cooled copper shroud, installed in STF. The rails allow the thrust stand to be easily slid in and out of the chamber for reconfiguration.

power, the cables are likely to heat up and flex, displacing the thrust stand and confusing the thrust produced. To avoid that obfuscating measurements, we incorporate waveguide transmission of the input microwave power. We use two RF Lambda RFWA340B9CFAL waveguides to couple the microwave power from the chamber to the thrust stand. This allows the thruster to float and mitigates changes in thrust stand response due to cable stiffness or thermal expansion. One waveguide was mounted on the stationary water cooling shroud and connected via vacuum feedthrough to the power supply. The other waveguide is mounted to the top of the thrust stand, moves with the stand, and supplies power to the thruster via SPP-375LL coax. Fig. 3.28 shows the power connections from the vacuum RF

feedthrough to the thruster. The receiving waveguide is electrically isolated from the thrust stand, to ensure the thruster voltage can float. The electrical isolation of the waveguides also acts as a DC break, preventing thruster voltage from propagating upstream and damaging the microwave power supply.

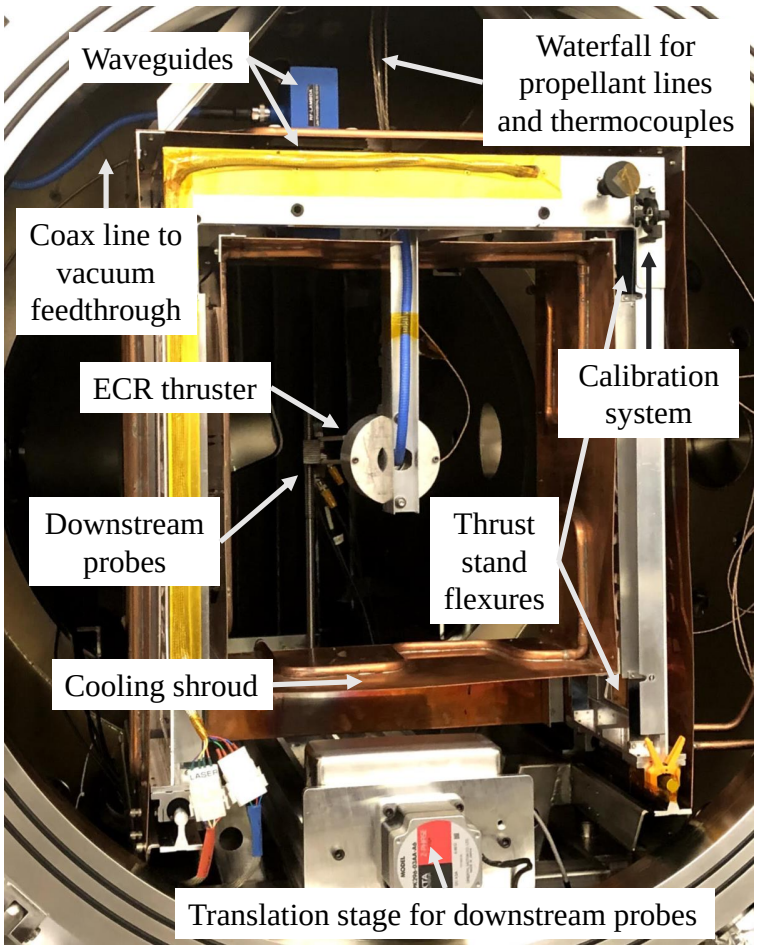

Figure 3.28: Microwave power connections to the SPACE Lab thrust stand.

Transmitting and receiving waveguides are separated from one another by a 1.7 mm vertical gap and up to a 2 mm horizontal displacement during operation. The power loss incurred by the vertical displacement was measured and determined to be less than 1%; a plot of transmitted power vs horizontal displacement is shown in Fig. 3.29. The power

transmitted is $> 99\%$ of the 0 mm displacement for up to 2 mm displacement, and there is only a 3% power loss up to 4 mm. This agrees with previous results for thrust stands transmitting 2.45 GHz power, albeit on a torsional stand [128]. The maximum displacement of the stand during testing was < 1 mm, and we conclude that the power loss due to waveguide alignment is negligible compared to the insertion losses characterized by the rest of the system, and we ignore it in the rest of this work. The net power transmission from the DDC to the thruster is measured to be 85.9%, and all powers recorded in this work are corrected for these losses.

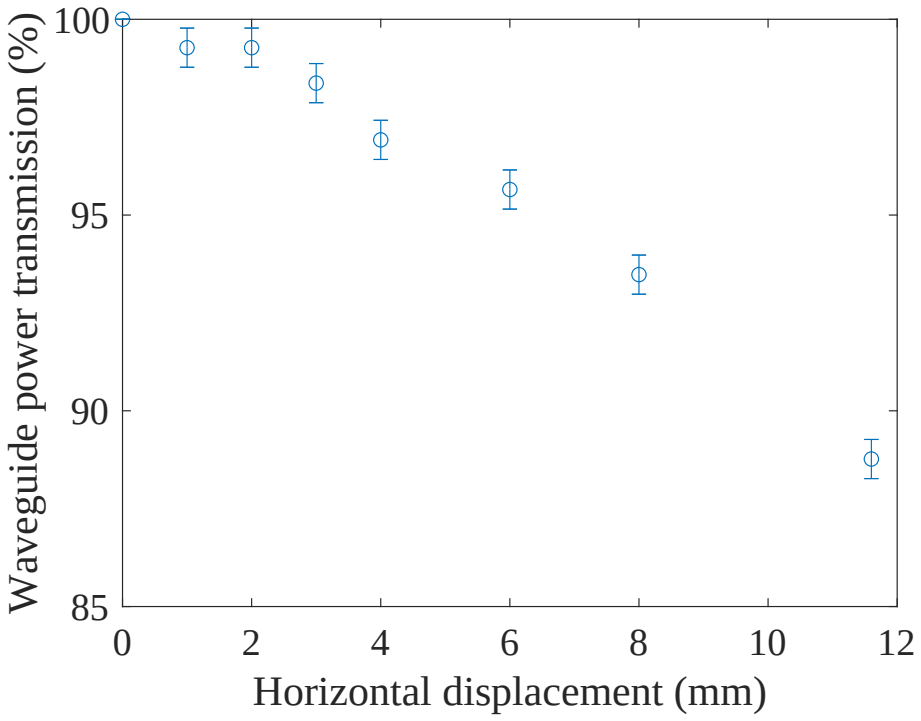

Figure 3.29: Waveguide power transmission relative to perfect alignment as a function of horizontal displacement. The maximum displacement during testing is < 1 mm.

The thrust stand does experience thermal drift, but the timescale is sufficiently long to not hinder measurements. An example trace is shown in Fig. 3.30. All thrust stand

measurements are taken after the stand has reached steady state and the power is turned off but flow rate is still on. Therefore, the thrust measurements do not account for cold gas components. For low powers, ignition is achieved by ramping up the power and/or mass flow rates, then the conditions are relaxed to those of interest, and the chamber pressure and thrust stand deflection are allowed to come to steady state (≈10 s).

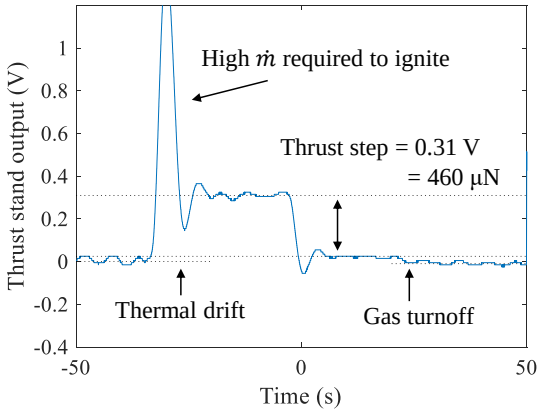

Figure 3.30: An example thrust stand trace showing the ignition and step down for 0.13 mg/s of krypton at 66 W of forward power. In this case, the thruster was lit at the test power condition but with a puff of high mass flow (6.5 mg/s) and then allowed to relax to steady state conditions.

3.5.6 ExB Probe

For determining ion species fractions, we use an ExB probe, also called a Wien filter. Incoming charged particles are deflected by crossed electric (**E**) and magnetic (**B**) fields, unless their velocity is such that the Lorentz force equation is balanced: $\mathbf{E} + \mathbf{u} \times \mathbf{B} = 0$. The ExB probe used here [42] is constructed using permanent magnets and the electric field is established by varying the voltage between two parallel plates using a Kepco 500M power supply. The probe is mounted 30 cm downstream to sample the thruster centerline. The probe collector is tungsten, and the current is read using a Keithley 680 picoammeter. The

probe has an entrance collimator with an acceptance angle of 2°, an electrode separation of 3.8 cm, and a 1,300 G magnetic field, which are comparable to commercially available ExB probes [17]. Previous research has measured ExB current in the 1 - 10 pA range for xenon (Xe^{+}, Xe^{+2}, Xe^{+3}) [64] and iodine (I_2^{+}, I^{+}, I^{+2}) [129]. These prior works have the benefit of large charge-to-mass ratio differences between the species; in this work, we need a much finer voltage resolution to differentiate the ions H_2O^{+}, OH^{+}, and O^{+}. In order to fit velocity profiles to the collected current, we must resolve differences corresponding to changes in velocity of 300 m/s or in potential of 2 V. The spread of voltages accepted at the collector plate is estimated at 1% of the voltage drop of the thruster [17], here estimated at 100 V drop or a 1 V acceptance on the collection plate. This resolution is insufficient to definitively extract velocity data for the heavier ions resulting from water vapor plasma. Experimentally, we see the full-width half-maximum of the peak is on the order of 10 V, sufficient to disambiguate the noble gas ion species but insufficient to definitively extract species data for the various ions resulting from water vapor plasma. Therefore, the ExB probe data is not assessed for the water vapor plasma in this work.

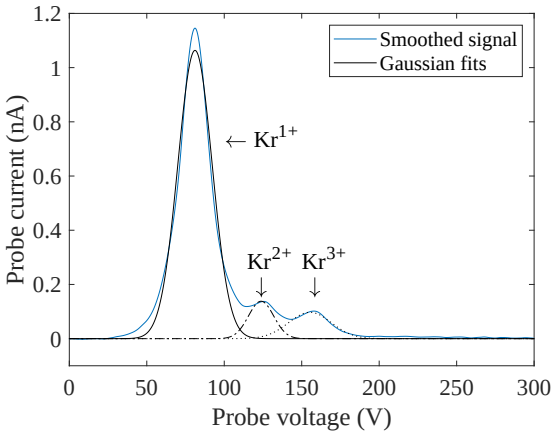

Figure 3.31: Example ExB trace with the Gaussian fits on the current peaks. This trace is for the ECR thruster operating on 0.12 mg/s of krypton at 44 W.

Determining the current fraction requires calculating separate ion currents for each ion species. Several methods have been implemented: Hofer simply measured the peak heights and ignored peak width [45]; Beal used triangles to fit the peak and full-width half maximum [9]; Linnell fit a succession of Gaussians [75]; and Kim derived a variable exponential fit [63]. A comparison of these methods, along with a charge exchange correction for background neutral collisions for xenon [119], showed only moderate disagreement among these four methods without the correction; including the correction did improve the fits for all cases tested, but determining an appropriate model for this charge exchange for the different gases tested is beyond the scope of this research. We use the results from Shastry et al [119] to estimate the error of the analyzed current as 10% and use the Gaussian fitting method [75] for all ExB probe traces, and the applied analysis is shown in Fig. 3.31.

3.5.7 Retarding Potential Analyzer

We use a four grid retarding potential analyzer (RPA) to measure the ion energy distribution function (IEDF) 30 cm downstream of the exit plane. The first grid is floating to minimize perturbation to the plasma plume. The second grid is biased to -30 V to repel electrons. The third grid is swept from 0 to 250 V to filter ions. The fourth grid is biased to -30 V to suppress secondary electron emission effects. A typical trace is shown in Fig. 3.32. The RPA is aligned with the axis of the thruster. The raw signal is smoothed using a butterworth filter and differentiated to determine the IEDF. A Gaussian is fit to the forward voltage sweep data to determine the peak of the IEDF and full-width half maximum of the distribution.

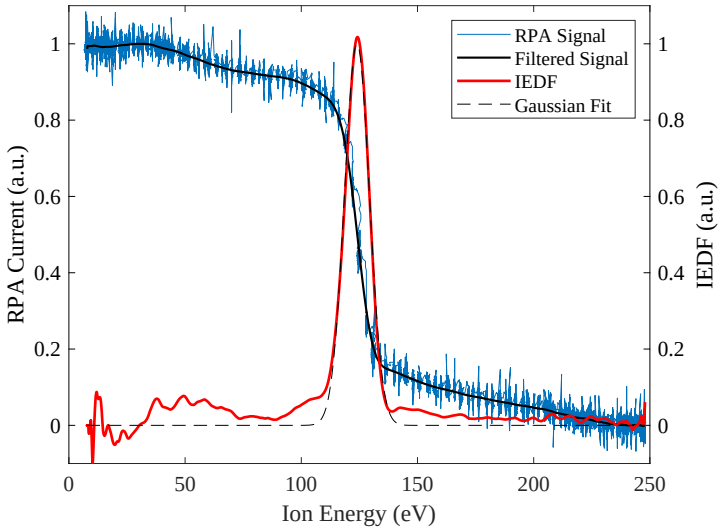

Figure 3.32: An example trace of the RPA for 0.28 mg/s of krypton at 130 W power.

Chapter 4

PERFORMANCE ANALYSIS ON ARGON, KRYPTON, XENON, AND WATER VAPOR

This chapter examines how propellant properties influence the mass utilization and frozen flow losses in an ECR thruster. The chapter begins by discussing the performance theory used to assess the thruster performance. Then, we describe the vacuum facility, the thruster, and the performance and plasma diagnostics. We present experimental results for thruster operation on argon, krypton, xenon, and water vapor. Using the resulting data, our analysis focuses on identifying how differences among the tested propellants impact the performance of the thruster. The paper ends with a discussion on relative importance of loss mechanisms observed in the thruster and suggestions for future work.

4.1 Thruster Performance Theory

Throughout our analysis, we use thruster performance measurements to derive important quantities that we cannot directly measure and provide deeper understanding into the mechanisms driving performance. We present the equations used to analyze thruster performance from the measured experimental quantities here. From the measured thrust T, we can calculate the specific impulse (I_{sp}) as

$$I_{sp} = \frac{T}{\dot{m} g_0}, \tag{4.1}$$

where $\dot{m}$ is the total mass flow rate and g_0 is the acceleration of gravity. Analytically, thrust is given by

$$T = \sum_j \dot{m}_j \langle u_j \rangle, \tag{4.2}$$

where $\dot{m}_j$ is the mass flow rate of ion species j and $\langle u_j \rangle$ is the average ion velocity, which can be written as

$$\langle u_j \rangle = \sqrt{\frac{2Z_j q V_B}{m_j}} \cos\theta_{div}, \tag{4.3}$$

where Z_j is the charge of j, q is the electron charge, V_B is the beam potential, m_j is the mass of j, and θ_{div} is the divergence half angle. If we define the total ion mass flow rate as $\dot{m}_i = \sum_j \dot{m}_j$, we can rewrite I_{sp} as

$$I_{sp} = \frac{1}{g_0} \frac{\dot{m}_i}{\dot{m}} \sqrt{2qV_B} \cos\theta_{div} \sum \frac{\dot{m}_j}{\dot{m}_i} \sqrt{\frac{Z_j}{m_j}}, \tag{4.4}$$

with mass utilization efficiency $\eta_m = \dot{m}_i/\dot{m}$. Mass utilization efficiency can then be determined experimentally using

$$\eta_m = \frac{1}{\alpha \cos\theta_{div}} \frac{g_0 I_{sp}}{\sqrt{2qV_B/M}}, \tag{4.5}$$

where we define α as a parameter correlated to the relative fraction of multiply charged ion species given by

$$\alpha = \sum_j \frac{\dot{m}_j}{\dot{m}_i} \sqrt{\frac{MZ_j}{m_j}}, \tag{4.6}$$

and M is the mass of the neutral species entering the thruster.

Likewise, from thrust and power, we calculate the thrust efficiency, η_T, as

$$\eta_T = \frac{T^2}{2\dot{m}P}, \tag{4.7}$$

where P is the power at the thruster from the supply. Thruster efficiency can also be represented as the product of all the component efficiencies

$$\eta_T = \eta_m \eta_d \eta_{ff} \eta_c \eta_b, \tag{4.8}$$

where $\eta_d = \cos^2\theta_{div}$ is the divergence efficiency, $\eta_{ff} = P_{KE}/P_{ex}$ is the frozen flow efficiency, η_c is the coupling efficiency, $\eta_b = P_{ex}/P_{in}$ is beam efficiency, P_{KE} is the ion kinetic power, $P_{ex} = P_{rad} + P_{ion} + P_{KE}$ is the power exhausted from the thruster, P_{rad} is the radiated power, P_{ion} is the power required to ionize the propellant, $P_{in} = P_{ex} + P_w$ is the power deposited into the plasma, and P_w is the power lost to the walls.

To determine the frozen flow efficiency, we consider the frozen flow power losses, described by

$$P_{rad} + P_{ion} = \sum_j \frac{\dot{m}_j}{m_j} \epsilon_j^*(T_e^*), \tag{4.9}$$

where ϵ_j^* is the effective ionization energy including excitation losses as a function of T_e^*, the electron temperature in the source. We find an effective ionization energy for the first ionization state following the method of Little [80], based on the numerical results of Dugan and Sovie [37], and assume an effective second and third ionization energy as twice the ionization energy of that state. For water vapor, we use the average ion cost from a non-equilibrium plasma chemistry model [121] to determine this effective ionization energy.

We did not measure T_e^* directly, as any physical probe would disrupt operation of the thruster, and we did not have the capability to measure indirectly (e.g., with optical or laser diagnostics). Instead, we infer T_e^* assuming a polytropic expansion of the plume from the microwave nozzle throat [91],

$$k_B T_e^* = \frac{\gamma_e - 1}{\gamma_e} q V_B, \tag{4.10}$$

where k_B is the Boltzmann constant, and γ_e is the electron polytropic index, generally found to be between 1.15 and 1.37 experimentally [31, 77]. We use the value 1.2 here. Eq. 4.10 is derived from a model that assumes a collisionless plasma past the magnetic nozzle throat and Maxwellian electrons at T_e^* at the throat [91]. Various studies have experimentally assessed this polytropic expansion, with varying levels of confidence in its goodness of fit. While the polytropic expansion fits tend to agree within the measurement error of the diagnostics [77,

131], there is also evidence that more complex fits may better explain the plasma expansion further downstream [28] or considering time-resolved measurements [62]. We use Eq. 4.10, as those caveats are mitigated here: first, we measure the ion energy sufficiently close to the source such that the polytropic expansion is still a good fit; and second, we are interested in the time-averaged effect of temperature.

With these definitions, we can calculate the frozen flow efficiency using

$$\eta_{ff} = \frac{\alpha \dot{m}_i q V_B}{\alpha \dot{m}_i q V_B + M \sum_j \frac{\dot{m}_j}{m_j} \epsilon_j^*}. \tag{4.11}$$

With the assumption of singly charged ion species, the frozen flow efficiency scales with the beam voltage over the effective ion energy. The presence of higher charge states ($\dot{m}_j$ for j = 2,3) leads to a reduction in η_{ff}, since the denominator increases faster than the numerator. α scales with $\sqrt{Z_j}$, while the second term in the denominator scales directly with the effective ionization cost for those higher ionization states.

With respect to the remaining terms in Eq. 4.8, we define a source efficiency, $\eta_s = \eta_c \eta_b$, where η_c is the coupling efficiency and η_b is the beam efficiency. This source efficiency represented the total power exhausted from the thruster over the total input power. Here, coupling efficiency is the fraction of power delivered to the plasma over the total power delivered to the thruster. Beam efficiency is the fraction of kinetic power exhausted from the thruster over the power deposited into the plasma. With the data from the experiment, we determine source efficiency as

$$\eta_s = \frac{\eta_T}{\eta_m \eta_d \eta_{ff}}. \tag{4.12}$$

The source efficiency captures the effects of losses that are difficult to measure experimentally. While a dual directional coupler or other device can measure the power delivered to the thruster, experiments have yet to discern the amount of power that is deposited into the plasma from the power radiated by the thruster. Likewise, beam efficiency relies on understanding this coupling efficiency and spatially resolving the ion kinetic energy and has

not been measured experimentally. Numerically, Sánchez-Villar et al calculated a coupling efficiency of 25.3% and a beam efficiency of 32.2% for a coaxial ECR thruster operating on xenon [111].

4.2 Plasma Diagnostics

Here, we describe the specific equations and assumptions necessary to utilize our diagnostics described in Ch. 3 to determine the performance detailed above.

4.2.1 Langmuir Probe

We must verify that the assumptions made in the Langmuir Probe (LP) analysis are well met by the sampled plasma. First, we consider the influence of magnetic fields. In the plane of measurement, the ambient magnetic field ($\approx$ 50 G) is low enough to ensure that $r_L >> r_p$, where r_L is the electron Larmor radius and r_p is the effective radius of the probe surface for all species considered here. Next, we consider quasineutrality. Water is electronegative below $\approx$ 4 eV [102], which requires analysis to account for negative ions reaching the probe [15]. However, in the work presented here, all probe traces collected using water vapor are well above that temperature, and the complicating effects are ignored.

4.2.2 Retarding Potential Analyzer

For simplicity, we assume that the ion energy is solely kinetic and that the ions are singly charged. This allows us to determine the ion velocity (u_i) using

$$u_i = \sqrt{\frac{2q(V_{peak} - V_{plasma})}{m_i}}, \tag{4.13}$$

where V_{peak} is the voltage corresponding to the peak of the ion energy, V_{plasma} is the plasma potential measured by the emissive probe described later, $V_{peak} - V_{plasma} = V_B$ as defined earlier, and m_i is the ion mass.

4.2.3 ExB Probe

If we assume all ions are accelerated by the same voltage drop in the thruster, the ion velocities are proportional to the square root of the charge state, and the ExB probe can distinguish between ion species. The total ion current to the probe (I_i) can be written as

$$I_i = qZ_i n_i u_i A_c = qZ_i n_i \sqrt{\frac{2qZ_i V_B}{m_i}} A_c, \tag{4.14}$$

where Z_i is the ion charge state, n_i is the ion number density, and A_c is the collector area. We can determine the ion mass flow rate from the ion current following Huang and Shastry [47] using

$$\dot{m}_j = \frac{I_j m_j}{Z_j q} = A_c \frac{K_2^2 m_j}{K_1} \int_0^\infty \frac{I_{p,j}(V_p)}{V_p^2} dV_p, \tag{4.15}$$

where I_j is the current of ion species j, K_1 and K_2 are geometric constants related to the construction of the ExB probe, V_p is the probe voltage, and $I_{p,j}(V_p)$ is the probe current as a function of V_p for the jth species. Since A_c, K_1, and K_2 are constants for the probe, we can rewrite Eq. 4.6 as

$$\alpha = \sum_j \frac{\int_0^\infty I_{p,j}/V_p^2 dV_p}{I_j} \sqrt{\frac{MZ_j}{m_j}}. \tag{4.16}$$

This equation for α requires distinct ion currents for each ion species from the probe signal. We use the results from Shastry et al [119] to estimate the error of the analyzed current as 10% and use the Gaussian fitting method [75] for all ExB probe traces, as discussed in Ch. 3.

4.3 Experimental Results

Mass, ionization energy, and ionization cross section all change with propellant. Mass influences neutral and ion velocity, which would suggest variation in transit time in a thruster of a constant length. Ionization energy determines the fraction of the electron population with sufficient energy to ionize the propellant particles, which impacts both plasma density and

mass utilization efficiency. Propellants with a larger ionization cross-section would also likely have increased mass utilization and plasma density, resulting in higher thrust and efficiency. To explore these characteristics, we tested the ECR thruster on argon, krypton, xenon, and water vapor. The propellants chosen span almost an order of magnitude in mass, about thirty percent in ionization energy, and a factor of around four in ionization cross section at the temperatures of interest. This range is to evaluate the key drivers in performance variation.

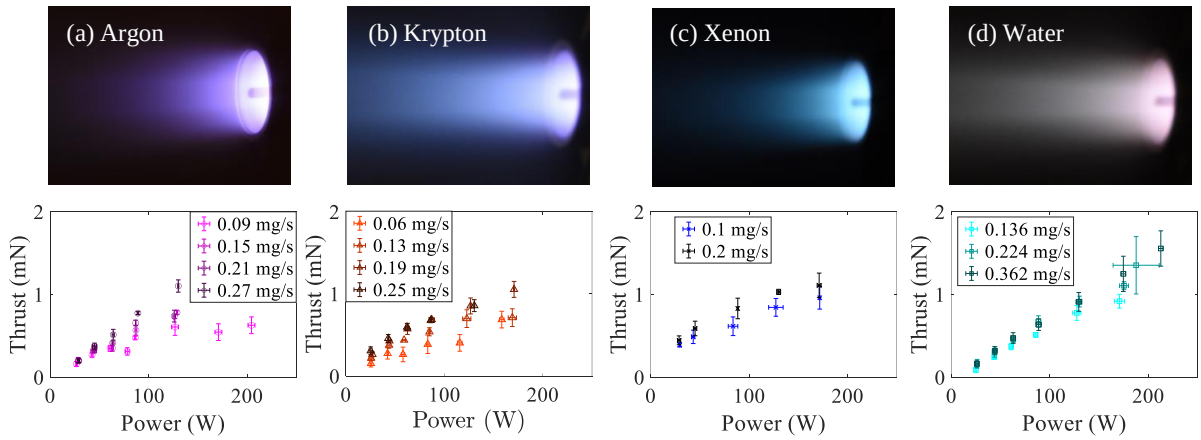

Figure 4.1: Photos of operation (top) and measured thrust (bottom) from operation on (a) argon, (b) krypton, (c) xenon, and (d) water vapor. The error bars represent one standard deviation of the measurement.

The top row of Fig. 4.1 shows images of the thruster firing on the different propellants. The thruster plume in all cases is highly collimated, and we notice a bright region near the central antenna. This localized brightness qualitatively agrees with the numerical work of Sánchez-Villar et al [111] showing areas of high current density near the antenna.

The measured thrust increases with power for all flow rates and all propellants, as shown in Fig. 4.1. At the lowest flow rates for both krypton and argon, the thrust seems to roll over as power increases, suggesting a limitation on acceleration gain vs loss mechanisms. Increasing mass flow rate is correlated with a higher thrust at all power levels, but the gain

for mass flow rate is not constant, particularly for water. We see a factor of about 2 reduction in thruster performance on xenon and krypton compared with literature [139, 138, 107] at similar conditions. The thruster tested here is approximately 8 mm longer than that reported earlier, which may indicate that this discrepancy in performance is due to losses associated with longer residence times, namely secondary ionization reactions and collisions with the walls. These thrust stand results, however, are comparable to or slightly higher than those reported by Moloney et al [92], which is also shorter than the thruster tested here.

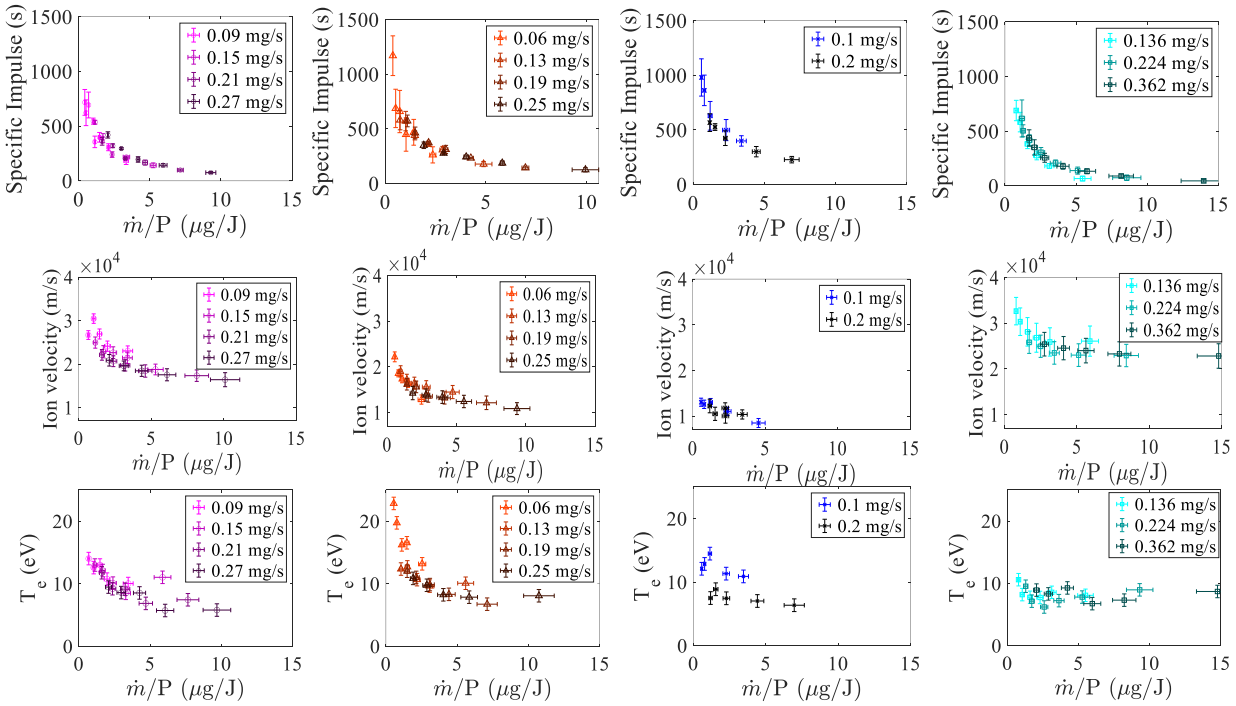

Figure 4.2: Performance characteristics of the ECR thruster operating on (a) argon, (b) krypton, (c) xenon, and (d) water vapor. From top to bottom, the rows show the specific impulse, ion velocity, and electron temperature in the plume.

To balance the competing effects of increasing power and mass flow rate on thruster performance, we consider the rest of the thruster performance and plasma characteristics as functions of the ratio $\dot{m}/P$. This is in accordance with previous ECR research [55] and is

helpful in considering the energy balance, as this metric describes the inverse of energy per particle. While this normalization does reduce some of the variability, we still find mass flow rate to influence performance in some parameters for some propellants.

Fig. 4.2 presents the data from the diagnostics: specific impulse from the thrust stand, ion velocity from the RPA, and electron temperature from the Langmuir probe. For all four species considered here, decreasing $\dot{m}/P$ is correlated with increased I_{sp} with an approximate scaling of $I_{sp} \sim (\dot{m}/P)^{-1}$ dependence. This agrees with the linear relationship observed between power and thrust shown in Fig. 4.1 but does contrast with the linear fit between $\dot{m}/P$ and I_{sp} found by Vialis et al [138] on xenon. The observed non-linear relationship in I_{sp} suggests that the plume is not fully ionized until a critical value of $\dot{m}/P$, at which point excess power goes into heating the electrons and accelerating the ions in the ambipolar field in the thruster. The second row of Fig. 4.2 shows that the ion velocity in the beam is quite high and relatively flat above a threshold value of $\dot{m}/P$ for most species. At lower $\dot{m}/P$, the ion velocity increases sharply for argon, krypton, and water vapor, indicating that the increased power goes into accelerating ions. The ion velocities described by the RPA match well with laser induced fluorescence results for xenon (≈ 11 km/s for 0.1 mg/s Xe at 30 W) reported by Wachs and Jorns [141]. Comparing the RPA ion velocity to the effective ion velocity from the specific impulse, the lower values of the specific impulse suggest that mass utilization efficiency is low.

The electron temperatures are shown in the third row of Fig. 4.2. For argon and krypton, the electron temperature increases strongly as $\dot{m}/P$ decreases, while the effect is more moderate for xenon. The electron temperature in the water vapor plasma appears to have a slight dip in temperature at moderate $\dot{m}/P$. These trends in electron temperature are similar to the trends in ion velocity, which is consistent with ambipolar acceleration in a magnetic nozzle. The LP measured plasma densities on the order of 1×10^{14} m^{-3}, consistent with the sampling in the far field region of the thruster.

Fig. 4.3 shows the charge state current fraction for the noble gases. The ExB probe was not able to sufficiently resolve the velocity spread of the ion species in the water vapor

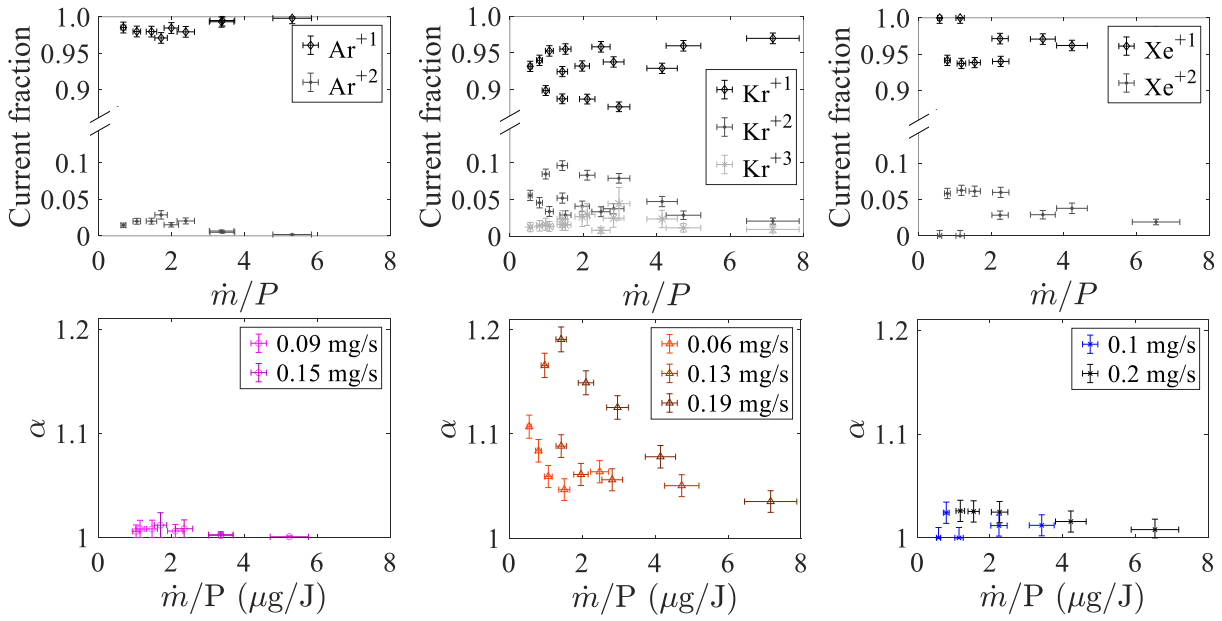

Figure 4.3: The influence of charge states of the ECR thruster operating on (a) argon, (b) krypton, and (c) xenon. The top row shows the charge state current fractions from the ExB probe and the bottom row shows α, from Eq. 4.6, all as functions of mass flow rate divided by power.

plume, due to the small difference in charge to mass ratio of the ion species. We see that, for all noble gases, the plume is comprised almost entirely of singly charged ion species. For argon and xenon, particularly, we see that there is no evidence of triply charged ions and the doubly charged ion fraction is no greater than 8% of the total current to the probe. Krypton has both a higher fraction of doubly charged ions and an observable population of triply charged ions in the plume. This is unexpected, as the krypton does not have significantly higher electron temperatures in the plume and its first, second, and third ionization energies are moderate and bounded by the corresponding ionization energies for argon and xenon. The lack of triply charged xenon ions is contrary to results for ExB probe traces in Hall thrusters, which shows that conditions producing triply charged krypton ions also produce triply charged xenon ions with a higher current than krypton [75].

The second row of Fig. 4.3 shows the impact of these charge states on the parameter α, as defined in Eq. 4.6, which represents the influence of the current arising from higher charge species as a single parameter. Higher α increases specific impulse at the cost of decreased mass utilization and frozen flow efficiency. We see that α decreases with increasing $\dot{m}/P$ for krypton, while it is largely constant for xenon and argon. Additionally, α is much larger for krypton than for the other species, due to the increased presence of secondly and triply charged ions in the plume. Interestingly, we do not necessarily see the negative effects of increased α on the mass utilization efficiency, shown in Fig. 4.4. This indicates that other factors dominate the losses in η_m.

Fig. 4.4 shows the efficiencies derived from the thruster performance measurements. The thrust efficiency, shown in the first row, increases slightly for a given $\dot{m}/P$ as mass flow rate increases and increases as $\dot{m}/P$ decreases for all species except xenon. Thrust efficiency for xenon is approximately flat across $\dot{m}/P$ and higher for the lower mass flow rate tested. In contrast to the work of Vialis et al [138], the $\dot{m}/P$ normalization does not collapse the thrust efficiency well onto one curve.

We calculate the mass utilization efficiency from our probe data following Eq. 4.5. We measured a divergence efficiency of 73%±2% with the Faraday probe. The divergence efficiency shows no variation in divergence with mass flow rate, power, or propellant type tested, in agreement with the literature [20, 138, 28]. Mass utilization efficiency is shown in the second row of Fig. 4.4. It is observed that the mass utilization efficiency increases with decreasing $\dot{m}/P$ for all species. This correlates with the higher electron densities measured by the Langmuir probe. Comparing the noble gases, argon has the highest ionization energy and lowest atomic mass and xenon has the lowest ionization energy and highest atomic mass. Xenon neutral particles have a slower thermal velocity at ambient temperature due to their higher mass and, therefore, a longer residence time in the thruster channel, which increases likelihood of ionization. This compounded with the lower ionization energy increasing the fraction of electrons with sufficient energy to ionize a neutral explains the difference in magnitude of mass utilization efficiency decreasing from xenon to krypton to argon. The electron

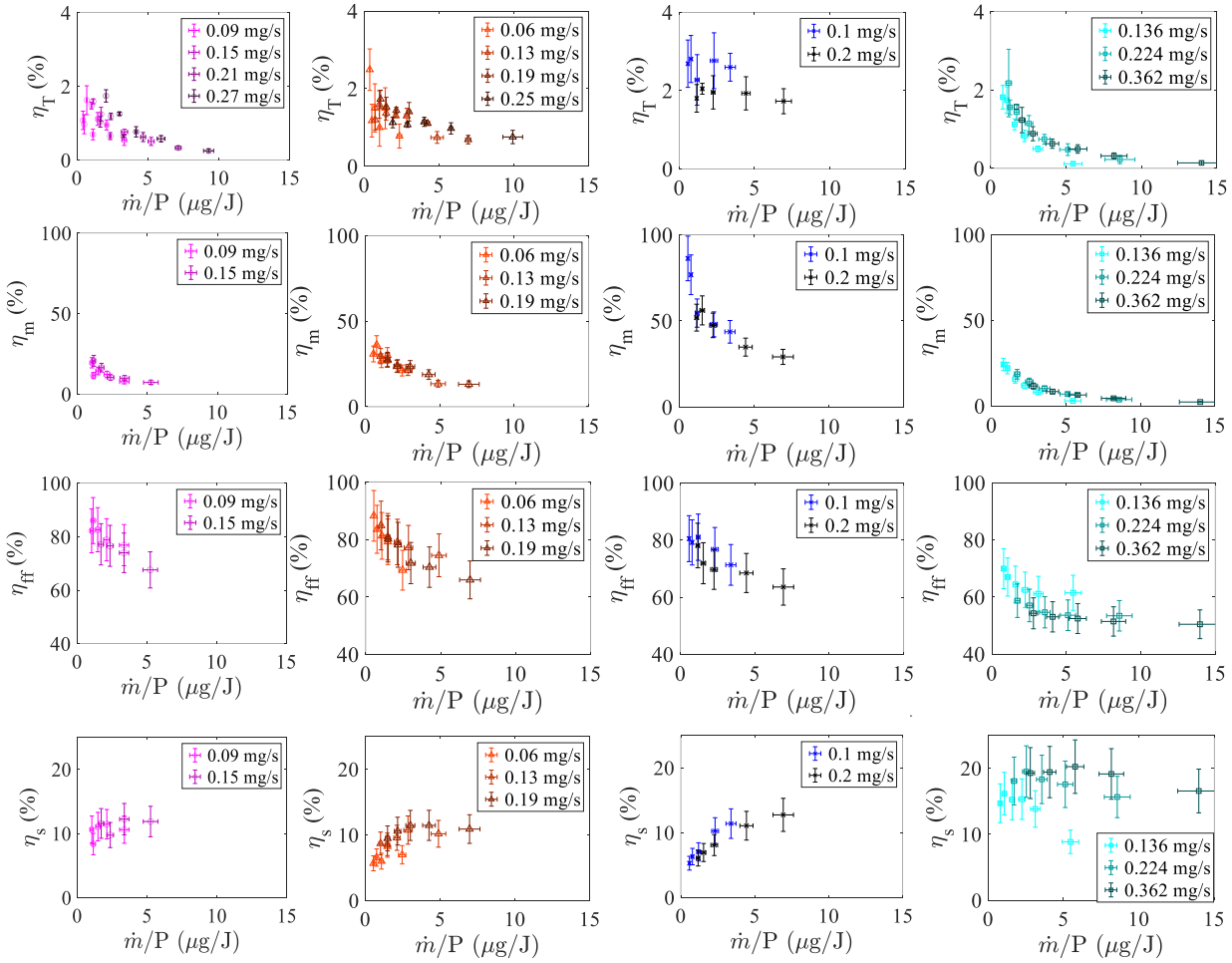

Figure 4.4: From top to bottom, the rows show thrust efficiency, mass utilization efficiency, frozen flow efficiency, and source efficiency for the ECR thruster operating on (a) argon, (b) krypton, (c) xenon, and (d) water vapor.

temperature in the source, T_e^*, is also a key factor in increasing mass utilization efficiency. As T_e^* increases, so does ionization rate, for the moderate electron temperatures considered here. This effect explains most of the increase in η_m for $\dot{m}/P < 5$ μg/J. Water vapor has a lower atomic mass than other species tested here but an ionization energy comparable to xenon. The trend shown in Fig. 4.4 demonstrates the relative importance of these two effects. At high $\dot{m}/P$, the neutrals exhaust before they can be ionized, while at low $\dot{m}/P$,

the electrons have sufficient energy and density to ionize the plume.

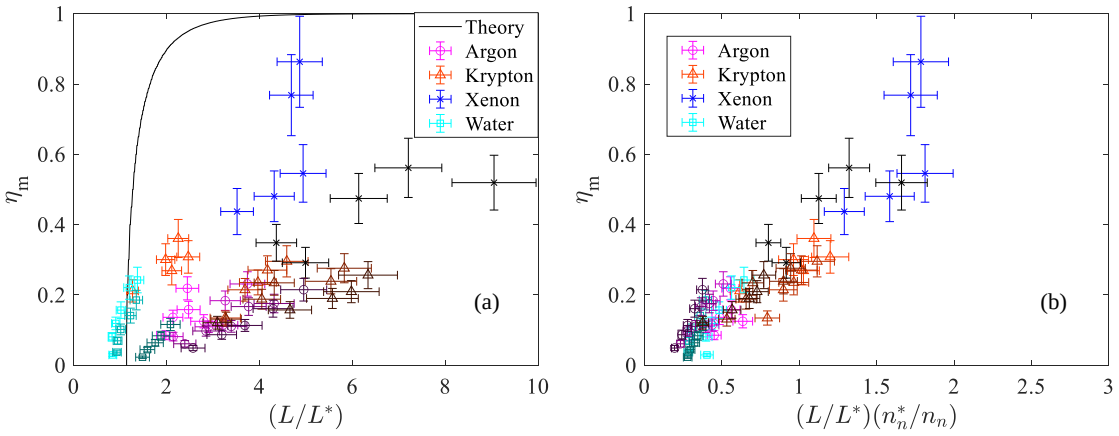

Figure 4.5: (a) The experimental data compared to theoretical scaling [3] of η_m with (L/L^*) and (b) the experimental η_m scaled with $(L/L^*)(n_n^*/n_n)$. The mass flow rates of the various species correspond to the caption in Fig. 4.4.

To gain deeper insight into the influence of propellant properties on mass utilization, we compare our experimental measurements to a theoretical scaling law proposed by Ahedo and Navarro-Cavallé [3]. Ahedo and Navarro-Cavallé derive an analytic scaling for mass utilization efficiency as an implicit function of the ratio of L/L^*, the transit length L over the ionization length scale $L^* = c_s/(n_n R_{ion})$, where c_s is the ion sound speed, n_n is the neutral density, and R_{ion} is the ionization reaction rate. This scaling was specifically derived for a helicon source but should be applicable to the tested ECR thruster due to the similarity in geometry and magnetic field structure. Fruchtman also finds the ratio L/L^* to be important in the scaling of mass utilization efficiency [39]. We present Ahedo and Navarro-Cavallé's scaling in Fig. 4.5(a) along with the experimental data for the propellants tested here. Here, in calculating L/L^*, we have assumed Maxwellian electrons at T_e^* and used the first ionization cross section for noble gases [146] and the total ionization and dissociation cross sections for water vapor [121]. It is clear from the figure that the experimental data does not follow

the theoretical scaling. Instead, the data suggests that a more complex scaling exists that depends on both the mass flow rate and propellant particle mass. We find that the experimental data collapses onto a single curve [Fig. 4.5(b)] if the x-axis is scaled by n_n^*/n_n, where $n_n = \dot{m}/(m_i u_n A)$ is the neutral density in the thruster, A is the cross sectional area of the thruster, and n_n^* is a characteristic value. We choose n_n^* such that a linear extrapolation of the observed scaling yields $\eta_m \approx 1$ when $L/L^* = 3$ and $n_n = n_n^*$. This method gives the value $n_n^* \approx 3 \times 10^{18}$ m^{-3}. The model of Ahedo and Navarro-Cavallé predicts $\eta_m \approx 1$ when $L/L^* > 3$. Our results then suggest that additional mass utilization loss processes appear when $n_n > n_n^*$, which cannot be explained by an insufficient ionization rate. One possible explanation is the onset of increased wall losses, which Ahedo and Navarro-Cavallé assumed to be small in the derivation of their analytical scaling law. A second explanation may be the appearance of wave cutoffs above a certain density. We expect the plasma density scales as $n_e \sim n_n \sqrt{T_n/T_e}$, which would give a value of $n_e^* \sim 10^{17}$ m^{-3} for $T_e \sim 20$ eV and $T_n \sim 300$ K. This value is on the order of the cutoff density for 2.45 GHz waves, $n_{e,co} \approx 7.5 \times 10^{16}$ m^{-3}. This may suggest that microwave power is being shielded from the outer regions of the flow when $n_n > n_n^*$. Additional numerical and experimental examination of these effects are needed, but are beyond the scope of this work.

Frozen flow losses account for ionization, radiation, and dissociation energy that is unrecoverable in the plume. As shown in the third row of Fig. 4.4, the noble gas species have similar η_{ff} over the range of T_e and $\dot{m}/P$ considered here. This may seem counterintuitive because these species have different ionization energies and cross sections. To understand this observation in more depth, we present Fig. 4.6, which compares the beam voltage across the range of propellants. Recall that V_B is also used to obtain T_e^* according to Eq. 4.10, and therefore also the effective ionization energy, $\epsilon^* = \sum_j (\dot{m}_j/\dot{m}_i)\epsilon_j^*$. We note that decreasing $\dot{m}/P$ increases beam voltage, as expected, although that effect is not as pronounced for either xenon or water vapor. Krypton and argon have comparable effective ionization energy, V_B, and T_e^*, which is reflected in the similar η_{ff} shown here. Likewise, while xenon has a lower effective ionization energy compared to krypton or argon, its V_B is lower and it therefore

has a similar η_{ff}. For all species, as $\dot{m}/P$ decreases, η_{ff} increases, and more power is put into heating the electrons and accelerating the ions. This trend for the atomic species is due to both increased V_B and decreased ϵ^*. However, for water, we see that, while η_{ff} and V_B increase as $\dot{m}/P$ decreases independent of mass flow rate, the effective ionization energy for a fixed mass flow rate also increases, albeit slowly. This suggests that increased beam energy has a larger impact on frozen flow losses than the ionization costs. Indeed, over the range of $\dot{m}/P$ shown here, the ionization cost for a given propellant varies by 15 - 25%, while the beam voltage varies by up to 400%. Compared with the atomic species, water vapor has about 50% higher effective ionization energy, as expected for a molecular compared to atomic propellant. This effective ionization energy also has a dependence on mass flow rate not seen in the atomic species, with larger mass flow rates corresponding to higher losses.

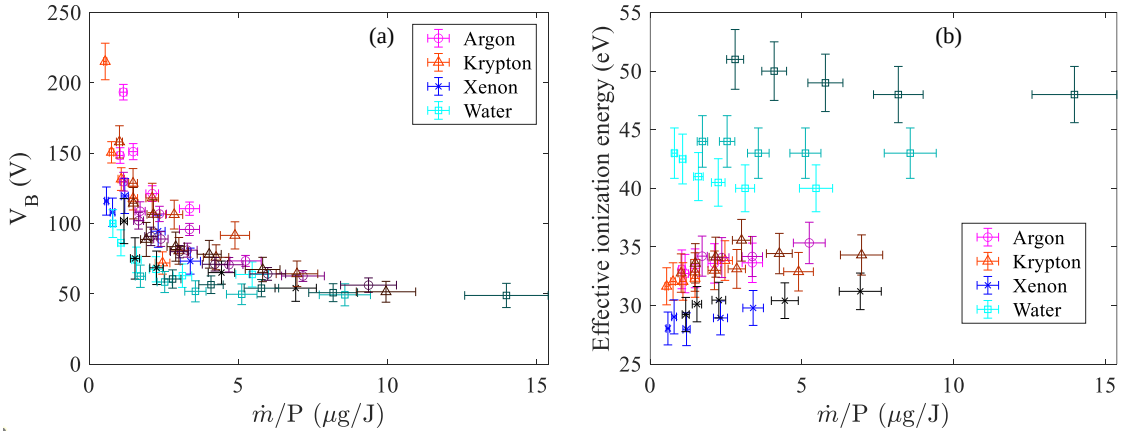

Figure 4.6: (a) The beam voltage and (b) the effective ionization cost for all propellants as function of $\dot{m}/P$. The mass flow rates of the various species correspond to the caption in Fig. 4.4.

From our analysis, the source efficiency, which embodies wall losses and coupling efficiency, is approximately constant across $\dot{m}/P$ for argon and water vapor, Fig. 4.4. Water has a higher η_s than any of the species, but its smallest mass flow rate has a lower η_s. Con-

sidering krypton and xenon, the efficiency rises for $\dot{m}/P < 5$ μg/J, then approximately levels off. For krypton, this trend is inversely proportional with the increasing electron temperatures, while for xenon, no apparent explanation arises. More research is needed to assess the roles of wall losses and coupling efficiency in these thrusters. With respect to wall losses, the thruster backwall is unshielded and near the neutral gas injection region, which combine to increase the likelihood of high wall losses. This effect is similar to that expected in helicon sources [3] and can be mitigated by modifying the magnetic field to shield the backwall. In the course of testing, we did see empirical evidence of losses from the central antenna. The plasma sputtered the exposed copper antenna onto the rear and side walls of the thruster channel, ultimately removing 0.1 mm from its diameter over the course of data collection ($\approx$ 40 hrs). Sánchez-Villar et al modeled the characteristics of a xenon plasma in an ECR thruster with good agreement to available experimental results [111]. The modeled thruster is similar in diameter but 40% shorter in length than the one presented here, and in that shorter thruster, wall losses accounted for two thirds of the energy loss. These losses are concentrated along the central antenna, where the electron temperatures are sufficiently high to overcome any magnetic shielding, and substantial along the backwall of the thruster, which qualitatively agrees with experimental results. Sánchez-Villar et al conclude that shielding on the lateral walls works well [111].

Finally, we combine Eqs. 4.1 and 4.7 to calculate the thrust-to-power ratio T/P as

$$\frac{T}{P} = \frac{2\eta_T}{g_0 I_{sp}}. \tag{4.17}$$

Fig. 4.7 presents a contour plot of η_T as a function of I_{sp} and T/P for all data discussed here. We see that operation with water vapor and argon corresponds to an approximately constant T/P spanning the range of conditions tested, whereas operation with xenon tends to follow a line of constant η_T. Krypton splits the difference, with test points falling on a line with a shallower slope than the lines of constant η_T. Comparing to the literature, at least two thrusters have operated with xenon and have performance generally spanning the range between 10 and 35 mN/kW and between 200 and 1000 s I_{sp}, with thrust efficiency between 1

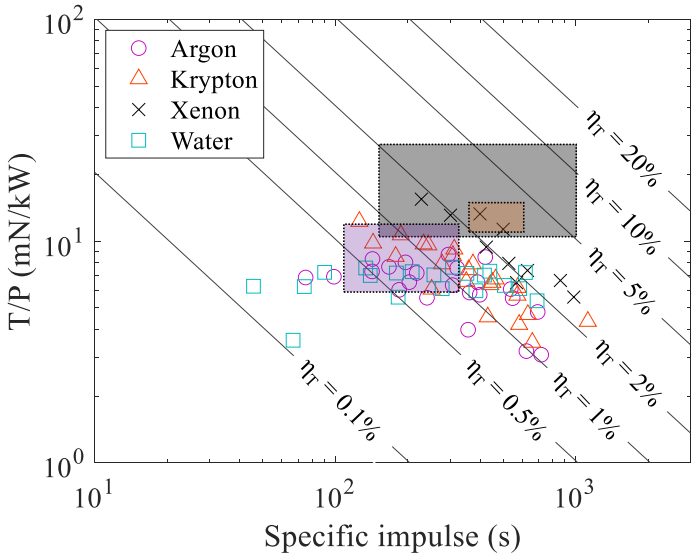

Figure 4.7: Thrust to power ratio vs specific impulse for all propellants tested in this work with lines of constant thrust efficiency. The shaded boxes represent the span of published results on argon (purple) [55, 92], krypton (orange) [139], and xenon (gray) [19, 138, 92, 107].

and 16% [19, 138, 92, 107]. Data published with argon shows lower performance: 90 - 315 s I_{sp} at a thrust-to-power ratio of 6 - 11 mN/kW and between 0.3 and 1.7% thrust efficiency [55, 92]. Vialis et al tested krypton [139] and found performance between 350 and 650 s at an approximate T/P between 11 and 16 mN/kW with a maximum thrust efficiency of 3.7%. The argon performance is comparable to that shown here, while the xenon and krypton performance is generally higher. Surprisingly, we find that even with the large frozen flow losses and poor mass utilization, we do not observe significantly worse performance with water vapor compared to xenon. We note that this thruster has not been optimized, and groups obtaining superior performance have iterated on materials and geometry to enhance performance. Our results suggest that, while xenon has been the propellant of choice in previous ECR literature, comparable performance on other propellants may be achievable

with optimization.

4.4 Conclusion

In this chapter, direct thrust measurements and ion energy diagnostics describe coaxial ECR performance on argon, krypton, xenon, and water vapor. The first results of an ExB probe on an ECR thruster show the presence of doubly charged ions for argon and xenon and triply charged ions for krypton, in contrast to results seen in Hall thruster operation comparing xenon and krypton. Higher ion exhaust velocities for the lighter species (water and argon) do not translate to higher specific impulse due to low mass utilization efficiency, and mass utilization efficiency appears to be driven more by the neutral density and residence time in the thruster than by the ionization energy of the species. Frozen flow losses do not have a large effect on thruster performance for the atomic species tested and have a moderate effect on performance for water vapor. High wall losses predominantly on the central antenna contribute to thruster erosion and poor thrust efficiency for all species.

Chapter 5
WATER PROPELLANT CHEMISTRY

In Chapter 2, our control volume model indicated that plasma composition is a function of electron temperature and p_0L. For EP applications, we are interested in regions that show high concentrations of molecular ions compared with neutrals and atomic ions, which corresponds to a p_0L between 0.03 and 0.3 mTorr·m for $T_e > 15$ eV, as shown in Fig. 2.2. Dissociation reactions are more common in lower temperature plasmas, while dissociative recombination reactions are more likely at high p_0L. By modifying experimental parameters, we can target these different regimes.

This chapter presents a unification of theory and experiment to describe the physics driving performance in a water thruster. We describe in more detail results from the thruster experiment described in Ch. 4, which motivate modifying the model presented in Ch. 2 and including loss mechanisms to better represent the experimental ECR thruster described in Ch. 3. We comment on the agreement between theory and experiment and conclude with suggestions for future experiments to improve thruster performance and clarify lingering physics questions.

5.0.1 Optical Emission Spectroscopy

We compare line intensities relative to the O I line, and two spectra can be seen in Fig. 3.22. While actinometry usually uses a trace gas to determine absolute concentration of a process gas [10, 48, 123], we use the line ratios to indicate the relative concentration of the species in the thruster plume [38]. If we assume coronal equilibrium, two processes are important: electron impact collisions that excite species and spontaneous emission that de-excite species [38]. A coronal equilibrium model is not as accurate as models that incorporate the influence

of metastable species that have been shown to have a significant impact in xenon excitation intensity in Hall thrusters [12], e.g., a collisional radiative model [57]. Our plasma conditions do not strictly meet those for coronal equilibrium, as the ionization fraction is high, but the electron temperature and number density are within the range usually expected for applicability. However, the coronal model, while simplified, is sufficient to reproduce the qualitative behavior of the changes in number density with power. Following Czerwiec et al [30], the ratio of two spectral lines scales as

$$\frac{I_1}{I_2} = C\frac{X_1^{eff} n_1}{X_2^{eff} n_2}, \tag{5.1}$$

where $I_{1,2}$ is the intensity of lines $1, 2$, C is a constant, $n_{1,2}$ is the particle density of species $1, 2$, and $X^{eff}(T_e, n_e, ...)$ is the effective excitation rate, which is generally a function of electron temperature, electron density, etc. C accounts for those differences that are constant for the two lines considered: wave energy, Einstein coefficients, etc. While X^{eff} is function of number density, that dependence is simplified in a coronal equilibrium model to that represented by the electron distribution function. Since the electron distribution function is the same for the actinometric pairs, X^{eff} is a function of T_e [38]. A more complete calculation of X^{eff} is found using a collisional radiative model, which accounts for interactions of metastable states with electrons and is beyond the scope of this work. This line ratio method assumes that X^{eff} is either weakly dependent on T_e or that T_e is well-known and the rates can be calculated [38]. For the atomic spectral lines, we have good information regarding the required excitation energy and cross sections from the ground state to the emitting upper state [1, 59, 50]. However, for the molecular species, the excitation cross sections are not well correlated to emission lines [52, 23, 43]. This precludes us from being able to calculate the reaction rates. However, to satisfy this condition, we measured T_e in the source to be ~ 10 eV and to not vary significantly between thruster test conditions [122]. This introduces error into our assessment of relative intensity, which is higher for the lowest mass flow rates and highest powers where temperatures are slightly higher than in the rest of the test conditions. We estimate that error to be on the order of 50%.

5.1 Thruster Performance

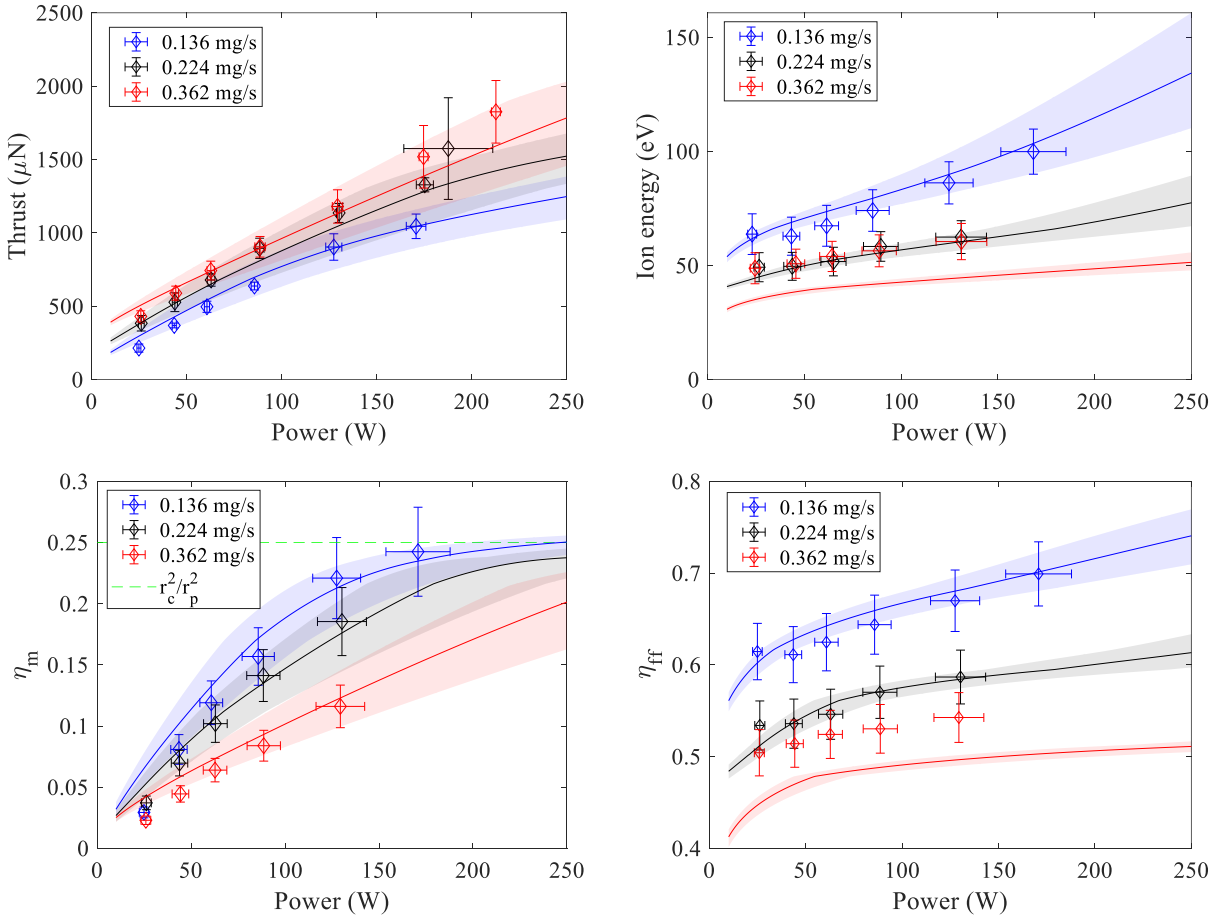

Figure 5.1: The experimental vs predicted (a) thrust, (b) ion energy, (c) mass utilization efficiency, and (d) frozen flow efficiency. The line of best fit corresponds to $r_c = 1/2r_t$ and $\xi = 0.6$.

Fig. 5.1(a) shows the measured and predicted thrust across all flow rates. We note a sublinear increase in thrust at high powers and low flow rates. The thrust is closely grouped at lower powers, with thrust increasing at a similar rate with power for all flow rates. At higher powers, however, the curves begin to deviate. This turning point is also visible in the ion energy. Fig. 5.1(b) shows the ion energy as measured by the RPA. The measured ion

energies show a shallow slope at low power, which becomes steeper as power increases. This increasing slope is correlated with the turning point in thrust shown in Fig. 5.1(a).

To explore the plasma composition factors that influence both thrust and ion energy, we look at Fig. 5.1(c), which shows the mass utilization efficiency, or ionization fraction, $\eta_m = g_0 I_{sp} / \cos\theta_{div} \sqrt{2qV_B/M}$, where g_0 is the acceleration of gravity, I_{sp} is specific impulse, θ_{div} is the divergence half angle, q is the electron charge, and M is the mass of the propellant. We see that η_m asymptotes to a fraction much less than 1, which suggests a saturation in ion concentration in the thruster. This saturation is correlated with the turning point in thrust and ion energy, indicating that the linear increase in thrust with power is primarily driven by increasing ionization and that once some saturation in ion concentration is reached, additional power goes into accelerating the ions. However, we observe that this additional acceleration is insufficient to maintain the linear increase in thrust with power.

While the behavior of the ion energy plots is a good indicator that additional power goes into accelerating the ions, we can evaluate how changes in mass utilization affects frozen flow efficiency. Fig. 5.1(d) presents the frozen flow efficiency as a function of power. We see that frozen flow efficiency slowly rises across the range of powers shown here. This agrees with predictions that higher electron temperatures increase frozen flow efficiency [121]. The experimental data, then, suggests that electrons are heated at an approximately uniform rate with respect to power. This implies that the hotter electrons contribute predominantly to accelerating the ions and not continuing to react with species in the thruster.

5.2 Modifications to the Theoretical Model

Between the visual evidence shown in Fig. 4.1(d) and the saturation in mass utilization efficiency, we consider modifications to our earlier model [121] to better represent the radial variation and incorporate loss mechanisms that were experimentally determined to contribute substantially to reduced performance. The one dimensional control volume model is described in detail elsewhere [121] and summarized here. We assume a cylindrically symmetric plasma source with device radius r_t and length L, with a primarily axial magnetic field

and a magnetic nozzle, a geometry suitable for modeling a variety of electrodeless thrusters (e.g., helicon, RF, and ECR thrusters).

Electron impact collisions dominate the chemistry inside the source, but resonant charge exchange collisions are also considered. We ignore any explicit time dependence in the solution and cross field diffusion, and we consider only axial variation in z. We ignore wall losses and assume the plasma in the thruster is azimuthally symmetric and that the plasma chemistry is frozen in the plume.

We use a chemical kinetics model to track the production and consumption of the neutral species H_2O, OH, O, and H and the ion species H_2O^+, OH^+, O^+, and H^+. This model conserves mass and momentum through these species, and we track the power in the thruster as

$$P = P_{ff} + P_v + P_{losses}, \tag{5.2}$$

where P_{ff} represents the frozen flow power losses, P_v represents the kinetic power, and P_{losses} represents other loss mechanisms (e.g., wall losses and coupling inefficiency).

The frozen flow power depends on $\epsilon_{j\to k}$, the energy required for the $j \to k$ reaction. For ionization reactions, this is an effective ionization energy which incorporates radiation and excitation losses. We assume the effective energy loss for ionization of a neutral species is twice the ionization energy, the asymptotic limit at high T_e of this type of energy loss for noble gases [73]. For dissociation reactions, this energy is equal to the dissociation energy, i.e., all excitation and radiation losses are incorporated into ionization energy loss.

The kinetic power includes a $g_u = \sqrt{\frac{\gamma_e+1}{\gamma_e-1}}$ term, which represents the additional acceleration ions undergo in a magnetic nozzle assuming polytropic expansion [79].

In our optimized thruster case [121], we assumed $P_{losses} = 0$, but the experimental data suggests three considerations that will improve the match between the predicted and observed performance: (1) we approximate the radial variation as consisting of a core plasma region along the center antenna surrounded by cold gas, (2) we incorporate wall losses along the central antenna, and (3) we include a coupling efficiency to account for discrepancy between

the power absorbed by the plasma and the power radiated from the thruster.

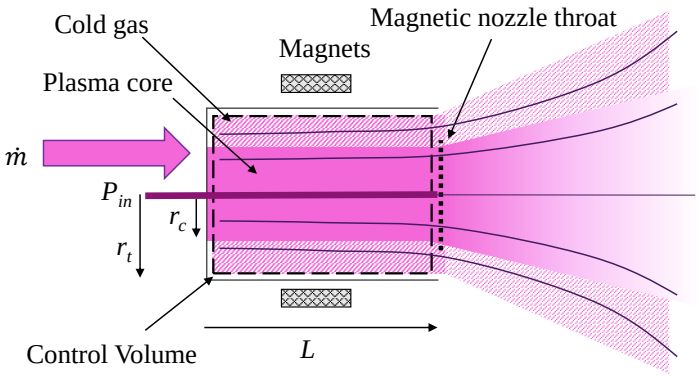

Figure 5.2: Schematic of the modeled thruster geometry.

With respect to the radial variation, the core plasma is defined by the free parameter r_c and shown schematically in Fig. 5.2. While the mass flow is uniformly distributed over the entire area of the thruster (defined by r_t), only the core plasma region absorbs the input power. The characteristics of the plasma core describe the ion energy, frozen flow losses, and expected spectral concentrations, while thrust and mass utilization efficiency contain information about the ratio of mass flow rate through the core to the overall mass flow rate, $\dot{m}_c/\dot{m} = r_c^2/r_t^2$.

By splitting the mass flow in this way, we modify the kinetic power of the thruster,

$$P_v = \frac{1}{2}\pi r_c^2 \left(\sum_{j \in ions} g_u^2 m_j n_j u_j^3 + \sum_{j \notin ions} m_j n_j u_j^3 \right) + \frac{1}{2} \frac{\dot{m} u_n^2}{\pi (r_t^2 - r_c^2)}, \tag{5.3}$$

where u_n is the neutral velocity of the propellant exhausting from the thruster, the first two terms on the right side represent the contribution of the plasma core to the kinetic exhaust, and the last term on the right represents the cold gas contribution. We use $u_n = M_a \sqrt{k_B T_n / m}$, where M_a is the mach number of the neutrals, k_B is Boltzmann's constant, $T_n = 298$ K is the neutral gas temperature, and m is the neutral propellant mass. Experimentally, we measure the cold gas thrust and find $M_a = 2.5$.

We next incorporate power losses to the walls (P_w) and through coupling (P_c). We assume the wall losses in the thruster are concentrated along the central antenna, in agreement with numerical work from Sánchez-Villar et al [111] and experimental results which showed moderate erosion along the antenna tested here. Wall losses along the central antenna are estimated following the model of Lafleur [69]. While this model is specifically for a helicon thruster, the assumptions regarding the axial magnetic field, magnetic nozzle, and cylindrical symmetry of the device are broadly applicable to the ECR thruster presented here and have been adapted for a similar thruster [20]. Lafleur assumes a Bohm-type diffusion coefficient inversely proportional to B and fits a sheath-edge-to-center density ratio h_r to experimental data. This h_r parameter folds into the larger wall losses as

$$P_w = 2\pi r_a h_r \int_0^L (n_e \bar{v_i} (\frac{5}{2} k_B T_e + \frac{k_B T_e}{2} \log[\frac{\bar{m_i}}{2\pi m_e}] + \bar{\epsilon_i}))dz \tag{5.4}$$

where r_a is the radius of the antenna, $\bar{v_i} = \sqrt{k_B T_e / \bar{m_i}}$ is the Bohm velocity of the average ion at z, $\bar{m_i}(z)$ is the average ion mass at z, and $\bar{\epsilon_i}(z)$ is the average ionization energy at z. We find $\bar{m_i}$ and $\bar{\epsilon_i}$ by taking a mean of the individual values. Eq. 5.4 accounts for the wall losses in a Bohm sheath, where the kinetic energy for the ions at the wall is equal to $k_B T_e/2(1 + \log(m_i/(2\pi m_e)))$ and for the electrons is equal to $2k_B T_e$ [73]. The collisional energy loss at the wall is equal to $\bar{\epsilon_i}$. While wall losses impact the thruster power, wall recombination is not considered as a source for neutrals.

The coupling power loss, P_c, scales with the total input power with the free parameter ξ, which represents the loss fraction. We calculate P_c as

$$P_c = \xi(P_v + P_{ff} + P_w). \tag{5.5}$$

This loss fraction ξ represents the power that is not coupled to the plasma and is instead lost through radiation to free space or through heating of the thruster. This power loss is separate from the reflected power that indicates an impedance mismatch in the line. That power loss is accounted for in the experimental data by the dual directional coupler.

5.3 Experimental Fit to Model

The free model parameters r_c, h_r, and ξ are varied to provide agreement with the experiment. We fix $h_r = 0.33$, which gives wall losses of $\sim 50\%$, comparable to Sànchez-Villar et al [111]. Next, we vary r_c and ξ to fit predicted thrust and ion energy to that determined in the experiment. We varied first r_c to capture the general trends in thrust and ion energy and then used ξ to match power to the experimental results. Reducing r_c inherently lows the mass utilization efficiency; by assuming only a fraction of the mass flow rate interacts significantly with the thruster power source, we cap the mass utilization efficiency at r_c^2/r_t^2. The best fit parameters we found are $r_c = 1/2r_t$ and $\xi = 0.6$. This implies that only 40% of the power available at the thruster actually is absorbed by the plasma.

Fig. 5.3 shows the comparison between the observed spectral ratios and the model predictions for number density relative to O at the thruster exhaust plane. These model predictions are only for the plasma core, which we expect to dominate the emission intensity. These ratios largely start out high, as there is expected to be a small fraction of O at lower powers. As power increases, the population of O increases, and we see variation in expected concentrations. These plots are normalized relative to the spectral intensity at 0.224 mg/s and 25 W of power to facilitate comparison between the flow rates and species concentrations for both the measured and modeled data.

In Fig. 5.3(a), we observe the variation of H_2O with O. The model predicts a sharp drop off, but the observed spectra do not decay as rapidly. Additionally, there is still substantial emission from water vapor at higher powers that asymptotes to a relatively constant value. This qualitatively agrees with our suggestion of a core plasma surrounded by a region of cold gas. Fig. 5.3(b) shows H concentration relative to O, which decays not as rapidly as the H_2O concentration. H is predominantly formed from the initial dissociation reaction of water and is destroyed by the formation of the H^+ ion. The experimental trends generally agree with the predicted trends, although we again notice that the H line ratios do not fall off as sharply predicted and still emit substantially at higher powers, which may again provide additional

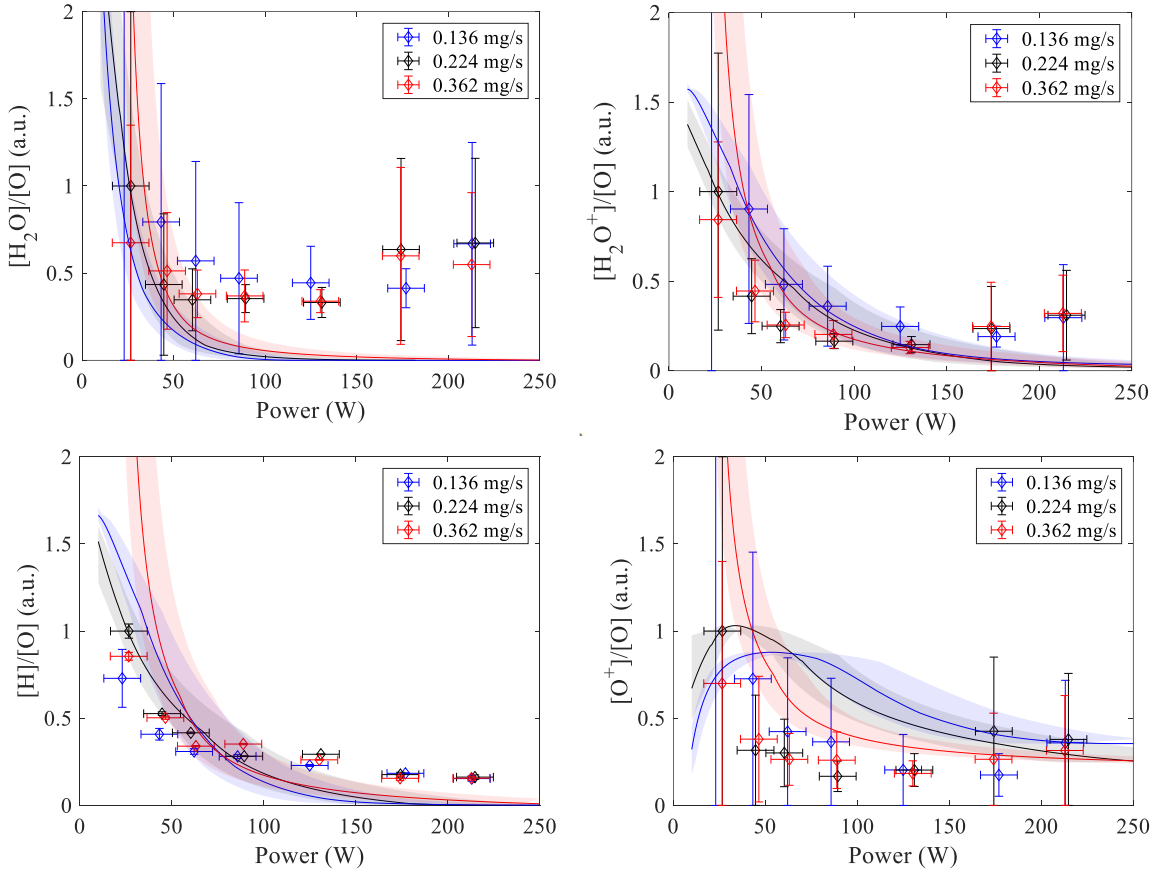

Figure 5.3: The observed spectral ratios compared with model predictions for the species (a) H_2O, (b) H, (c) H_2O^+, and (d) OH^+. The experimental data is a ratio of line intensities, and the modeled data is a ratio of number densities.

evidence to suggest there is water in the plume that interacts with the core plasma. This could additionally be related to the optics view angle into the thruster, which incorporates not only the thruster plume but part of the inner channel.

The second column of Fig. 5.3 shows the ion concentrations in the plasma. The model predicts a slower drop off for the H_2O^+ compared with the neutral H_2O, which generally agrees with the observed emission and reflects the extended presence of molecular ions in the plume. Fig. 5.3(d) shows O^+ intensity relative to O. This ion species, which is an end state of

propellant dissociation and ionization in the thruster, shows a different expected trend at the lower flow rates than the other species. We see that the predicted relative concentration rises to a peak at moderate powers then falls off. This suggests that O^+ grows at a similar rate to O until some threshold power. Below this threshold power, lower electron temperatures encourage the reactions that produce O^+. Above this threshold power, the species that produce O^+ exhaust before they can react significantly with electrons in the thruster.

5.4 Conclusion

By incorporating a Bohm sheath model for wall losses to the central antenna, a power coupling efficiency, and a plasma core approximation to radial variation, we are able to capture agreement between measured and predicted performance metrics. Frozen flow efficiency slowing increases with power, suggesting that the electron heating mechanism is relatively constant throughout the range of conditions tested here. As the plasma core reaches a saturation value in mass utilization, additional power increases ion energy. The actinometric assessement of species concentrations qualitatively agrees with model predictions and variation between the two supports the core plasma assumptions. This work enables a closer look at the thruster plasma chemistry that influences the bulk performance.

Chapter 6

CONCLUSIONS AND FUTURE WORK

This dissertation has discussed the feasibility of using water vapor propellant in electron cyclotron resonance thrusters. Molecular plasmas have been studied for use in electric propulsion thrusters, and water's ubiquity makes it an excellent initial candidate. However, the plasma chemistry complicates thruster design. We explored this complexity theoretically and experimentally in this work.

Computational results show that water would perform comparably to state of the art propellants provided the plasma conditions encourage molecular ion formation over atomic ion formation or molecular dissociation. These conditions are largely driven by the electron temperature (better performance is associated with $T_e > 15$ eV) and the combination of molecule concentration and residence time in the thruster channel (as described by $p_0 L$). The approach taken here is broadly applicable to other molecular species and applications outside of propulsion.

The results from the computational work informed the design of an ECR thruster for experimental validation. The APEX thruster was operated with the argon, krypton, xenon, and water vapor. Where available, the APEX thruster was compared with published results from other ECR thrusters. We explored the differences in propellant performance as they varied with ionization cost, ionization cross section, and molecular mass. Frozen flow efficiency in the APEX thruster did not vary significantly due to ionization cost or cross section; however, multiple reaction pathways and dissociation reactions in the water vapor propellant did decrease frozen flow efficiency. We found that mass utilization efficiency for all species was predominantly influenced by the neutral density and residence time in the thruster, which supports our model predictions finding self-similar behavior for $p_0 L$ for water

vapor. Lighter species (water and argon) have higher ion exhaust velocities and lower mass utilization efficiencies than heavier species (krypton and xenon). These competing metrics yield comparable specific impulses for all species tested. Wall losses are concentrated along the central antenna and contribute to low thrust efficiency for all species.

We discovered that three modifications to the original model were necessary in order to match the water vapor experimental data: incorporating radial plasma variation, wall losses on the central antenna, and coupling efficiency. The radial variation was approximated simply as a plasma core that absorbed the RF power surrounded by a cold gas component. The wall losses incorporated a Bohm sheath approximation to the flow to the central antenna; including these wall losses is supported by empirical evidence of significant erosion of this antenna during testing and numerical simulations suggesting that these losses and coupling inefficiency are important. With these modifications, the model agreed with experimental data and provided additional information regarding how plasma composition varied with power. The spectral intensities corroborated the plasma density information.

The results of the work presented here lead to multiple potential paths for future work. The main driver in future ECR studies should be improving thruster efficiency. Based on the results shown in Ch. 4, reducing wall losses and improving coupling efficiency will have a large impact on increasing thruster efficiency for all propellants. These improvements should incorporate modeling of the magnetic field topology and the propagation of RF in the thruster channel. We additionally suggest material improvements on the thruster antenna, to both improve resiliency and additionally better propagate the wave energy into the plasma.

As coupling efficiency improves in the thruster, the future experimenter should feel more comfortable in increasing power. Higher powers enable higher electron temperatures, lower frozen flow losses, higher ion energies, and overall improved performance. However, as thruster power increases, additional care should be put into thermal mitigation efforts, to potentially include radiation surfaces or incorporating electromagnets vs permanent magnets.

BIBLIOGRAPHY

[1] *Atomic and Plasma–Material Interaction Data for Fusion*. Number 4 in Atomic and Plasma–Material Interaction Data for Fusion. INTERNATIONAL ATOMIC ENERGY AGENCY, Vienna, 1993.

[2] E. Ahedo and M. Merino. Two-dimensional supersonic plasma acceleration in a magnetic nozzle. *Physics of Plasmas*, 17(7), 2010.

[3] Eduardo Ahedo and Jaume Navarro-Cavallé. Helicon thruster plasma modeling: Two-dimensional fluid-dynamics and propulsive performances. *Physics of Plasmas*, 20(4), 2013.

[4] N. L. Aleksandrov, S. V. Kindysheva, A. A. Kirpichnikov, I. N. Kosarev, S. M. Starikovskaia, and A. Yu Starikovskii. Plasma decay in N2, CO2 and H2O excited by high-voltage nanosecond discharge. *Journal of Physics D: Applied Physics*, 40(15):4493–4502, 2007.

[5] Z. Amitay, D. Zajfman, P. Forck, T. Heupel, M. Grieser, D. Habs, R. Repnow, D. Schwalm, A. Wolf, and Steven L. Guberman. Dissociative recombination of cold O[Formula Presented]: Evidence for indirect recombination through excited core Rydberg states. *Physical Review A - Atomic, Molecular, and Optical Physics*, 53(2):R644–R647, 1996.

[6] R. Barni, A. Decina, S. Zanini, A. D'Orazio, and C. Riccardi. Experimental investigation of hydrogen peroxide RF plasmas. *Plasma Sources Science and Technology*, 25(2), 2016.

[7] R. Baskaran, S. K. Jain, and S. S. Ramamurthi. ECR ion source using slow wave structures. *Review of Scientific Instruments*, 63(4):2525–2528, 1992.

[8] Brian Beal. The Air Force Research Laboratory's In-Space Propulsion Program. In *38th Annual AAS Guidance & Control Conference, Breckenridge, CO; 2 Feb 2015*, 2015.

[9] Brian Eric Beal. *Clustering of Hall Effect Thrusters for High-Power Electric Propulsion Applications*. PhD thesis, University of Michigan, 2004.

[10] A. V. Bernatskiy, V. N. Ochkin, and I. V. Kochetov. Multispectral actinometry of water and water-derivative molecules in moist, inert gas discharge plasmas. *Journal of Physics D: Applied Physics*, 49(39), 2016.

[11] J. P. Boeuf and L. Garrigues. Low frequency oscillations in a stationary plasma thruster. *Journal of Applied Physics*, 84(7):3541, oct 1998.

[12] A. Bouchoule, Ch Philippe-Kadlec, M. Prioul, F. Darnon, M. Lyszyk, L. Magne, D. Pagnon, S. Roche, M. Touzeau, S. Béchu, P. Lasgorceix, N. Sadeghi, N. Dorval, J. P. Marque, and J. Bonnet. Transient phenomena in closed electron drift plasma thrusters: Insights obtained in a French cooperative program. *Plasma Sources Science and Technology*, 10(2):364–377, 2001.

[13] Iain D. Boyd, Douglas B. Van Gilder, and Xiaoming Liu. Monte Carlo Simulation of Neutral Xenon Flows in Electric Propulsion Devices. *Journal of Propulsion and Power*, 14(6):1009–1015, 1998.

[14] John E. Brandenburg, John Kline, and Daniel Sullivan. The microwave electro-thermal (MET) thruster using water vapor propellant. *IEEE Transactions on Plasma Science*, 33(2 II):776–782, 2005.

[15] Jerome Bredin, Pascal Chabert, and Ane Aanesland. Langmuir probe analysis in electronegative plasmas. *Physics of Plasmas*, 21(12), 2014.

[16] Daniel L. Brown, Mitchell L.R. Walker, James Szabo, Wensheng Huang, and John E. Foster. Recommended practice for use of faraday probes in electric propulsion testing. *Journal of Propulsion and Power*, 33(3):582–613, 2017.

[17] Daniel Lucas Brown. *Investigation of Low Discharge Voltage Hall Thruster Characteristics and Evaluation of Loss Mechanisms*. PhD thesis, University of Michigan, 2009.

[18] R.B. Cairns, H Harrison, and R. I. Schoen. Dissociative photoionization of H2O. *The Journal of Chemical Physics*, 55:4886, 1971.

[19] F. Cannat, T. Lafleur, J. Jarrige, P. Chabert, P. Q. Elias, and D. Packan. Optimization of a coaxial electron cyclotron resonance plasma thruster with an analytical model. *Physics of Plasmas*, 22(5), 2015.

[20] F. Cannat, T. Lafleur, J. Jarrige, P. Chabert, P.-Q Q. Elias, and D. Packan. Optimization of a coaxial electron cyclotron resonance plasma thruster with an analytical model. *Physics of Plasmas*, 22(5):11101, 2015.

[21] Felix Cannat, Julien Jarrige, Paul-quentin Elias, and Denis Packan. Experimental investigation of magnetic gradient influence in a coaxial ECR plasma. *Space Propulsion 2014*, 2014.

[22] Angela M. Capece, James E. Polk, and Joseph E. Shepherd. Decoupling the Thermal and Plasma Effects on the Operation of a Xenon Hollow Cathode With Oxygen Poisoning Gas. *IEEE Transactions on Plasma Science*, 43(9):3249–3255, 2015.

[23] K. Chakrabarti, V. Laporta, and Jonathan Tennyson. Calculated cross sections for low energy electron collision with OH. *Plasma Sources Science and Technology*, 28(8), 2019.

[24] Steven D. Chambreau, Denisia M. Popolan-Vaida, Ghanshyam L. Vaghjiani, and Stephen R. Leone. Catalytic Decomposition of Hydroxylammonium Nitrate Ionic Liquid: Enhancement of NO Formation. *Journal of Physical Chemistry Letters*, 8(10):2126–2130, 2017.

[25] C. Charles, R. W. Boswell, R. Laine, and P. MacLellan. An experimental investigation of alternative propellants for the helicon double layer thruster. *Journal of Physics D: Applied Physics*, 41(17), 2008.

[26] Francis Chen. *Introduction to Plasma Physics and Controlled Fusion*. Plenum Press, New York and London, second edition, 1984.

[27] G. Cifali, T. Misuri, P. Rossetti, M. Andrenucci, D. Valentian, and D. Feili. Preliminary characterization test of HET and RIT with nitrogen and oxygen. *47th AIAA/ASME/SAE/ASEE Joint Propulsion Conference and Exhibit 2011*, (August):1–16, 2011.

[28] S. Correyero, J. Jarrige, D. Packan, and E. Ahedo. Plasma beam characterization along the magnetic nozzle of an ECR thruster. *Plasma Sources Science and Technology*, 28(9), 2019.

[29] S. Correyero, M. Merino, Paul Quentin Elias, J. Jarrige, D. Packan, and E. Ahedo. Characterization of diamagnetism inside an ECR thruster with a diamagnetic loop. *Physics of Plasmas*, 26(5), 2019.

[30] T. Czerwiec, F. Greer, and D. B. Graves. Nitrogen dissociation in a low pressure cylindrical ICP discharge studied by actinometry and mass spectrometry. *Journal of Physics D: Applied Physics*, 38(24):4278–4289, 2005.

[31] K. Dannenmayer and Stéphane Mazouffre. Electron flow properties in the far-field plume of a Hall thruster. *Plasma Sources Science and Technology*, 22(3), 2013.

[32] S T Demetriades. A novel system for space flight using a propulsive fluid accumulator. *J. Brit. Interplanet. Soc.*, 17, 9 1959.

[33] Kevin D. Diamant. Microwave Cathode for Air Breathing Electric Propulsion. *31st International Electric Propulsion Conference*, (1):IEPC–2009–015, 2009.

[34] Kevin D. Diamant, Byron L. Zeigler, and Ronald B. Cohen. Microwave electrothermal thruster performance. *Journal of Propulsion and Power*, 23(1):27–34, 2007.

[35] Patrick Dietz, Waldemar Gärtner, Quirin Koch, Peter E Köhler, Yan Teng, Peter R Schreiner, Kristof Holste, and Peter J Klar. Molecular propellants for ion thrusters. *Plasma Sources Science and Technology*, 2019.

[36] Vincent M. Donnelly and Avinoam Kornblit. Plasma etching: Yesterday, today, and tomorrow. *Journal of Vacuum Science & Technology A: Vacuum, Surfaces, and Films*, 31(5):050825, sep 2013.

[37] John V Dugan and Ronald J Sovie. VOLUME ION PRODUCTION COSTS IN TENUOUS PLASMAS: A General Atom theory and Detailed Results for Helium, Argon, and Cesium. *NASA TN D-4150, NASA Lewis Research Center, ...*, (September), 1967.

[38] U. Fantz. Basics of plasma spectroscopy. *Plasma Sources Science and Technology*, 15(4), 2006.

[39] Amnon Fruchtman. Neutral depletion in a collisionless plasma. *IEEE Transactions on Plasma Science*, 36(2 PART 1):403–413, 2008.

[40] Robert J Goldston and Paul H Rutherford. *Introduction To Plasma Physics*, volume 01. Institute of Physics Publishing, Bristol and Philadelphia, 1995.

[41] Vasco Guerra. The case for in situ resource utilisation for oxygen production on Mars by non- equilibrium plasmas. *Plasma Sources Sci. Technol.*, 26, 2017.

[42] Sungyoung Ha. Erosion and Performance Scaling of Electrodeless Plasma Thrusters with a Magnetic Nozzle. Master's thesis, University of Washington, 2021.

[43] James R. Hamilton, Alexandre Faure, and Jonathan Tennyson. Electron-impact excitation of diatomic hydride cations II: OH+ and SH+. *Monthly Notices of the Royal Astronomical Society*, 476(3):2931–2937, 2018.

[44] Nicholas-E. Harmansa, Stefanos Fasoulas, Georg Herdrich, Adam Boxberger, Christoph Montag, and Ulrich Gotzig. Hybrid Electric Propulsion System based on Water Electrolysis. *International Electric Propulsion Conference*, pages 1–4, 2019.

[45] Richard R. Hofer. Development and Characterization Impulse Xenon Hall Thrusters. Technical Report NASA/CR-2004-213099, University of Michigan, 2004.

[46] Lingyun Hou, Yan Shen, Huangzai Tang, and Wenhua Zhao. Improvement on stability of water arcjet. *IEEE Transactions on Plasma Science*, 39(1 PART 2):608–614, 2011.

[47] Wensheng Huang and Rohit Shastry. Analysis of Wien filter spectra from Hall thruster plumes. *Review of Scientific Instruments*, 86(7), 2015.

[48] Yosuke Ichikawa, Takeshi Sakamoto, Atsushi Nezu, Haruaki Matsuura, and Hiroshi Akatsuka. Actinometry measurement of dissociation degrees of nitrogen and oxygen in N2-O2microwave discharge plasma. *Japanese Journal of Applied Physics*, 49(10):1061011–10610116, 2010.

[49] L. M. Isola, B. J. Gomez, and V. Guerra. Determination of the electron temperature and density in the negative glow of a nitrogen pulsed discharge using optical emission spectroscopy. *Journal of Physics D: Applied Physics*, 43(1), 2010.

[50] Y. Itikawa, S. Hara, T. Kato, S. Nakazaki, M. S. Pindzola, and D. H. Crandall. Electron-impact cross sections and rate coefficients for excitations of carbon and oxygen ions. *Atomic Data and Nuclear Data Tables*, 33(1):149–193, 1985.

[51] Yukikazu Itikawa. Cross sections for electron collisions with carbon dioxide. *Journal of Physical and Chemical Reference Data*, 31(3):749–767, 2002.

[52] Yukikazu Itikawa and Nigel Mason. Cross sections for electron collisions with water molecules. *Journal of Physical and Chemical Reference Data*, 34(1):1–22, 2005.

[53] Robert G Jahn and Edgar Y Choueiri. Electric Propulsion History. 5:125–141, 2002.

[54] Julien Jarrige, Sara Correyero, Paul-Quentin Elias, and Denis Packan. Investigation on the ion velocity distribution in the magnetic nozzle of an ECR plasma thruster using LIF measurements. *International Electric Propulsion Conference*, pages 1–10, 2017.

[55] Julien Jarrige, Paul-Quentin Elias, and Denis Packan. Performance Comparison of an ECR Plasma Thruster using Argon and Xenon as Propellant Gas. *Internationl Electric Propulsion Conference*, page 420, 2013.

[56] M. J. Jensen, R. C. Bilodeau, O. Heber, H. B. Pedersen, C. P. Safvan, X. Urbain, D. Zajfman, and L. H. Andersen. Dissociative recombination and excitation of H2O+ and HDO+. *Physical Review A*, 60(4):2970–2976, 1999.

[57] George F. Karabadzhak, Yu Hui Chiu, and Rainer A. Dressler. Passive optical diagnostic of Xe propelled Hall thrusters. II. Collisional-radiative model. *Journal of Applied Physics*, 99(11), 2006.

[58] A Kato and E Asano. Comparison of Recombination Rate Coefficients Given by Empirical Formulas for Ions from Hydrogen through Nickel. *Research Report NIFS-DATA Series*, 54, 1999.

[59] H. M. Katsch, A. Tewes, E. Quandt, A. Goehlich, T. Kawetzki, and H. F. Döbele. Detection of atomic oxygen: Improvement of actinometry and comparison with laser spectroscopy. *Journal of Applied Physics*, 88(11):6232–6238, 2000.

[60] D. Kaufman, D. Goodwin, and J. Sercel. Experimental studies of an ECR plasma thruster. 1993.

[61] D. A. Kaufman and D. G. Goodwin. Plume characteristics of an ECR thruster. pages 355–360, 1993.

[62] June Young Kim, Jae Young Jang, K. S. Chung, Kyoung Jae Chung, and Y. S. Hwang. Time-Dependent Kinetic Analysis of Trapped Electrons in a Magnetically Expanding Plasma. *Plasma Sources Science and Technology*, 28(7), 2019.

[63] Sang-Wook Kim. *Experimental Investigations of Plasma Parameters and Species-Dependent Ion Energy Distribution in the Plasma Exhaust Plume of a Hall Thruster*. PhD thesis, University of Michigan, 1999.

[64] Sang Wook Kim and Alec D. Gallimore. Plume study of a 1.35-kW SPT-100 using a ExB probe. *Journal of Spacecraft and Rockets*, 39(6):904–909, 2002.

[65] David Kirtley, Anthony Pancotti, John Slough, and Chris Pihl. Steady operation of an FRC thruster on Martian atmosphere and liquid water propellants. *48th AIAA/ASME/SAE/ASEE Joint Propulsion Conference and Exhibit 2012*, (August):1–17, 2012.

[66] H. Koizumi, K. Komurasaki, and Y. Arakawa. Development of thrust stand for low impulse measurement from microthrusters. *Review of Scientific Instruments*, 75(10 I):3185–3190, 2004.

[67] H. G. Kosmahl, D. B. Miller, and G. W. Bethke. Plasma acceleration with microwaves near cyclotron resonance. *Journal of Applied Physics*, 38(12):4576–4582, 1967.

[68] Tomàš Kozàk and Annemie Bogaerts. Splitting of CO2by vibrational excitation in non-equilibrium plasmas: A reaction kinetics model. *Plasma Sources Science and Technology*, 23(4), 2014.

[69] T. Lafleur. Helicon plasma thruster discharge model. *Physics of Plasmas*, 21(4), 2014.

[70] D. Levko, A. Shchedrin, V. Chernyak, S. Olszewski, and O. Nedybaliuk. Plasma kinetics in ethanol/water/air mixture in a 'tornado'-type electrical discharge. *Journal of Physics D: Applied Physics*, 44(14), 2011.

[71] B. R. Lewis, I. M. Vardavas, and J. H. Carver. AERONOMIC DISSOCIATION OF WATER VAPOR BY SOLAR H LYMAN alpha RADIATION. *Journal of Geophysical Research*, 88(A6):4935–4940, 1983.

[72] X. Li, Y.-L. Huang, and G. D. Flesch. A state-selected study of the ion – molecule. 928(September 1996), 1997.

[73] M. A. Lieberman and A. J. Lichtenberg. *Principles of Plasma Discharge and Materials Processing*. John Wiley & Sons Inc, New York, USA, 1994.

[74] Jesse a Linnell. *An Evaluation of Krypton Propellant in Hall Thrusters*. PhD thesis, University of Michigan, 2007.

[75] Jesse A. Linnell and Alec D. Gallimore. Krypton performance optimization in high-voltage hall thrusters. *Journal of Propulsion and Power*, 22(4):921–924, 2006.

[76] C. Randal Lishawa, Rainier A. Dressler, James A. Gardner, Richard H. Salter, and Edmond Murad. Cross sections and product kinetic energy analysis of H2O – H2O collisions at suprathermal energies. *The Journal of Chemical Physics*, 93, 1990.

[77] J. M. Little and E. Y. Choueiri. Electron Cooling in a Magnetically Expanding Plasma. *Physical Review Letters*, 117(22):1–5, 2016.

[78] J. M. Little and E. Y. Choueiri. Electron Demagnetization in a Magnetically Expanding Plasma. *Physical Review Letters*, 123, 2019.

[79] Justin Little and Edgar Choueiri. The Influence of Induced Currents on Magnetic Nozzle Acceleration and Plasma Detachment. *46th AIAA/ASME/SAE/ASEE Joint Propulsion Conference & Exhibit*, (July), 2010.

[80] Justin M Little. *Performance Scaling of Magnetic Nozzles for Electric Propulsion*. PhD thesis, Princeton University, 2015.

[81] Justin M Little and Edgar Y Choueiri. Critical Condition for Plasma Confinement in the Source of a Magnetic Nozzle Flow. *IEEE Transactions on Plasma Science*, 43(1):277–286, 2015.

[82] Robert B. Lobbia and Brian E. Beal. Recommended practice for use of Langmuir probes in electric propulsion testing. *Journal of Propulsion and Power*, 33(3):566–580, 2017.

[83] B. Longmier, S. Baalrud, and N. Hershkowitz. Nonambipolar electron source. *Review of Scientific Instruments*, 77(11), 2006.

[84] X. Lu, G. V. Naidis, M. Laroussi, S. Reuter, D. B. Graves, and K. Ostrikov. Reactive species in non-equilibrium atmospheric-pressure plasmas: Generation, transport, and biological effects. *Physics Reports*, 630(April):1–84, 2016.

[85] H. Luna, A. L.F. De Barros, J. A. Wyer, S. W.J. Scully, J. Laconte, P. M.Y. Garcia, G. M. Sigaud, A. C.F. Santos, V. Senthil, M. B. Shah, C. J. Latimer, and E. C. Montenegro. Water-molecule dissociation by proton and hydrogen impact. *Physical Review A - Atomic, Molecular, and Optical Physics*, 75(4):1–11, 2007.

[86] Natalia MacDonald-Tenenbaum, Quinn Pratt, Michael Nakles, Nickolas Pilgram, Michael Holmes, and William Hargus. Background Pressure Effects on Ion Velocity Distributions in an SPT-100 Hall Thruster. *Journal of Propulsion and Power*, 35(2):403–412, 2019.

[87] Colleen M. Marrese, Alec D. Gallimore, William A. Mackie, and David E. Evans. The design of a cathode to operate in an oxygen-rich environment. *AIP Conference Proceedings*, 387(305), 1997.

[88] Morito Matsuoka and Ken'ichi Ono. Magnetic field gradient effects on ion energy for electron cyclotron resonance microwave plasma stream. *Journal of Vacuum Science & Technology A: Vacuum, Surfaces, and Films*, 6(1):25–29, 1988.

[89] Stéphane Mazouffre. Electric propulsion for satellites and spacecraft: established technologies and novel approaches. *Plasma Sources Science and Technology*, 25(3):033002, 2016.

[90] Mario Merino and Eduardo Ahedo. Plasma detachment in a propulsive magnetic nozzle via ion demagnetization. *Plasma Sources Science and Technology*, 23(3), 2014.

[91] Mario Merino and Eduardo Ahedo. Influence of electron and ion thermodynamics on the magnetic nozzle plasma expansion. *IEEE Transactions on Plasma Science*, 43(1):244–251, 2015.

[92] R Moloney, B Karadag, A Lucca Fabris, Surrey Space Centre, United Kingdom, D Staab, A Frey, A Garbayo, L Shadbolt, E Rosati Azevedo, United Kingdom, D Faircloth, S Lawrie, O Tarvainen, and Muon Facility. Experimental Validation and Performance Measurements of an ECR Thruster Operating on Multiple Propellants. *36th International Electric Propulsion Conference*, pages 1–13, 2019.

[93] N. A. Morrison, C. William, and W. I. Milne. Methane chemistry involved in a low-pressure electron cyclotron wave resonant plasma discharge. *Journal of Applied Physics*, 94(11):7031–7043, 2003.

[94] Yuichi Nakagawa, Hiroyuki Koizumi, Hiroki Kawahara, and Kimiya komurasaki. Performance characterization of a miniature microwave discharge ion thruster operated with water. *Acta Astronautica*, (November 2017):0–1, 2018.

[95] Sonca V. T. Nguyen. *Operating a radio-frequency plasma source on water vapor*. PhD thesis, University of Michigan, 2009.

[96] Guohua Ni, Yan Lan, Cheng Cheng, Yuedong Meng, and Xiangke Wang. Reforming of methane and carbon dioxide by DC water plasma at atmospheric pressure. *International Journal of Hydrogen Energy*, 36(20):12869–12876, 2011.

[97] Kazutaka Nishiyama. Air Breathing Ion Engine Concept. In *54th International Astronautical Congress*, number October, 2003.

[98] David Y. Oh, Thomas Randolph, Scott Kimbrel, and Manuel Martinez-Sanchez. End-to-End Optimization of Chemical-Electric Orbit-Raising Missions. *Journal of Spacecraft and Rockets*, 41(5):831–839, 2004.

[99] F Paschen. *Ann. Phys.*, 273:69–96, 1889.

[100] RWB Pearse and AG Gaydon. *The Identification of Molecular Spectra, 4th ed.* Wiley, New York, 1976.

[101] Leonid Pekker and Michael Keidar. Analysis of air breathing hall effect thruster. *42nd AIAA Plasmadynamics and Lasers Conference*, (June):1–12, 2011.

[102] Elaine M. Petro and Raymond J. Sedwick. Effects of water-vapor propellant on electrodeless thruster performance. *Journal of Propulsion and Power*, 33(6):1410–1417, 2017.

[103] Elaine M. Petro, Raymond J. Sedwick, and Lubos Brieda. Second-order chemistry effects in an electrodeless water plasma thruster. *AIAA Propulsion and Energy Forum and Exposition, 2019*, (August):1–20, 2019.

[104] James E. Polk, Anthony Pancotti, Thomas Haag, Scott King, Mitchell Walker, Joseph Blakely, and John Ziemer. Recommended Practice for Thrust Measurement in Electric Propulsion Testing. *Journal of Propulsion and Power*, 33(3):539–555, 2017.

[105] John L. Power. Microwave Electrothermal Propulsion for Space. *IEEE Transactions on Microwave Theory and Techniques*, 40(6):1179–1191, 1992.

[106] Y. Raitses, J. Ashkenazy, and M. Guelman. Propellant Utilization in Hall Thrusters. *Journal of Propulsion and Power*, 14(2):247–253, 1998.

[107] E. Rosati Azevedo, K. Swar, D. Staab, E. Longhi, A. Garbayo, B. Karadag, J. Stubbing, R. Moloney, A. Lucca Fabris, T. le Toux, O. Taravainen, and D. Faircloth. Xjet : Design Upgrade and Preliminary Characterization for an Electrodeless Ecr Thruster. *Space Propulsion 2020*, 2021.

[108] Krstic P S and Schultz D R. Elastic and related transport cross sections for collisions among isotopomers ofh+ + h, h+ + h2,h+ + he, h + h, and h + h2. Technical report, 1999.

[109] N Sadeghi, T Nakano, and D Trevor. Ion transport in an electro cyclotron resonance plasma. *Journal of Applied Physics*, 70:2552, 1991.

[110] Seiji Samukawa and Shuichi Furuoya. Time-modulated electron cyclotron resonance plasma discharge for controlling generation of reactive species. *Applied Physics Letters*, 63(15):2044–2046, 1993.

[111] Álvaro Sánchez-Villar, Jiewei Zhou, Eduardo Ahedo, and Mario Merino. Coupled plasma transport and electromagnetic wave simulation of an ECR thruster. *Plasma Sources Science and Technology*, 30(4), 2021.

[112] Gerald B. Sanders. Advancing In Situ Resource Utilization Capabilities To Achieve a New Paradigm in Space Exploration. *2018 AIAA SPACE and Astronautics Forum and Exposition*, (September):1–9, 2018.

[113] JE Sansonetti, WC Martin, and SL Young. Handbook of basic atomic spectroscopic data, 2005. Accessed 27 Nov 2021.

[114] Carsten A Scharlemann and Thomas M York. PULSED PLASMA THRUSTER USING WATER PROPELLANT, PART I: INVESTIGATION OF THRUST BEHAVIOR AND MECHANISM. 2003.

[115] Tony Schonherr, Kimiya Komurasaki, Francesco Romano, Bartomeu Massuti-Ballester, and Georg Herdrich. Analysis of atmosphere-breathing electric propulsion. *IEEE Transactions on Plasma Science*, 43(1):287–294, 2015.

[116] Alexander Schwertheim and Aaron Knoll. The Water Electrolysis Hall Effect Thruster. *36th International Electric Propulsion Conference*, pages 1–12, 2019.

[117] J. C. Sercel. *An Experimental and Theoretical Study of the ECR Plasma Engine*. PhD thesis, California Institute of Technology, 1993.

[118] M. B. Shah, D. S. Elliott, and H. B. Gilbody. Pulsed crossed-beam study of the ionisation of atomic hydrogen by electron impact. *Journal of Physics B: Atomic and Molecular Physics*, 20(14):3501–3514, 1987.

[119] Rohit Shastry, Richard R. Hofer, Bryan M. Reid, and Alec D. Gallimore. Method for analyzing E×B probe spectra from Hall thruster plumes. *Review of Scientific Instruments*, 80(6), 2009.

[120] J. P. Sheehan, Yevgeny Raitses, Noah Hershkowitz, and Michael McDonald. Recommended practice for use of emissive probes in electric propulsion testing. *Journal of Propulsion and Power*, 33(3):614–637, 2017.

[121] Anna J. Sheppard and Justin M. Little. Scaling laws for electrodeless plasma propulsion with water vapor propellant. *Plasma Sources Science and Technology*, 29(4), 2020.

[122] Anna J Sheppard and Justin M Little. Performance Analysis of an Electron Cyclotron Resonance Thruster with Various Propellants. *AIAA Propulsion and Energy Forum 2021*, 2021.

[123] Tiago Silva, Nikolay Britun, Thomas Godfroid, and Rony Snyders. Optical characterization of a microwave pulsed discharge used for dissociation of CO2. *Plasma Sources Science and Technology*, 23(2), 2014.

[124] Lake A. Singh and Mitchell L.R. Walker. A review of research in low earth orbit propellant collection. *Progress in Aerospace Sciences*, 75:15–25, 2015.

[125] John T Slough, David E Kirtley, and Thomas Weber. Pulsed Plasmoid Propulsion: The ELF Thruster. *31 th International Electric Propulsion Conference*, pages 1–24, 2009.

[126] D Staab, A Frey, A Garbayo, L Shadbolt, A Lucca Fabris, A Gurciullo, and P E Grondein. AQUAJET : An Electrodeless ECR Water Thruster Space Propulsion 2018 Barcelo Renacimiento Hotel, Seville, Spain / 14 - 18 May 2018. (May), 2018.

[127] RF Stebbings, A C I-i Smith, and I-i Ehrhardt. Charge Transfer between Oxygen Atoms and O+ and H+ Ions. 69(11), 1964.

[128] K Swar, D Staab, A Garbayo, L Shadbolt, United Kingdom, S Masillo, A Lucca Fabris, B Karadag, R Moloney, and United Kingdom. Design and testing of a μN mN torsional thrust balance with wireless microwave power transmission. (November):1–13, 2019.

[129] James Szabo and Mike Robin. Plasma species measurements in the plume of an iodine fueled Hall Thruster. *Journal of Propulsion and Power*, 30(5):1357–1367, 2014.

[130] Kazunori Takahashi. Helicon-type radiofrequency plasma thrusters and magnetic plasma nozzles. *Reviews of Modern Plasma Physics*, 3(1):3, 2019.

[131] Kazunori Takahashi, Christine Charles, Rod Boswell, and Akira Ando. Adiabatic Expansion of Electron Gas in a Magnetic Nozzle. *Physical Review Letters*, 120(4):45001, 2018.

[132] Yoshinori Takao, Koji Eriguchi, and Kouichi Ono. A miniature electrothermal thruster using microwave-excited microplasmas: Thrust measurement and its comparison with numerical analysis. *Journal of Applied Physics*, 101(12), 2007.

[133] V. Tarnovsky, H. Deutsch, and K. Becker. Electron impact ionization of the hydroxyl radical. *The Journal of Chemical Physics*, 109(3):932, 1998.

[134] W. R. Thompson, M. B. Shah, and H. B. Gilbody. Single and double ionization of atomic oxygen by electron impact. *Journal of Physics B: Atomic, Molecular and Optical Physics*, 28(7):L321–L330, 1995.

[135] Peter Thoreau and Justin Little. Development of the SPACE Lab Thrust Stand for Millinewton Thrust Measurement. *36th International Electric Propulsion Conference*, pages 1–11, 2019.

[136] E. A.H. Timmermans, J. Jonkers, I. A.J. Thomas, A. Rodero, M. C. Quintero, A. Sola, A. Gamero, and J. A.M. van der Mullen. Behavior of molecules in microwave-induced plasmas studied by optical emission spectroscopy. 1. Plasmas at atmospheric pressure. *Spectrochimica acta, Part B: Atomic spectroscopy*, 53(11):1553–1566, 1998.

[137] Nolan M Uchizono, Adam L Collins, Anirudh Thuppul, Peter L Wright, Daniel Q Eckhardt, John K Ziemer, and Richard E Wirz. Electrospray Steady-State and Transient Emission Behavior. *36th International Electric Propulsion Conference*, pages 1–13, 2019.

[138] Théo Vialis, Julien Jarrige, Ane Aanesland, and Denis Packan. Direct thrust measurement of an electron cyclotron resonance plasma thruster. *Journal of Propulsion and Power*, 34(5):1323–1333, 2018.

[139] Theo Vialis, Julien Jarrige, and Denis Packan. Geometry optimization and effect of gas propellant in an electron cyclotron resonance plasma thruster. In *35th International Electric Propulsion Conference*, 2017.

[140] Benjamin Wachs and Benjamin Jorns. Effect of Background Pressure on Ion Dynamics in an Electron Cyclotron Resonance Thruster. *2018 Joint Propulsion Conference*, pages 1–12, 2018.

[141] Benjamin Wachs and Benjamin Jorns. Background pressure effects on ion dynamics in a low-power magnetic nozzle thruster. *Plasma Sources Science and Technology*, 29(4), 2020.

[142] Benjamin Wachs and Benjamin Jorns. Optimization of an ECR Thruster using Two Frequency and Pulsed Waveforms. *AIAA 2021-3382*, Aug 2021.

[143] Mitchell L.R. Walker, Richard R. Hofer, and Alec D. Gallimore. The effects of nude faraday probe design and vacuum facility backpressure on the measured ion current density profile of hall thruster plumes. *38th AIAA/ASME/SAE/ASEE Joint Propulsion Conference and Exhibit*, (July), 2002.

[144] HX Wang, Sun WP, Sun SR, and et al. Two-temperature chemical non-equilibrium modelling of a high velocity argon plasma flow in a low-power arcjet thruster. *Plasma Chem Plasma Process*, 34, 2014.

[145] K. Watanabe and A.S. Jursa. Absorption and Photoionization Cross Sections of H2O and H2S. *J Chem Phys*, 41:1650, 1964.

[146] Robert C. Wetzel, Frank A. Baiocchi, Todd R. Hayes, and Robert S. Freund. Absolute Cross Sections for Electron-Impact ionization of the Rare-Gas Atoms by the Fast-Neutral-Beam Method. *Physical Review A*, 35(2):559–577, 1987.

[147] J. Christopher Whitehead. Plasma-catalysis: The known knowns, the known unknowns and the unknown unknowns. *Journal of Physics D: Applied Physics*, 49(24), 2016.

[148] Yohji Yamamoto and Takeshi Tachibana. Feasibility study of water plasma jets for combustion promotion. *Fuel*, 186:846–852, 2016.